2015

Quantifying road roughness: multiresolution and near real-time analysis

Ahmad Abdulraheem Alhasan
Iowa State University

Quantifying road roughness: Multiresolution and near real-time analysis

by

Ahmad A. Alhasan

A dissertation submitted to the graduate faculty

in partial fulfillment of the requirements for the degree of

DOCTOR OF PHILOSOPHY

Major: Civil Engineering (Geotechnical Engineering)

Program of Study Committee:
David J. White, Major Professor
Kris De Brabanter
Pavana Vennapusa
Raj Aggarwal
Caroline Westort
Jeremy Ashlock

Iowa State University

Ames, Iowa

2015

DEDICATION

This work is dedicated to my wife, Ruba, who taught me the mysterious equations of love, and my parents, Abdulraheem and Hayat, and my family for their endless support.

TABLE OF CONTENTS

DEDICATION ii

LIST OF TABLES viii

LIST OF FIGURES ix

LIST OF SYMBOLS xii

ACKNOWLEDGMENTS xiii

ABSTRACT xiv

CHAPTER 1. GENERAL INTRODUCTION 1

Industry Problem 1

Industry Concerns 1

Impact on Industry 1

Technical Problem 2

Research Goals and Objectives 3

Significance of the Research 4

Background 5

Historical Practices for Measuring Roughness 6

Roughness measurements for paved roads 6

Roughness indices 8

Time-frequency roughness analysis 10

Roughness measurements for unpaved roads 11

Automate Machine Guidance (AMG) 12

Mathematical Models 13

Finite Difference Algorithm for Quarter-Car Simulations 13
Spatial-Frequency Analysis 17
Fourier analysis 17
Wavelets analysis 19
Discrete wavelet transform and multiresolution analysis 22
Dissertation Organization 26
Work Cited in Chapter 1 26
CHAPTER 2. SPATIAL PAVEMENT ROUGHNESS FROM STATIONARY LASER SCANNING 35
Abstract 35
Data Collection Using Stationary Laser Scanner 39
Analysis Approach 43
Visioning Algorithm 44
Simulation Algorithm 47
Indexing Algorithm 49
Results and Discussion 52
Visioning Algorithm 52
Simulation Algorithm Results 53
Indexing Algorithm Results 55
Summary and Conclusions 61
Work Cited in Chapter 2 63

CHAPTER 3. QUANTIFYING UNPAVED ROAD ROUGHNESS FROM TERRESTRIAL LASER SCANNING....67
Abstract....67
Methods....71
Data Acquisition....71
Analysis Approach....72
IRI Road Roughness....73
FFT Spectral Road Roughness....75
Surface Texture Analysis....76
Results and Discussion....78
Road Roughness....78
FFT Spectra....80
Surface Texture....82
Conclusions....86
Recommendations....87
Work Cited in Chapter 3....87
CHAPTER 4. CONTINUOUS WAVELET ANALYSIS OF PAVEMENT PROFILES....91
Abstract....91
Continuous Wavelet Transform....94
Analysis Approach....99
Road Profiles....99
CWT and Profile Decomposition....99
Quarter-Car Filter....101
Results and Discussion....103

Variance as a Summary Index 103
Statistical Analysis of AC and PCC Profiles 105
CWT Contour Plots 108
Significant Layers of Detail 111
Conclusions 115
Acknowledgements 116
Work Cited in Chapter 4 116
CHAPTER 5. WAVELET FILTERS DESIGN FOR PAVEMENT ROUGHNESS ANALYSIS 120
Abstract 120
Wavelet Analysis 124
Continuous Wavelet Transform 125
Discrete Wavelet Transform and Multiresolution Analysis 126
Analysis Approach 128
Road Profiles 128
Quarter-Car Wavelet Filter 129
Results and Discussion 133
Long Profiles Analysis 133
Stability of Analysis of Short Profiles 137
Spatial-Frequency Decomposition Using Wavelet Filters 142
Conclusions 144
Acknowledgments 145
Work Cited in Chapter 5 146

CHAPTER 6. GENERAL CONCLUSIONS 150

CHAPTER 7. WORKS CITED.....153

APPENDIX PSEUDOCODES FOR ANALYSIS ALGORITHMS.....166

LIST OF TABLES

Table 1. Methods for measuring road profiles and roughness 8
Table 2. Methods for analyzing pavement roughness 10
Table 3. Summary of articles..... 26
Table 4. Statistic results for quadratic model fit to mesh grid..... 53
Table 5. LTPP profile information. 99
Table 6. Scale factors, pseudo-frequencies, and pseudo-periods. 100
Table 8. Levene's test results for elevation and suspension rate distribution variance..... 107
Table 9. LTPP profile information. 129
Table 10. Wavelets used to design QC-wavelet filters..... 132
Table 11. Summary of results for 20 QC-wavelet filters used to analyze the 30 profiles..... 134

LIST OF FIGURES

Figure 1. Quarter-car model. 14
Figure 2. Morlet wavelet with different scales 21
Figure 3. Morlet wavelet overlapped with sinusoidal wave with frequency 0.81 22
Figure 4. (a) Original Daubechies wavelet basis (db21); (b) db21 wavelet basis after applying quarter-car filter to it; (c) original Mexican hat wavelet basis; and (d) Mexican hat wavelet basis after applying the quarter-car filter to it. 25
Figure 5. Laser scanner setup at “rough” pavement section showing scanner, GPS equipment and targets. 40
Figure 6. Registered point clouds for (a) “smooth” pavement and (b) “rough” pavement showing target sphere. 41
Figure 7. Sections included in the study: (a) new “smooth” full-depth HMA pavement and (b) “rough” HMA overly over JPCP. 42
Figure 8. Global processing algorithm. 43
Figure 9. Point cloud data after processing in the visioning algorithm for the “rough” pavement section. 46
Figure 10. Quarter-car model. 47
Figure 11. IRI versus width for both pavement sections included in the study. 54
Figure 12. Histogram of IRI values for both pavement sections included in the study. 55
Figure 13. “Smooth” pavement section surface maps of (a) absolute rectified slope, (b) absolute acceleration and (c) absolute spatial jerk. 56
Figure 14. “Rough” pavement section surface maps of (a) absolute rectified slope, (b) absolute acceleration and (c) absolute spatial jerk. 57
Figure 15. “Smooth” pavement index parameters as a function of speed: (a) rectified slope, (b) acceleration and (c) spatial jerk. 59
Figure 16. “Rough” pavement index parameters as a function of speed: (a) rectified slope; (b) acceleration; and (c) spatial jerk. 60
Figure 17. Trimble CX 3D laser scanner set-up. 71
Figure 18. Registered point cloud for data acquired from two stations. 73
Figure 19. Quarter-car model (Alhasan 2015). 74

Figure 20. Photo of the scanned area (top) and the smoothed surface showing sampled points (3D representation). 77
Figure 21. Rectified slope maps for 160th Street (5a) and 170th Street (5b). 79
Figure 22. IRI vs. width. 80
Figure 23. FFT for road profiles in (a) smooth surface with corrugations, (b) unsystematically rough surface with corrugations, (c) relatively smooth surface, and (d) unsystematically rough surface. 82
Figure 24. Grain size distribution of surface material for the three patches. 83
Figure 25. 3D surfaces for the three patches with the calculated areal parameters. 84
Figure 26. Height distribution and material ratio curves. 85
Figure 27. Morlet wavelet comparisons for different scale factors: (left) a = 1 and 2, and (right) a = 1 and 0.5. 97
Figure 28. Morlet wavelet overlapped with sinusoidal wave (frequency = 0. 8125). 98
Figure 29. Quarter-car model schematic. 101
Figure 30. Profile variance vs. IRI for (a) suspension rate profiles and (b) elevation profiles. 104
Figure 31. Suspension rate profile for (a) PCC section (124138) and (b) AC section (906420). 105
Figure 32. Wavelet decomposition amplitude contours for elevation (left) and SR profiles (right) in scale-distance domain for three AC sections with low, medium, or high roughness. 109
Figure 33. Wavelet decomposition amplitude contours for elevation profiles (left) and SR profiles (right) in scale-distance domain for three PCC sections with low, medium, or high roughness. 110
Figure 34. Average % variance of (a) elevation profiles and (b) suspension rate profiles at different scales for AC and PCC sections. 112
Figure 35. Section 06B441: (a) elevation profile derivative, (b) wavelet filtered elevation profile derivative, and (c) suspension rate profile from quarter-car simulations. 114
Figure 36. Mexican hat wavelet function with a scale factor a = 1 and a = 0.5. 125
Figure 37. Quarter-car model schematic. 129

Figure 38. An (a) original Daubechies wavelet function (db21) and (b) the wavelet function after applying QC filter to it, (c) an original Mexican hat wavelet function and (d) the wavelet function after applying the QC filter to it. 131
Figure 39. (a) High pass analysis filter and (b) low pass analysis filter for bior3.1 wavelet pair. 136
Figure 40. Comparison of (a) profile derivative, (b) rectified slope calculated using FD algorithm, (c) rectified slope calculated using QC-wavelet with morl0 basis, and (d) rectified slope calculated using QC-wavelet with db12 basis. 137
Figure 41. Average cross-correlation coefficient (C_c) versus segmented analyzed length for different QC-wavelet filters. 138
Figure 42. Average cross-correlation coefficient (C_c) versus segmented analyzed length for four approaches. 139
Figure 43. Coefficient of variance for the 30 profiles versus segmented analyzed length for different approaches. 140
Figure 44. Rectified slopes calculated for short profiles and obtained from the full length profiles using (a) FD algorithm, (b) QC filter and FFT, (c) QC- wavelet with morl0 basis, and (d) QC- wavelet with db12 basis. 141
(a) 142
(b) 143
Figure 45. Wavelet decomposition amplitude contours for (a) elevation profile and (b) SR profiles using QC-wavelet filter with db21 basis. 143
Figure 46. Wavelet decomposition amplitude contours for (a) elevation profile and (b) suspension rate profiles using QC-wavelet filter with a morl0 basis. 144

LIST OF SYMBOLS

Symbol	Description	Unit
IRI	International Roughness Index	m/km (in/mile)
QC	Quarter-car model	—
h_{ps}	Elevation profile after applying moving average	cm
z_s	Elevation of sprung mass	cm
z_u	Elevation of unsprung mass	cm
$\dot{z}s$	Elevation time derivative of sprung mass	cm/s
$\dot{z}u$	Elevation time derivative of unsprung mass	cm/s
k_t	Tire spring coefficient	kg/s^2
k_s	Suspension spring coefficient	kg/s^2
M_s	Sprung mass	kg
M_u	Unsprung mass	kg
c	Suspension damping rate	kg/s
μ	Ratio of unsprung mass to sprung mass	—
FD	Finite difference algorithm	—
SR	Suspension response profile	m/km (in/mile)
RS	rectified slope	m/km (in/mile)
CWT	continuous wavelet transform	—
DWT	Discrete wavelet transform	—
x	distance	m
ξ	Spatial frequency (wave number)	1/m
a	Scale factor	—
b	Shift factor	m
ψ	Wavelet function (mother wavelet)	—
$\hat{\psi}$	Fourier transform of wavelet function	—
$\overline{\psi}$	Wavelet function complex conjugate	—
V_j	Subspace in Lebesgue space $L^2(\mathbb{R})$	—
W_j	orthogonal complement of V_j	—
W_f	wavelet transform of function f	—
C_c	Cross-correlation coefficient at lag 0	—

ACKNOWLEDGMENTS

I would like to thank Dr. David White for his guidance, encouragement, and vision that inspired me to go beyond traditional thinking and pushed my experience in graduate school beyond my expectations. I feel lucky for receiving the opportunity to work with him for he made me a better researcher and thinker.

I would also like to Dr. Kris De Brabanter for his helpful guidance in statistics that made me think outside the box and expanded my view beyond civil engineering. I would also like to thank Dr. Raj Aggarwal, Dr. Pavana Vennapusa, Dr. Caroline Westort, and Dr. Jeremy Ashlock for their enlightening suggestions and helpful tips. Their discussions have moved this research beyond the theoretical scope towards real life applications.

Finally I would like to extend special thanks to Dr. Christianna White for all her effort and the time she spent teaching me proper writing skills. Without her training and guidance this work could not be done.

ABSTRACT

Road roughness is a key parameter for road construction and for assessing ride quality during the life of paved and unpaved road systems. The quarter-car model (QC model), is a standard mathematical tool for estimating suspension responses and can be used for summative or pointwise analysis of vehicle response to road geometry.

In fact, transportation agencies specify roughness requirements as summative values for pavement projects that affect construction practices and contractor pay factors. The International Roughness Index (IRI), a summative statistic of quarter-car suspension response, is widely used to characterize overall roughness profiles of pavement stretches but does not provide sufficient detail about the frequency or spatial distribution of roughness features.

This research focuses on two pointwise approaches, continuous roughness maps and wavelets analysis, that both characterize overall roughness and identify localized features and compares these findings with IRI results. Automated algorithms were developed to preform finite difference analysis of point cloud data collected by three-dimensional (3D) stationary terrestrial laser scans of paved and unpaved roads. This resulted in continuous roughness maps that characterized both spatial roughness and localized features. However, to address the computational limitations of finite difference analysis, Fourier and wavelets (discrete and continuous wavelet transform) analyses were conducted on sample profiles from the federal highway administration (FHWA) Long Term Pavement Performance data base. The Fourier analysis was performed by transforming profiles into frequency domain and applying the QC filter to the transformed profile. The filtered profiles are transformed back to spatial domain to inspect the location of high amplitudes in the suspension rate profiles.

Finite difference analysis provides suspension responses in spatial domain, on the other hand Fourier analysis can be performed in either frequency or spatial domains only. To describe the location and frequency content of localized features in a profile, wavelet filters were customized to separate the suspension response profiles into sub profiles with known frequency bands. Other advantages of wavelets analysis includes data compression, making inferences from compressed data, and analyzing short profiles (< 7.6 m). The proposed approaches present the basis for developing real-time autonomous algorithms for smoothness based quality control and maintenance.

CHAPTER 1. GENERAL INTRODUCTION

This dissertation focuses on the development and implementation of image and signal processing tools to continually quantify the surface roughness of roads and locate roughness features.

Industry Problem

Transportation agencies specify roughness requirements for pavement projects, and those requirements affect construction practices and contractor pay factors.

Industry Concerns

Even pavements that are designed and constructed to very stringent roughness specifications always deteriorate and get rougher over time. These deteriorations reduce ride quality, safety, and pavement performance and increase both vehicle operation and maintenance costs. Accurate evaluation of pavement roughness levels and modes is a key factor in optimizing quality control during construction and maintenance decisions (Chootinan et al. 2006; Lamptey et al. 2008).

With the emerging technologies in road construction (e.g., automated machine guidance (AMG), light detection and ranging (LIDAR), and 3D modeling), there is a need for a systematic approach that quantifies vehicle pavement interaction indices continually and in real-time, and uses these indices to take corrective actions for localized features during construction (Perera and Kohn 2002).

Impact on Industry

Current practice in evaluating pavements serviceability involves either visual inspection or expensive setups that require well trained personal. Using roughness indices presents an

objective and cost effective alternative (Park et al. 2007). However current roughness indices are summary statistics obtained for long sections (e.g., >7.6 m), ignoring the spatial variability of roughness. Also the algorithms used to evaluate these indices are not applicable for short profiles. Such limitations will result in false decisions during construction and maintenance activities, which will directly translate to budget misplacement and unnecessary expenditures. With the increasing need for smooth roads and limited budgets, better roughness indicators capable of capturing the spatial variability and quantifying localized features will reduce the construction and maintenance costs to produce smoother pavements.

Technical Problem

Roughness of paved roads is typically quantified by indices such as the International Roughness Index (IRI) and Ride Number (RN) (Sayers and Karamihas 1998). Ouyang and Madanat (2004) and Gao and Zhang (2013) investigated relationships between IRI values (i.e., where higher values indicate more roughness) and serviceability indicators and confirmed that higher IRI values correlate with increased vehicle operation and travel delay costs. Other researchers (Al-Omari and Darter 1994; Vidya et al. 2013) established correlations between IRI and other serviceability indicators (e.g., pavement condition index (PCI), present serviceability index (PSI), and present serviceability rating (PSR)) used in pavement management systems (Bianchini 2012).

In terms of structural performance, research by Sun and Deng (1998) showed that for vehicles operating at constant speed dynamic load power spectral density (PSD) is proportional to pavement PSD. Shi and Cai (2009) also indicated that dynamic loads induced by vehicles on rough pavements are significantly higher than static loads. Dynamic loads cause fatigue damage of the pavement and accelerates crack propagation (Sun et al. 2003),

these cracks are expected to initiate and propagate from localized rough features, because dynamic loads peak at these locations.

Although IRI characterizes the overall roughness profile of a pavement stretch, IRI values do not provide sufficient detail about the frequency or location of roughness features. PSD on the other hand can include details of the frequency content of a profile, but fails to locate rough features. Karamihas et al. (1999) investigated the variability in the IRI values for different profiles across the road, and reported that drivers typical wander laterally within a range of 50 cm (20 in).

Another part of the highway network is unpaved roads. Over one third of the roadway network in the U.S. is unpaved, and in Iowa approximately 72,000 of 115,000 miles are unpaved (Transportation 2012). There is a lack of a common set of criteria, many local agencies use visual inspection to estimate an IRI value (Archondo-Callao 1999; Namur and de Solminihac 2009; Walker et al. 2002). Some agencies combine visual inspection with direct measurement of defects (e.g., pothole depth, corrugation spacing) (Soria and Fontenele 2003; Woll et al. 2008). Several studies have pointed out the importance of precise assessment of unpaved road conditions to help transportation agencies decide whether to maintain or upgrade these roads (Archondo-Callao 2007; Huntington and Ksaibati 2011; McDonald and Sperry 2013; Zimmerman and Wolters 2004).

Research Goals and Objectives

The goal of this research is to develop ways to continuously quantify roughness of both paved and unpaved roads at near real-time that will overcome some of the limitations in current roughness indices.

The objectives of this research are to:

- Develop new algorithms to quantify roughness of localized features and produce continuous roughness profiles and maps.
- Develop algorithms that convert random 3D point clouds into uniform discrete points that can be viewed for analysis as surface grid maps.
- Study the vehicle response by simulating quarter-car model for different road profiles and different simulation parameters.
- Use wavelet analysis to calculate the vehicle response at each point in a profile.
- Compare the limitations of quarter-car simulation and wavelets analysis and the applicability of these methods in near real-time analysis.

Significance of the Research

Owners, contractors, agencies, and AMG equipment manufacturers will benefit from this research because it will allow accurate and automated assessment of surface conditions based on pavement performance indicators. Continuous roughness assessment will allow development of decision support systems to perform quality control autonomously (Rasmussen et al. 2013), and will set a step for future developments in predicting pavement performance based on construction conditions, which improves the optimized quality control and maintenance decisions which produces smooth long lasting roads (Kilpeläinen et al. 2011).

The products of this research include an algorithm that provides continuous roughness maps obtained using 3D point clouds from terrestrial laser scanners, the maps capture the spatial variability of surface roughness and provides a quantitative and visual aiding tool to allocate localized features. Another outcome of this research is the use of wavelets analysis to design specialized filters capable of analyzing short profiles (<7.6 m) and compressing the

data produced, these two characteristics qualifies the new approach for use in accurate real-time roughness evaluation.

Background

Pavement performance evaluation has been a research issue since the early twentieth century (Buchanan et al. 1941; Nakamura and Michael 1962). Gillespie et al. (1980) described methods to quantify pavement roughness using time-stable calibrated response-type systems. After 1986, the International Roughness Index (IRI) was established as a standard pavement roughness measurement (Sayers et al. 1986; Sayers et al. 1986). IRI and other roughness indices are summary statistics, and since their development the main focus was on increasing the measurement accuracy, and the results repeatability. Yet there is less agreement on how to quantify local features roughness, even though studies have shown that local features are very crucial to human comfort and cause most vehicle fatigue damage (Bogsjö and Rychlik 2009; Oijer and Edlund 2004; Steinwolf et al. 2002).

Unlike paved roads, there are no systematic approaches to quantify unpaved road roughness using time-stable indices, therefore the evaluation techniques of these roads vary significantly from state to state and county to county, and all the available techniques are either subjective or depend on measurements of distress size and not there effect on serviceability (Soria and Fontenele 2003; Zhang and Elaksher 2012).

The subsequent sections provide a background on some of the available techniques for assessing road roughness, it includes the field measurements and the indices used to assign roughness values for both paved and unpaved roads. Also a background on AMG and the role of real time roughness measurements in such systems is presented.

Historical Practices for Measuring Roughness

Quantifying roughness can be achieved either by subjective or objective approaches. Subjective approaches are not always reliable or accurate compared to objective approaches, but they were used before objective techniques were developed (Nakamura and Michael 1962) and still are used for unpaved roads due to the difficulties in obtaining profiles for those roads (Brooks et al. 2011). More recently basic measurements (e.g., deterioration features sizes) and subjective observations are summarized as indices or ratings to quantify surface conditions (Sayers and Karamihas 1996; Walker et al. 2002).

Roughness measurements for paved roads

As defined by Sayers and Karamihas, "a profiler is an instrument used to produce a series of numbers related in a well-defined way to a true profile" (1998). Measuring devices fall into two categories, systems that measure the coordinates of points along a linear track (geometry-type) and systems that measure the response of mechanical system driven along a track (response-type road roughness measure systems; RTRRM systems).

One of the basic geometry-type systems is the static rod level. In this method the elevations of sampled points along a line are recorded, the true elevation of a point is not critical, however the change in elevation relative to a reference point is the main concern (Gillespie et al. 1987). This technique is physically demanding and time consuming, yet it is stable and reliable. ASTM E1364–95 is the standard method to perform static level measurements.

Other geometry-type systems are available, including dipstick, rolling dipstick, rolling straightedge, and Hearne straightedge (El-Korchi et al. 2002; El-Korchi and Collura 1998;

Perera and Kohn 2002), but all of these devices are relatively time consuming compared to inertial profilers. Inertial profilers were developed in the 1960s (Spangler and Kelly 1964), and were standardized in ASTM E950, and these profilers are more accurate and faster than other profilers, hence the name high-speed profilers (Choubane et al. 2002).

High-speed profilers consist of four main components: an accelerometer, a non-contact height sensor(s), a speedometer, and a computer. The accelerometer measures the vertical acceleration of the height sensor. The height sensor(s) records the elevation from the ground using laser, infrared, or ultrasonic waves. The longitudinal distance relative to a reference point is measured by processing the speedometer readings. The computer processes the acceleration data to construct an inertial reference to filter out the height sensor motion due to suspension. Finally the computer combines these inputs and produces a sequence of distance versus elevation (Baus and Wang 2004).

RTRRM systems are based on measuring the relative movement between the axle and the body of a vehicle or a trailer of one tire (Gillespie et al. 1980). There are different types developed; BPR roughmeter (Moyer and Ahlborn 1956), Mays meter (Walker and Hudson 1973), and the PCA meter (Brokaw 1967). The disadvantage of these systems is the variability in the response due to different system parameters such as, suspension rat and tire pressure, thus the rating is not time-stable nor transportable.

Table 1 lists the available ASTM standards for measuring road profiles and surface roughness. However, although LIDAR is increasingly employed in the field, there is no ASTM standard for using LIDAR technologies in gathering road profiles and assessing surface roughness, a gap that needs to be filled.

Researchers have addressed the need to investigate new techniques in profiling using different scanning technologies. Some of these studies focused on modifications to inertial profilers to involve a broader variety of sensors, such as non-contact wide-footprint and multi-point height sensors (Fernando et al. 2014; Fernando and Walker 2013). Chang and Chang (2006) investigated the applicability of using stationary three dimensional (3D) laser scanning techniques in obtaining IRI.

Table 1. Methods for measuring road profiles and roughness

ASTM Designation	Title
E950 / E950M - 09	Standard Test Method for Measuring the Longitudinal Profile of Traveled Surfaces with an Accelerometer Established Inertial Profiling Reference.
E1082 – 90 (2012)	Standard Test Method for Measurement of Vehicular Response to Traveled Surface Roughness.
E1215 – 93 (2012)	Standard Specification for Trailers Used for Measuring Vehicular Response to Road Roughness.
E1274 - 03(2012)	Standard Test Method for Measuring Pavement Roughness Using a Profilograph.
E1364 - 95(2012)	Standard Test Method for Measuring Road Roughness by Static Level Method.
E1448 / E1448M - 09	Standard Practice for Calibration of Systems Used for Measuring Vehicular Response to Pavement Roughness.
E1703 / E1703M - 10	Standard Test Method for Measuring Rut-Depth of Pavement Surfaces Using a Straightedge.
E2133 – 03 (2013)	Standard Test Method for Using a Rolling Inclinometer to Measure Longitudinal and Transverse Profiles of a Traveled Surface.
E2560 - 13	Standard Specification for Data Format for Pavement Profile.

Roughness indices

Roughness indices are numbers calculated to summarize the surface conditions, and relate closely to ride quality. Several procedures were developed in the twentieth century to assess roads conditions by assigning roughness ratings and calculating index values. Roughness ratings normally refer to numbers assigned by subjective evaluation means (Bandara and Gunaratne 2001; Nick and Janoff 1983). Subjective ratings are conducted according to ASTM E1927 by a panel of pavement experts who rank the ride comfort of a

road section on a 0 to 5 scale. Individual ratings are referred to as present serviceability ratings (PSR), and the mean panel rating (MPR) is the average of the PSR values. To standardize rating procedures some measurements were incorporated to calculate a present serviceability index (PSI).

With the development of profilers, different indices were introduced. The first type was based on accumulating the absolute suspension strokes of an RTRRM system and dividing it by the traveled distance. The second type of index, including the profile index (PI), ride number (RN), international roughness index (IRI), uses mathematical models to simulate dynamic systems and calculate their response to measured profiles.

PI is the standard deviation of a selected frequency band of the PSD function of a road profile slope. Although selecting a frequency band attenuates frequencies outside a certain range, several frequency ranges have been proposed in the literature to reach the strongest correlation to MPR (Janoff 1988; Sayers and Karamihas 1996). RN is the exponential transform of PI (Equation 1) that was developed to follow the tradition of rating profiles on a 0 to 5 scale (Liu and Herman 1999):

$$RN = 5e^{-160PI} \tag{1}$$

When both the left and right real paths are profiled, the root mean square of those PIs is used as a summary index (Equation 2):

$$PI = \sqrt{\frac{PI_l^2 + PI_r^2}{2}} \tag{2}$$

IRI utilizes a mathematical model, sometimes called the golden quarter-car model, that simulates the dynamic response of a single tire connected to an axle, and the axle is connected to suspension system supporting a sprung mass. The accumulated suspension

strokes over the traveled distance is the IRI value (Gillespie et al. 1980). IRI has long been considered to be stable and empirically correlate with ride quality and vehicle operating cost (Gao and Zhang 2013; Ouyang and Madanat 2004). Other studies investigated the use of half- and full-car models to account for the other acceleration components (i.e., roll and pitch) riders would experience (Capuruço et al. 2005; Sayers 1989).

Table 2 lists the available ASTM standard procedures for quantifying road roughness. It should be noticed that no standard is provided for identifying localized features, which indicates the need for such a standard since localized features are of concern.

Table 2. Methods for analyzing pavement roughness

ASTM Designation	Title
E1170 – 97 (2012)	Standard Practices for Simulating Vehicular Response to Longitudinal Profiles of Traveled Surfaces.
E1489 – 08 (2013)	Standard Practice for Computing Ride Number of Roads from Longitudinal Profile Measurements Made by an Inertial Profile Measuring Device.
E1926 - 08	Standard Practice for Computing International Roughness Index of Roads from Longitudinal Profile Measurements.
E1927 – 98 (2012)	Standard Guide for Conducting Subjective Pavement Ride Quality Ratings.
E2034 – 99 (2012)	Standard Practices for Simulating Truck Response to Longitudinal Profiles of Vehicular Traveled Surfaces.
E2955 - 13	Standard Practice for Simulating Profilograph Response to Longitudinal Profiles of Traveled Surfaces.

Time-frequency roughness analysis

For more precise evaluation or investigation, PSD is used to understand both the frequency content of a profile and the sources of the frequencies that dominate the roughness of the profile. This approach is useful because the dynamic response of a vehicle can be found analytically in the frequency domain (Loizos and Plati 2008; Mucka and Granlund 2012). Transforming from spatial to frequency domain (Fourier transform) eliminates spatial localization (i.e., the frequency content of features can be found but not the location of these contents). On the other hand, knowing the locations of distinct, especially regular, features

(e.g., joints) reveals patterns that can be used as reference points in the frequency domain (Kohn et al. 2008).

Hesami and McManus (2009) considered two signal processing techniques, PSD and discrete wavelet transform (DWT) analysis, to quantify road roughness. DWT analysis outperformed PSD analysis in verifying road roughness features and locating high frequency defects such as cracks and potholes. DWT is computationally efficient and can be carried out by simple pyramidal algorithms. Tomiyama et al. (2014) used a lifting wavelet transform scheme to analyze sets of data collected with a response type profiler to detect and quantify pavement distresses. On average 77.9% of target distresses were identified correctly. Sen et al. (2012) used wavelet analysis to assess changes in pavement profile characteristics over time, and linked the changes to contributing factors (i.e., traffic loading, climatic conditions, pavement composition, and subgrade soil type). These studies suggest that wavelet analysis could be a useful technique for determining the location of problematic road segments, including unpaved roads, and identifying causes of deterioration.

Roughness measurements for unpaved roads

Road geometry (e.g., curves, cross sections) and the surface quality of unpaved roads (e.g., corrugation, loose aggregate, ruts, potholes) are the major features that affect road users' travel experience, safety, and vehicle operating costs (Archondo-Callao 2007; McDonald and Sperry 2013). There are three approaches to assess unpaved roads visual inspection, a combination of visual inspection and direct measurements, and indirect data acquisition (Brooks et al. 2011). Visual inspection approaches, such as pavement surface evaluation and rating (PASER) systems and road surface management system (RSMS), are

very common because they are easy to conduct and do not require specialized equipment (Goodspeed et al. 1994; Walker et al. 2002). Despite the ease of these approaches, they depend on the experience of the evaluator and fail to accurately quantify the serviceability.

Combinational approaches, such as Central Federal Lands, the Highway Division–Objective Rating System, and the Unsurfaced Road Condition Index (URCI), incorporate direct measurements collected with a basic measuring kit. These techniques are objective, so they are transferable and stable, but they do not necessarily reflect the vehicle/road interaction (Eaton and Beaucham 1992; Eaton et al. 1987; Woll et al. 2008).

Indirect data acquisition methods such as unmanned aerial vehicles (UAV), ground penetrating radar (GPR), and accelerometers have been explored for use on unpaved roads (Berthelot et al. 2008; Brown et al. 2003; Zhang 2009). Zhang and Elaksher (2012) used a UAV-based digital imaging system to create 3D surface models and developed algorithms to extract and characterize road features.

Automate Machine Guidance (AMG)

In the last decade many construction projects have utilized emerging technologies such as, building information model (Chau et al. 2004; Suermann 2009) and intelligent compaction (White et al. 2007). These are specific technologies, however the term automated machine guidance (AMG) is generic and includes monitoring and controlling the construction process using near real-time measurements and feedback loop that can react to the encountered conditions (Barrett 2008; Hannon 2007; White and Vennapusa 2009). There have been several successful projects that utilized AMG. Anderegg and Kaufmann (2004) reported that intelligent compaction can help optimizing the compaction and to prove the homogeneity and the achieved compaction degree.

Any AMG technology requires the development of real-time or near real-time measurements. The reason for using near real-time instead of plain real-time is that in most control systems literature, real-time is related to processes occurring at a scale of seconds and even milliseconds, the profound limitation to achieve that in construction applications that some construction parameters (e.g., roughness) cannot be assigned to a single point unless it is defined over a spatial domain with minimum size. Navon and Shpatnitsky (2005) investigated the automated measurement of performance parameters for earthmoving equipment and indicated the system feasibility and accuracy. Chang et al. (2009) developed a robot (Pioneer P3-AT) capable of collecting profile data and provide IRI values autonomously.

Rasmussen et al. (2013) reported several real-time smoothness measuring systems. One system, the GOMACO smoothness indicator (GSI), includes up to eight traces, two sonic sensors, and a slope sensor on each trace. The Ames Engineering profiler allows multiple sensors to be installed across a lane to acquire multiple profiles. Both systems have real-time graphics displays and calculate IRI and PI and bump alarms that identify localized features.

Mathematical Models

This section will discuss the mathematical formulation behind, quarter-car model, Fourier analysis, and wavelets analysis. These tools are the backbone for the new approach proposed. Along the discussion a general outline of the developed algorithms will be introduced.

Finite Difference Algorithm for Quarter-Car Simulations

The quarter-car model described in ASTM E1170-97 is used to simulate vehicular response along a longitudinal profile. This model quantifies rectified slopes at each point

along a profile. The dynamic system can be thought of as a mechanical filter that attenuates frequencies corresponding to the strokes absorbed by the suspension system and amplifies frequencies where the vehicle body resonates (Gillespie 1992; Sayers et al. 1986; Sayers and Karamihas 1996).

Figure 1 presents a schematic of the quarter-car model. The schematic represents a two degrees of freedom model where both sprung (M_s) and unsprung (M_u) masses move in the z-direction.

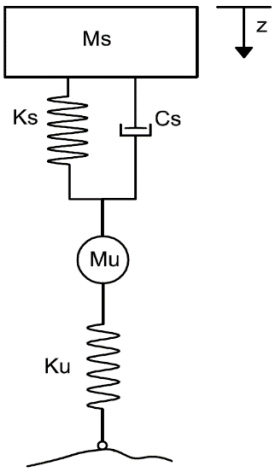

Figure 1. Quarter-car model.

Equation 3 is the differential equation of motion, in state-space form, used to determine the model response. A FORTRAN code is provided in ASTM E1926-08 to solve this equation. To take advantage of the object oriented nature of MATLAB, the code provided in ASTM was translated to a MATLAB function.

$$\dot{X} = AX + B h_{ps} \tag{3}$$

where

$$X = \begin{bmatrix} z_S & \dot{z}_S & z_u & \dot{z}_u \end{bmatrix}^T$$

$$A=\begin{bmatrix} 0 & 1 & 0 & 0 \\ -k_2 & -c & k_2 & c \\ 0 & 0 & 0 & 1 \\ \frac{k_2}{\mu} & \frac{c}{\mu} & -\frac{(k_1+k_2)}{\mu} & -\frac{c}{\mu} \end{bmatrix}$$

$$B=\begin{bmatrix} 0 & 0 & 0 & k1/\mu \end{bmatrix}^T \tag{4}$$

where h_{ps} is the elevation of the profile after applying the moving average smoother; z_S and z_u are the elevations of sprung and unsprung masses; $\dot{z}_S$ and $\dot{z}_u$ are elevation time derivatives of sprung and unsprung masses; k_1 is the tire spring coefficient divided by the sprung mass, k_2 is the suspension spring coefficient divided by the sprung mass, c is the suspension damping rate divided by the sprung mass, and μ is the ratio of unsprung to sprung mass.

Equations 5 through 8 represent the closed form solution of a differential equation in state-space form (Murray et al. 1994), this solution can be generalized in a matrix form (Equations 9 and 10) for a system of equations.

$$\dot{x}-\alpha x=\beta u_{ps} \tag{5}$$

$$e^{-\alpha t}\left[\dot{x}-\alpha x=\beta u_{ps}\right]$$

$$e^{-\alpha t}\dot{x}-e^{-\alpha t}\alpha x=e^{-\alpha t}\beta u_{ps}$$

Based on the chain rule and since x is a function of time;

$$\frac{d}{dt}\left[e^{-\alpha t}x(t)\right]=e^{-\alpha t}\dot{x}-e^{-\alpha t}\alpha x \tag{6}$$

Integrating both sides and introducing a dummy variable τ changing from t_{i-1} to t_i;

$$\int_{t_{i-1}}^{t_i} d\left[e^{-\alpha\tau}\, x(\tau)\right] = \int_{t_{i-1}}^{t_i} e^{-\alpha\tau}\, \beta\, u_{ps}.d\tau$$

$$e^{-\alpha t_i}\, x(t_i) = e^{-\alpha t_{i-1}}\, x(t_{i-1}) + \int_{t_{i-1}}^{t_i} e^{-\alpha\tau}\, \beta\, u_{ps}.d\tau \tag{7}$$

Multiplying both sides by $e^{\alpha t_i}$;

$$x(t_i) = e^{\alpha(t_i - t_{i-1})}\, x(t_{i-1}) + \int_{t_{i-1}}^{t_i} e^{\alpha(t_i - \tau)}\, \beta\, u_{ps}.d\tau$$

$$x(t_i) = e^{\alpha(t_i - t_{i-1})}\, x(t_{i-1}) + \frac{1}{\alpha}\left[1 - e^{\alpha(t_i - t_{i-1})}\right]\beta\, u_{ps} \tag{8}$$

β and u_{ps} are independent on τ, even though u_{ps} changes in each step it is an independent input and not affected by the solution. Rearrange Equation 8 in matrix notation yields;

$$X_i = S\, X_{i-1} + P\, h_{ps} \tag{9}$$

where

$$S = e^{A\Delta t}$$

$$P = A^{-1}(S - I)B \tag{10}$$

X, *A*, and *B* are defined in Equation 4, and *I* is the identity matrix. Rectified slope is defined mathematically as the absolute difference in elevation between the sprung and unsprung masses divided by the iteration step length (i.e., the second and forth elements in the vector *X*). IRI is the average of all rectified slope values along a profile. IRI is also defined as the accumulated suspension strokes divided by the traveled distance. Although the definitions are interchangeable, IRI calculated from rectified slope equations allows assigning values to points in a profile.

Spatial-Frequency Analysis

Spatial-frequency analysis is another approach to solve a described dynamic system. This approach namely depends on transforming the state equations from time to frequency or quasi-frequency domain. Such transformation allows deriving analytical forms to solve the system instead of iterating in spatial domain.

Fourier analysis

The analytical description of quarter-car model is best explained in terms of random signal analysis, where Fourier transformation can be a helpful tool for such analysis.

The basic assumption in this approach is that any profile can be decomposed into building sinusoids, for infinite precision the signal should be decomposed to an infinite number of sinusoids, however only finite number can be used to describe a signal. Equations 11 and 12 represent the forward and backward discrete Fourier transforms of a signal (Broughton and Bryan 2011).

$$\mathcal{F}(x) = X_k = \sum_{n=0}^{N-1} x_n \exp(-i2\pi kn/N) \tag{11}$$

$$\mathcal{F}^{-1}(X) = x_n = \frac{1}{N} \sum_{k=0}^{N-1} X_k \exp(i2\pi kn/N) \tag{12}$$

where the lower case variable x represents the signal in spatial (or time) domain, the uppercase variable X represents the function magnitude evaluated in the frequency domain, k is the frequency, n is the spatial coordinate (corresponding to time t), N is the number of points acquired in a signal, and i is the imaginary number. The forward transformation evaluates the signal at each frequency k in the frequency domain, given a signal in the spatial

domain. The backward or inverse transformation evaluates the signal at each point *n* in the spatial domain, given the frequency spectrum of the signal. Equation 13 can be rewritten in the general form to describe a profile as:

$$z(x) = \mathrm{Re}\left\{\sum_n A_n \exp i\left(\omega_n t + \varphi_n\right)\right\} \tag{13}$$

where A is the amplitude of the signal for a frequency ω_n, and ϕ_n is a random phase angle in the range $(-\pi, \pi)$ to allow for phase shift. For sufficiently long profiles that approximately satisfy Fourier analyses assumptions the analytical form of the rectified slope is described in Equation 14 (Liu and Herman 1998),

$$RS(t) = \dot{z}_s - \dot{z}_u = -\sum_j \overline{A}_j \sin\left[\varphi_s(\omega) + \omega_j t + \varphi_{k,j}\right] \tag{14}$$

where;

$$\overline{A}_j = \omega_j A_k R(\omega_i) \tag{15}$$

and j is the index at time t, ϕ_s is a phase angle function of a sprung mass, and R is the response function, described as a band pass filter (Equation 16). Note that the solution is a function of time, transformation from time domain to spatial domain is achieved by dividing the outputs over a constant speed (80 km/h for golden-car model).

$$R(\omega) = \alpha_0 \omega^2 \Big/ \left(1 + \alpha_1 \omega^2 + \alpha_2 \omega^4 + \alpha_3 \omega^6 + \alpha_4 \omega^8\right)^{1/2}$$

$$\alpha_0 = M_s / k_s$$

$$\alpha_1 = C_s{}^2 / k_s{}^2 - 2\left[M_s / k_s + (M_s + M_u)/k_t\right]$$

$$\alpha_2 = \left[M_s / k_s + (M_s + M_u)/k_t\right]^2 + 2\left(M_s M_u k_s - C_s{}^2 (M_s + M_u)\right) / k_s{}^2 k_t$$

$$\alpha_3 = C_s^{\,2}\left(M_s + M_u\right)^2 / k_s^{\,2} k_t^{\,2} - 2\, M_s M_u \left(k_s M_u + \left(k_s + k_t\right) M_s\right) / k_s^{\,2} k_t^{\,2}$$

$$\alpha_4 = \left(M_s M_u / k_s k_t\right)^2 \tag{16}$$

Implementing the Fourier analysis here would best suite stationary profiles, where no localized features are present or frequency content changes occur as a function of distance. For more random profiles where different frequencies are included this approach is expected to suffer from higher errors and low resolution in spatial domain due to the boundary conditions and the violation of the described assumptions (Stein and Shakarchi 2011).

Wavelets analysis

Wavelet transform decomposes data or functions into different waveband frequency components (scales), presented in spatial (or time) domains identical to the original spatial domain. Wavelets were developed independently in different fields (i.e., pure mathematics, physics, and engineering) to overcome the time-frequency resolution issues in Fourier analysis (Aslaksen and Klauder 1968; Calderón 1964; Daubechies 1992; Morlet 1983).

Time-frequency resolution issue in Fourier analysis is due to using infinitely periodic functions (i.e., sines and cosines) as building blocks. This assumption induces uncertainty in the analysis, where high resolution cannot be achieve simultaneously in both frequency and spatial domains. Equation 17 states that as the dispersion of a function in spatial domain about a fixed point x_0 decreases (i.e., higher resolution) the dispersion of the transformed function in the frequency domain about a fixed frequency ξ_0 increases to satisfy the inequality condition (Pinsky 2002; Stein and Shakarchi 2011).

$$D_0(f) D_0\left(\hat{f}\right) \geq \frac{1}{16\pi^2} \tag{17}$$

where;

$$D_0(f) = \int_{-\infty}^{+\infty} (x - x_0)^2 \left| f(x) \right|^2 dx$$

$$D_0(\hat{f}) = \int_{-\infty}^{+\infty} (\xi - \xi_0)^2 \left| \hat{f}(\xi) \right|^2 d\xi$$

To overcome this issue different building blocks (wavelets) are used. Wavelets can be thought of as wave pulses that translate in the spatial domain and can change size (dilate or shrink). The dispersion of a wavelet is controlled by a scale factor '*a*', where larger scale factors correspond to dilated waves and smaller scale factors correspond to shrunken waves. Equation 18 defines a wavelet function with scale factor '*a*' and translation factor '*b*', where *b* is the position of the wavelet center.

$$\psi_{a,b}(x) = \frac{1}{\sqrt{a}} \psi\left(\frac{x - b}{a} \right) \tag{18}$$

Similar to Fourier analysis there are continues and discrete transforms, namely the continuous wavelet transform (CWT) and discrete wavelet transform (DWT). Each transform is built on assumptions that a wavelet function should satisfy to qualify as a basis for the analysis. For most CWT bases have explicit forms defined in spatial or frequency domains.

For CWT, wavelets should satisfy two conditions; continuity with exponential decay, and the integral of ψ(x) should equal to zero. Also it is assumed in the analysis that ψ(x) equals zero outside the effective support interval [-*A*, *A*]. Morlet wavelet (Equation 19) is described as an example due to its wide use. Figure 2 shows the effect of different scales (0.5, 1, and 2) on the Morlet wavelet, scale 1 corresponds to the original function with no dilation or shrinking.

$$\psi(x) = e^{\frac{-x^2}{2}} \cos(5x) \tag{19}$$

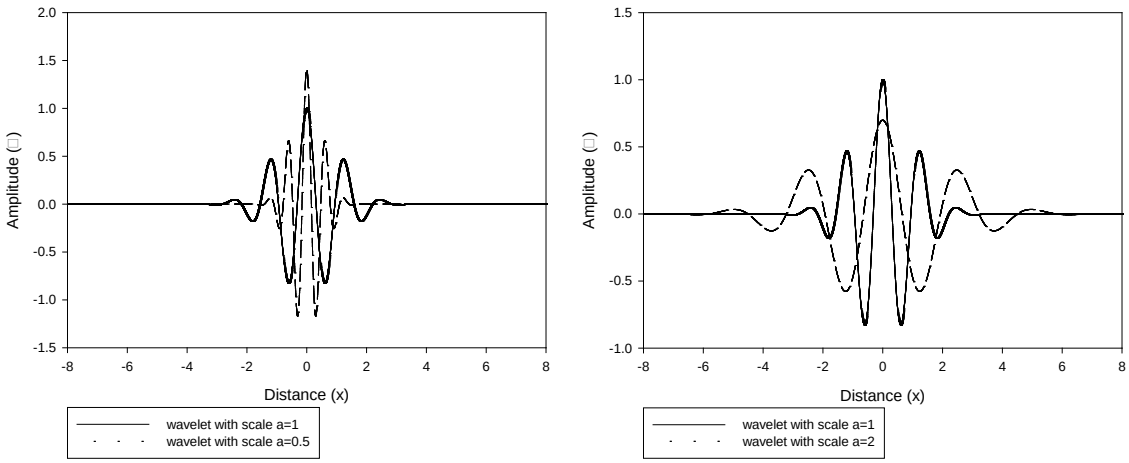

Figure 2. Morlet wavelet with different scales

CWT projects the signal on the wavelet function defined at different scales. Equation 20 defines the wavelet transform of a function as the inner product between the original function and the wavelet, at a spatial coordinate *b* and onto a wavelet with scale *a*.

$$W_f(a,b) = \left\langle \psi_{a,b} \middle| f \right\rangle = \int_{-\infty}^{+\infty} f(x)\overline{\psi}_{a,b}(x)dx \tag{20}$$

The Fourier transform of a wavelet results in a very narrow frequency band with central frequency f_c, this frequency is the most dominant frequency component in a wavelet and it corresponds to the frequency of a sinusoidal wave that matches the wavelet best (Figure 3). Scale factor changes the dominant frequency of a wavelet, the new frequency is referred to as pseudo-frequency and it is proportional to *1/a* (Equation 21). CWT decomposes a profile into '*j*' levels of detail corresponding to different scales (pseudo-frequencies), and the sum of these decomposed profiles returns back the original signal.

$$f = f_c / a \tag{21}$$

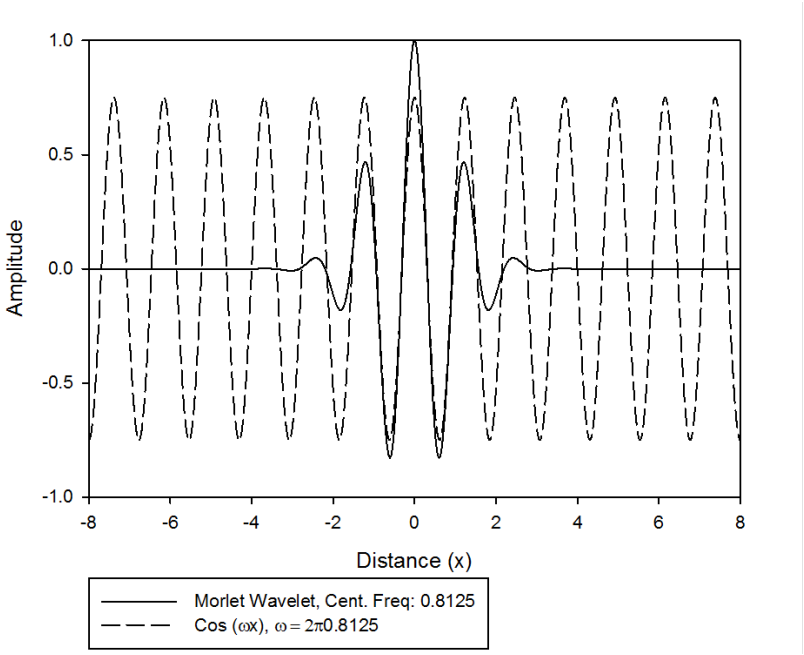

Figure 3. Morlet wavelet overlapped with sinusoidal wave with frequency 0.81

The inverse wavelet transform is defined in Equation (3). The equation provides the form to retrieve the full profile, however if a single layer of detail (frequency band) is of interest the second integration over all scales, can be eliminated.

$$f(x)=\frac{1}{C_\psi}\int_{-\infty}^{+\infty}\int_{-\infty}^{+\infty}|a|^{-1/2}\psi\left(\frac{x-b}{a}\right)W_f(a,b)\frac{dbda}{a^2} \tag{22}$$

where

$$C_\psi=2\pi\int_{-\infty}^{+\infty}\frac{|\hat{\psi}(\xi)|^2}{|\xi|}d\xi$$

Discrete wavelet transform and multiresolution analysis

Unlike CWT bases, DWT bases are constructed iteratively and are not smooth functions with explicit form. DWT bases should satisfy a set of conditions given elsewhere in the literatures (Boggess 2009; Daubechies 1992). Furthermore, the wavelet family constitutes a

sequence of subspaces V_j in Lebesgue space $L^2(\mathbb{R})$, where V_j is a subspace of scaling functions ϕ and defined as a linear combination:

$$\sum_{k \in Z} a_k \phi\left(2^j x - k\right) \tag{23}$$

Where a_k are amplitude coefficients and b is the shifting factor that determines the center of the function. Subsequently W_j is the subspace of wavelet functions ψ and defined as a linear combination:

$$\sum_{k \in Z} a_k \psi\left(2^j x - k\right) \tag{24}$$

Accordingly the wavelet function can be constructed as a linear combination of scaling functions as defined in Equation 25:

$$\psi(x) = \sum_l a_l \phi\left(2^j x - l\right) \tag{25}$$

W_j is the orthogonal complement of V_j in V_{j+1} as defined in Equation 26. Also from Equation 26 it can be seen that V_j is an element of V_{j+1}.

$$V_{j+1} = V_j \oplus W_j \tag{26}$$

where $\oplus$ is the orthogonal sum operator. If the collection of spaces satisfy the following five conditions, the analysis is called a multiresolution analysis (Boggess 2009):

1. Nested: $V_j \subset V_{j+1}$
2. Density: $\overline{\cup V_j} = L^2(R)$
3. Separation: $\cap V_j = \{0\}$
4. Scaling: The function $f(x)$ belongs to V_j if and only if the function $f(2^{-j}x)$ belongs to V_0.

5. Orthonormal basis.

The first condition can be deduced from Equation 25, and means that the content in a profile at level *j+1* can be composed of two other profiles one projected onto the scaling function and one on the wavelet function at level *j*. The second condition means that the whole space can be composed of the subspaces V_j. The third condition means that the decomposed profiles do not contain common features and thus each decomposition contains a unique set of features. The fourth condition indicates that the scaling of a space will correspondingly affect the function contained in the space by a factor 2^j. This condition corresponds to the down sampling of a profile when using pyramidal algorithms. The fifth condition insures that the bases do not interfere and the total energy of decomposed layers will be equal to the energy of original profile.

A road profile can be first filtered using wavelets to obtain layers of details. Since the layers are separate and nested for a multiresolution analysis, or approximately separate and nested for CWT, a quarter-car filter can be applied for each layer in frequency domain separately, and then based on the superposition principle these profiles will constitute the original filtered profile in spatial domain. Equation 27 represents the mathematical description for a CWT transform, however the exact same concept can be applied to the multiresolution analysis.

$$f_{QC}(x=b)=\sum_{j=1}^{N}\left\langle R_0 \left| W_f\left(a_j, b\right)\right.\right\rangle \tag{27}$$

where f_{QC} is the rectified slope, and R_0 is the quarter-car filter in spatial domain. The sum runs over all possible *N* layers of details. In addition since the quarter-car filter is linear (a linear operator) the order of filtering can be switched as shown in Equation 28.

$$f_{QC}(a,b) = \langle \psi_{a,b} | R_0 | f_s \rangle \tag{28}$$

Thus the quarter-car filter can be applied to the wavelet filter and then this new filter (i.e., QC-wavelet filter) can be used to decompose a road profile to SR profiles with different frequency bands in one step. To achieve that the wavelet filter should be transformed to the frequency domain and filtered using the quarter-car filter defined previously in Equation 16, then invert the new filter to the spatial domain. Figure 4 shows the original wavelets and QC-wavelet filters in spatial domain produced by applying the quarter-car filter on db21 and the Mexican hat wavelet respectively.

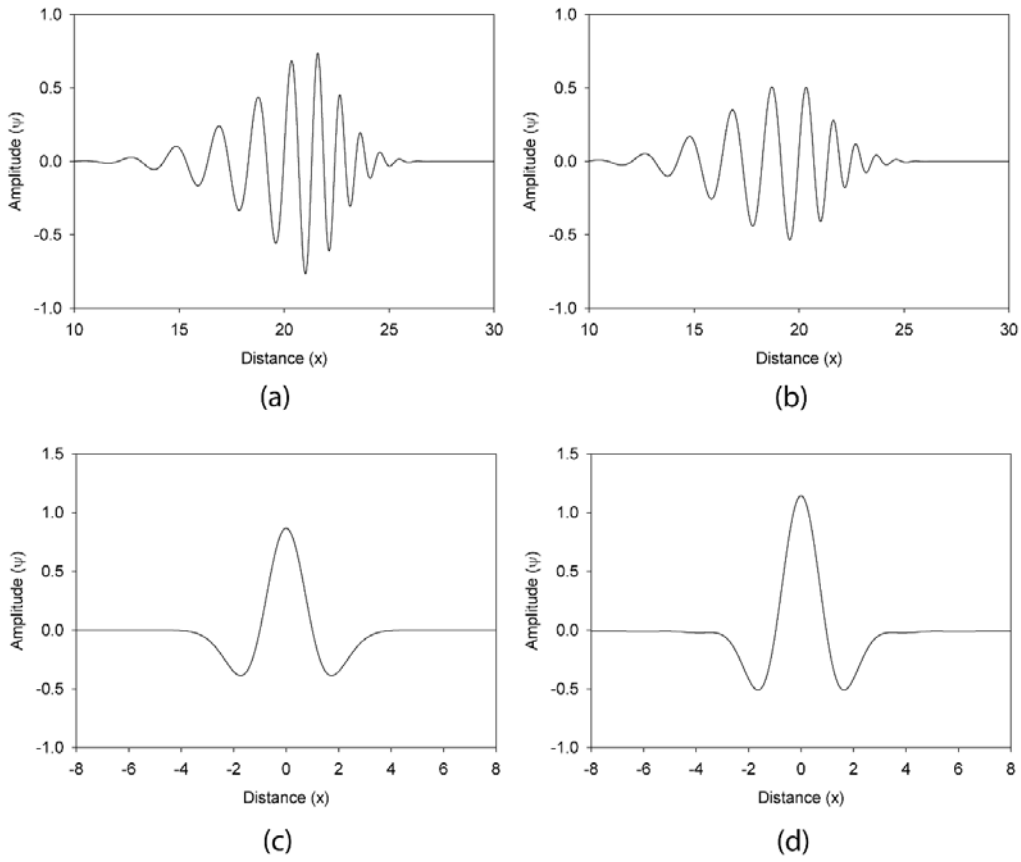

Figure 4. (a) Original Daubechies wavelet basis (db21); (b) db21 wavelet basis after applying quarter-car filter to it; (c) original Mexican hat wavelet basis; and (d) Mexican hat wavelet basis after applying the quarter-car filter to it.

Dissertation Organization

Following this introductory chapter, four research articles report the results of this study (Table 3).

Table 3. Summary of articles

Article Title	Journal	Authors	Submission Status
Spatial pavement roughness from stationary laser scanning.	*International Journal of Pavement Engineering*	Ahmad Alhasan, David J. White, and Kris De Brabanter.	Published
Quantifying unpaved road roughness from terrestrial laser scanning.	*Transportation Research Record: Journal of the Transportation Research Board*	Ahmad Alhasan, David J. White, and Kris De Brabanter.	In-press
Continuous wavelet analysis of pavement profiles.	*Automation in Construction*	Ahmad Alhasan, David J. White, and Kris De Brabanter.	Under review
Wavelet filter design for pavement roughness analysis.	*Computer-Aided Civil and Infrastructure Engineering*	Ahmad Alhasan, David J. White, and Kris De Brabanter.	Under review

Chapter 6 summarizes the outcomes and conclusions derived from this research, discusses how these conclusions can be applied in construction practice, and offers suggestions for future research. Following a complete references list, an appendix provides the algorithms developed in this project.

Work Cited in Chapter 1

Al-Omari, B., and Darter, M. I. (1994). "Relationships between international roughness index and present serviceability rating." *Transportation Research Record*(1435).

Anderegg, R., and Kaufmann, K. (2004). "Intelligent compaction with vibratory rollers: Feedback control systems in automatic compaction and compaction control." *Transportation Research Record: Journal of the Transportation Research Board*, 1868(1), 124-134.

Archondo-Callao, R. (1999). "Unpaved roads roughness estimation by subjective evaluation." *The World Bank*.

Archondo-Callao, R. (2007). "Evaluating economically justified road works expenditures on unpaved roads in developing countries." *Transportation Research Record: Journal of the Transportation Research Board*(1989), 41-49.

Aslaksen, E. W., and Klauder, J. R. (1968). "Unitary representations of the affine group." *Journal of Mathematical Physics*, 9(2), 206-211.

Bandara, N., and Gunaratne, M. (2001). "Current and future pavement maintenance prioritization based on rapid visual condition evaluation." *Journal of Transportation Engineering*, 127(2), 116-123.

Barrett, L. "Automated machine guidance: An emerging technology whose time has come?" *Proc., Transportation Research Board Annual Meeting. Washington, DC. January*.

Baus, R. L., and Wang, W. (2004). "Development of profiler-based rideability specifications for asphalt pavements and asphalt overlays." FHWA.

Berthelot, C. F., Podborochynski, D., Stuber, E., Prang, C., and Marjerison, B. "Saskatchewan case studies of network and project level applications of a structural asset management system." *Proc., Seventh International Conference on Managing Pavement Assets*.

Bianchini, A. (2012). "Fuzzy representation of pavement condition for efficient pavement management." *Computer-Aided Civil and Infrastructure Engineering*, 27(8), 608-619.

Boggess, A. (2009). *A First Course in Wavelets with Fourier Analysis*, Hoboken John Wiley & Sons, Hoboken, N.J.

Bogsjö, K., and Rychlik, I. (2009). "Vehicle fatigue damage caused by road irregularities." *Fatigue & Fracture of Engineering Materials & Structures*, 32(5), 391-402.

Brokaw, M. (1967). "Development of the PCA road meter: a rapid method for measuring slope variance." *Highway Research Record*(189).

Brooks, C., Colling, T., Kueber, M. J., Roussi, C., and Endsley, A. (2011). "Characterization of unpaved road condition through the use of remote sensing." Michigan Tech Research Institute.

Broughton, S. A., and Bryan, K. M. (2011). *Discrete Fourier analysis and wavelets: applications to signal and image processing*, John Wiley & Sons.

Brown, M., Mercier, S., and Provencher, Y. (2003). "Road maintenance with Opti-Grade®: Maintaining road networks to achieve the best value." *Transportation Research Record: Journal of the Transportation Research Board*, 1819(1), 282-286.

Buchanan, J. A., Catudal, A. L., Greenshields, B. D., and Moyer, R. A. (1941). "Standardizable equipment for evaluating road surface roughness." *Highway Research Board Proceedings*, 20.

Calderón, A. (1964). "Intermediate spaces and interpolation, the complex method." *Studia Mathematica*, 24(2), 113-190.

Capuruço, R. A., Hegazy, T., Tighe, S. L., and Zaghloul, S. (2005). "Full-car roughness index as summary roughness statistic." *Transportation Research Record: Journal of the Transportation Research Board*, 1905(1), 148-156.

Chang, J.-R., Chang, K.-T., and Chen, D.-H. (2006). "Application of 3D laser scanning on measuring pavement roughness." *ASTM Journal of Testing and Evaluation*, 34(2), 83-91.

Chang, J.-R., Su, Y.-S., Huang, T.-C., Kang, S.-C., and Hsieh, S.-H. "Measurement of the international roughness index (IRI) using an autonomous robot (P3-AT)." *Proc., 26th International Symposium on Automation and Robotics in Construction (ISARC). International Association for Automation and Robotics in Construction*.

Chau, K., Anson, M., and Zhang, J. (2004). "Four-dimensional visualization of construction scheduling and site utilization." *Journal of construction engineering and management*, 130(4), 598-606.

Chootinan, P., Chen, A., Horrocks, M. R., and Bolling, D. (2006). "A multi-year pavement maintenance program using a stochastic simulation-based genetic algorithm approach." *Transportation Research Part A: Policy and Practice*, 40(9), 725-743.

Choubane, B., McNamara, R. L., and Page, G. C. (2002). "Evaluation of high-speed profilers for measurement of asphalt pavement smoothness in Florida." *Transportation Research Record: Journal of the Transportation Research Board*, 1813(1), 62-67.

Daubechies, I. (1992). *Ten lectures on wavelets*, Philadelphia, PA : Society for Industrial and Applied Mathematics, Philadelphia, PA.

Eaton, R. A., and Beaucham, R. E. (1992). "Unsurfaced road maintenance management." U.S. Army Cold Regions Research and Engineering Laboratory, 67 p.

Eaton, R. A., Gerard, S., and Dattilo, R. S. "A method for rating unsurfaced road." *Proc., Fourth International Conference*, p. 34-43.

El-Korchi, T., Bacon, J., Turo, M., and Ecmecian, M. (2002). "Ride quality assessment with pavement profiling devices." *Transportation Research Record: Journal of the Transportation Research Board*, 1806(-1), 140-148.

El-Korchi, T., and Collura, J. (1998). "Comparative study of ride quality measuring devices." *Transportation Research Record: Journal of the Transportation Research Board*, 1643(-1), 125-135.

Fernando, E., Walker, R., and Mikhail, M. (2014). "Comparative testing of lasers for ride quality measurement on hot-mix asphalt pavements." *Transportation Research Record: Journal of the Transportation Research Board*, 2457, 19-29.

Fernando, E. G., and Walker, R. S. (2013). "Impact of changes in profile measurement technology on QA testing of pavement smoothness: Technical Report."Alexandria, VA: National Technical Information Service., 188p.

Gao, H., and Zhang, X. (2013). "A Markov-based road maintenance optimization model considering user costs." *Computer-Aided Civil and Infrastructure Engineering*, 28(6), 451-464.

Gillespie, T., Sayers, M., and Segel, L. (1980). "Calibration of response-type road roughness measuring systems." Washington, DC: Transportation Research Board, National Research Council, NCHRP Report 228, Available from: http://www.trb.org/Publications/Pages/262.aspx.

Gillespie, T. D. (1992). *Fundamentals of vehicle dynamics*, Warrendale, PA : Society of Automotive Engineers, Warrendale, PA.

Gillespie, T. D., Sayers, M. W., and Hagan, M. R. (1987). "Methodology for road roughness profiling and rut depth measurement." Federal Highway Administration, 47P.

Goodspeed, C. H., Schmeckpeper, E. R., and Lemieux, R. L. "Road surface management system." Transportation Research Board, p. 242-248.

Hannon, J. J. (2007). *Emerging technologies for construction delivery*, Transportation Research Board, Washington D.C.

Hesami, R., and McManus, K. J. "Signal processing approach to road roughness analysis and measurement." *Proc., TENCON 2009-2009 IEEE Region 10 Conference*, IEEE, 1-6.

Huntington, G., and Ksaibati, K. (2011). "Implementation guide for the management of unsealed gravel roads." *Transportation Research Record: Journal of the Transportation Research Board*, 2205(1), 189-197.

Janoff, M. S. (1988). "Pavement roughness and rideability field evaluation." Washington, DC: Transportation Research Board, National Research Council, NCHRP Report 308.

Karamihas, S. M., Gillespie, T. D., Perera, R. W., and Kohn, S. D. (1999). "Guidelines for longitudinal pavement profile measurement: final report." Transportation Research Board, 81 p.

Kilpeläinen, P., Jaakkola, M., and Alanaatu, P. (2011). "Development of a control system for a multipurpose road repairing machine." *Automation in Construction*, 20(6), 662-668.

Kohn, S. D., Perera, R. W., Cable, J. K., Karamihas, S. M., and Swanlund, M. "Use of profile data to detect concrete paving problems." *Proc., 9th International Conference on Concrete Pavements*, pp 690-703.

Lamptey, G., Labi, S., and Li, Z. (2008). "Decision support for optimal scheduling of highway pavement preventive maintenance within resurfacing cycle." *Decision Support Systems*, 46(1), 376-387.

Liu, C., and Herman, R. (1998). "Road profiles, vehicle dynamics, and human judgment of serviceability of roads: spectral frequency domain analysis." *Journal of transportation engineering*, 124(2), 106-111.

Liu, C., and Herman, R. (1999). "Road profile, vehicle dynamics, and ride quality rating." *Journal of Transportation Engineering*, 125(2), 123-128.

Loizos, A., and Plati, C. (2008). "An alternative approach to pavement roughness evaluation." *International Journal of Pavement Engineering*, 9(1), 69-78.

McDonald, T., and Sperry, R. (2013). "Evaluation of mitigation for safety concerns on low-volume, unpaved rural roads." Institute for Transportation, Iowa State University, Ames, IA.

Morlet, J. (1983). "Sampling theory and wave propagation." *Issues in Acoustic Signal—Image Processing and Recognition*, Springer, 233-261.

Moyer, R., and Ahlborn, G. (1956). "New developments in the BPR roughness indicator and tests on California pavements." *HRB Bulletin*, 139.

Mucka, P., and Granlund, J. (2012). "Comparison of longitudinal unevenness of old and repaired highway lanes." *Journal of Transportation Engineering*, 138(3), pp 371-380.

Murray, R. M., Li, Z., Sastry, S. S., and Sastry, S. S. (1994). *A mathematical introduction to robotic manipulation*, CRC press.

Nakamura, V. F., and Michael, H. L. (1962). "Serviceability ratings of highway pavements : technical paper." FHWA/IN/JHRP-62/18. Joint Highway Research Project, Indiana Department of Transportation and Purdue University, West Lafayette, Indiana, 1962., 43p.

Namur, E., and de Solminihac, H. (2009). "Roughness of unpaved roads." *Transportation Research Record: Journal of the Transportation Research Board*, 2101, 10-16.

Navon, R., and Shpatnitsky, Y. (2005). "Field experiments in automated monitoring of road construction." *Journal of construction engineering and management*, 131(4), 487-493.

Nick, J., and Janoff, M. (1983). "Evaluation of panel rating methods for assessing pavement ride quality." *Transportation Research Record: Journal of the Transportation Research Board*(946).

Oijer, F., and Edlund, S. (2004). "Identification of transient road obstacle distributions and their impact on vehicle durability and driver comfort." *Vehicle System Dynamics*, 41, 744-753.

Ouyang, Y., and Madanat, S. (2004). "Optimal scheduling of rehabilitation activities for multiple pavement facilities: exact and approximate solutions." *Transportation Research Part A: Policy and Practice*, 38(5), 347-365.

Park, K., Thomas, N. E., and Wayne Lee, K. (2007). "Applicability of the international roughness index as a predictor of asphalt pavement condition." *Journal of Transportation Engineering*, 133(12), 706-709.

Perera, R., and Kohn, S. (2002). "Issues in pavement smoothness." *Transportation Research Board, Washington, DC*.

Pinsky, M. A. (2002). *Introduction to Fourier analysis and wavelets*, Brooks/Cole Pacific Grove.

Rasmussen, R. O., Torres, H. N., Sohaney, R. C., Karamihas, S. M., and Fick, G. (2013). "Real-time smoothness measurements on Portland cement concrete pavements during construction." Transportation Research Board, SHRP 2 Report S2-R06E-RR-1, 143p.

Sayers, M. W. (1989). "Two quarter-car models for defining road roughness: IRI and HRI." *Transportation Research Record*(1215), 165-172.

Sayers, M. W., Gillespie, T. D., and Paterson, W. D. (1986). "Guidelines for conducting and calibrating road roughness measurements." *Technical Report UMTRI-84-13, Washington, DC: The World Bank.*

Sayers, M. W., Gillespie, T. D., and Queiroz, A. (1986). "The international road roughness experiment. Establishing correlation and a calibration standard for measurements." *Technical Report HS-039 586, Washington, DC: The World Bank.*

Sayers, M. W., and Karamihas, S. M. (1996). "Interpretation of road roughness profile data." University of Michigan Transportation Research Institute.

Sayers, M. W., and Karamihas, S. M. (1998). "The little book of profiling." *Ann Arbor: Transportation Research Institute, University of Michigan*.

Sen, R., Hassan, R. A., and Evans, R. P. (2012). "Wavelet-based detection of roughness progression in wavebands for highways in Victoria, Australia." *Transportation Research Record: Journal of the Transportation Research Board*, 2304(1), 17-27.

Shi, X., and Cai, C. (2009). "Simulation of dynamic effects of vehicles on pavement using a 3D interaction model." *Journal of Transportation Engineering*, 135(10), 736-744.

Soria, M., and Fontenele, E. (2003). "Field evaluation of method for rating unsurfaced road conditions." *Transportation Research Record: Journal of the Transportation Research Board*, 1819(-1), 267-272.

Spangler, E., and Kelly, W. (1964). "GMR road profilometer—A method for measuring road profile." *General Motors Corporation*.

Stein, E. M., and Shakarchi, R. (2011). *Fourier analysis: an introduction*, Princeton University Press.

Steinwolf, A., Giacomin, J., and Staszewski, W. (2002). "On the need for bump event correction in vibration test profiles representing road excitations in automobiles." *Proceedings of the Institution of Mechanical Engineers, Part D: Journal of Automobile Engineering*, 216(4), 279-295.

Suermann, P. C. (2009). "Evaluating the impact of building information modeling (BIM) on construction." Doctoral dissertation: University of Florida.

Sun, L., and Deng, X. (1998). "Predicting vertical dynamic loads caused by vehicle-pavement interaction." *Journal of transportation engineering*, 124(5), 470-478.

Sun, L., Hudson, W., and Zhang, Z. (2003). "Empirical-mechanistic method based stochastic modeling of fatigue damage to predict flexible pavement cracking for transportation infrastructure management." *Journal of Transportation Engineering*, 129(2), 109-117.

Tomiyama, K., Kawamura, A., and Ohiro, T. "Lifting wavelet transform for distress identification using response type profilers." *Proc., Transportation Research Board 93rd Annual Meeting*.

Transportation, U. S. D. o. (2012). "Highway Statistics 2012." Federal Highway Administration, Washington, DC.

Vidya, R., Santhakumar, S. M., and Mathew, S. (2013). "Estimation of IRI from PCI in construction work zones." *ACEE International Journal on Civil and Environmental Engineering*, 2(1).

Walker, D., Entine, L., and Kummer, S. (2002). "Gravel-Paser Manual: pavement surface evaluation and rating." Wisconsin Transportation Information Center.

Walker, R. S., and Hudson, W. R. (1973). "A correlation study of the Mays road meter with the surface dynamics profilometer." Center for Highway Research, University of Texas at Austin.

White, D. J., Vennapusa, P., and Thompson, M. J. (2007). "Field validation of intelligent compaction monitoring technology for unbound materials." *Tech Transfer Summaries*(Paper 2).

White, D. J., and Vennapusa, P. K. R. "Report of the workshop on intelligent construction for earthworks." *Proc., Workshop on Intelligent Construction for Earthworks*, 156p.

Woll, J. H., Surdahl, R. W., Everett, R., and Andresen, R. (2008). "Road stabilizer product performance: Seedskadee national wildlife refuge." *FHWA-CFL/TD-08-005*.

Zhang, C. (2009). "Monitoring the condition of unpaved roads with remote sensing and other technology." Geographic Information Science Center of Excellence, South Dakota State University.

Zhang, C., and Elaksher, A. (2012). "An unmanned aerial vehicle-based imaging system for 3D measurement of unpaved road surface distresses." *Computer-Aided Civil and Infrastructure Engineering*, 27(2), 118-129.

Zimmerman, K., and Wolters, A. (2004). "Local road surfacing criteria." South Dakota Department of Transportation, Federal Highway Administration, Applied Pavement Technology, Inc.

CHAPTER 2. SPATIAL PAVEMENT ROUGHNESS FROM STATIONARY LASER SCANNING

A paper published in *The International Journal of Pavement Engineering*

Ahmad Alhasan[1,2,3], David J. White[4], Kris De Brabanter[5]

Abstract

Pavement roughness is a key parameter for controlling pavement construction processes and for assessing ride quality during the life of a pavement system. This paper describes algorithms used in processing three-dimensional (3D) stationary terrestrial laser scanning (STLS) point clouds to obtain surface maps of point wise indices that characterise pavement roughness. The backbone of the analysis is a quarter-car model simulation over a spatial 3D mesh grid representing the pavement surface. With the rich data set obtained by 3D scanning, the algorithms identify several dynamic responses and inferences (suspension, acceleration and jerk) at each point in the domain. Variability in the indices is compared for a "rough" pavement and a "smooth" pavement in the spatial domain for different speed simulations of the quarter-car model. Results show high spatial variability in the various roughness indices both longitudinally and transversely (i.e., different wheel path positions). It is proposed that pavement roughness characterisation using a spatial framework coupled with univariate statistics provides more details on the severity and location of pavement roughness features

[1] Graduate research assistant, Department of Civil, Construction, and Environmental Engineering, Iowa State University.
[2] Primary researcher and author.
[3] Author for correspondence.
[4] Richard L. Handy Professor of Civil Engineering, Department of Civil, Construction, and Environmental Engineering, Iowa State University.
[5] Assistant Professor, Department of Statistics, Department of Computer Science, Iowa State University.

compared to the (1D) one-dimensional methods. This paper describes approaches that provide an algorithmic framework for others collecting similar STLS 3D spatial data to be used in advanced pavement roughness characterisation.

Keywords: 3D laser scanning, pavement roughness, quarter-car simulation, vehicle dynamics, algorithms

Ride quality is a key indicator of pavement performance and significantly affects highway construction practice, contractor payment and maintenance, and pavement roughness directly influences ride quality. Gillespie et al. (1980) described methods for using time-stable calibrated response-type systems to quantify pavement roughness. In 1986, the International Roughness Index (IRI) was established as the standard pavement roughness measurement (Sayers et al. 1986; Sayers et al. 1986). The IRI utilises a mathematical model that simulates the quarter-car dynamics and accumulates the quarter-car suspension response induced by variations in the vertical profile. The current IRI testing method (E950M-09) uses an instrumented vehicle to collect data in one or two wheel tracks.

IRI is widely used because it is considered to be stable and to empirically correlate ride quality and vehicle operating costs (Gao and Zhang 2013; Ouyang and Madanat 2004; Tsunokawa and Schofer 1994). However, IRI and other roughness indexes are summary statistics, and IRI research has mainly focused on improving the accuracy of measurements used to calculate IRI and the repeatability of IRI results. Further, there is less agreement on how to quantify local roughness features, even though studies have shown that local features affect rider comfort, pavement stresses and cause most vehicle fatigue damage (Bogsjö and Rychlik 2009; Kuo et al. 2011; Oijer and Edlund 2004; Steinwolf et al. 2002).

Some researchers have identified IRI limitations and proposed ways to address them. Herabat and Songchitruksa (2003) argued that IRI values are less representative than reporting pavement conditions as a single value based on calculations that account for IRI, distress, structural capacity and pavement friction. Other studies have demonstrated that artificial neural networks effectively relate pavement roughness to variables such as rut depth, patching, potholing and cracks, and improve predictions of the pavement roughness over time (Attoh-Okine 2001). Rahim et al. (2009) constructed a nonlinear model to predict the IRI of jointed plain concrete pavement (JPCP) sections rehabilitated by the crack, seat and overlay technique in different weather zones using several factors (i.e., age, depth of both concrete slab and asphalt overlay, base type and equivalent single axle load), and the coefficient of determination ranged between 0.5 and 0.62. Byrne et al. (2009) reported that seasonal variation influences IRI results; so, the results must be adjusted to account for the season when IRI measurements are performed to provide comparable values.

Some researchers have investigated theoretical models from other disciplines and adapted them to simulate vehicle-road interactions. Liu and Herman (1998) introduced a detailed theoretical description of vehicle-road interaction and discussed how it would affect human comfort. In another study, Liu and Herman (1999) showed that jerk (which is the rate of change in acceleration) has a vital role in explaining the serviceability of roads. Ahlin and Granlund (2002) analysed profile wave lengths to represent roughness to derive a relationships between whole-body vibration and IRI values. Marcondes et al. (1991) used spectral analysis to compute the power spectral density (PSD) function of road profiles and proposed a set of models for predicting PSD based on pavement type, age and IRI. Sun (2003) used linear regression to correlate IRI to PSD roughness. Loizos and Plati (2008)

called for a new index that would account for the effects of road roughness on vehicle performance at different speeds.

Recent developments in laser scanning techniques and light detection and ranging (LIDAR) sensing have motivated researchers and practitioners to adopt these technologies due to the accurate and rich data measurements. Recent studies (Fu et al. 2013; Tsai et al. 2010; Zalama et al. 2011), have demonstrated the effectiveness of laser scanning and LIDAR in identifying geometrical features of interest (e.g., cracks and bumps). Other systems (e.g. laser crack measurement system and LCMS) were developed to evaluate the IRI and other surface features, by accruing 3D scans and road profiles at highway speed (Laurent et al. 2014). Other studies have demonstrated how these techniques can be used to characterise features of both paved and unpaved roads (Ouyang and Xu 2013; Zhang and Elaksher 2012).

Researchers have addressed the need to investigate new techniques in profiling using different scanning technologies. Some of these studies focused on modifications to inertial profilers to involve a broader variety of sensors, such as noncontact, wide footprint and multi-point height sensors (Fernando et al. 2014; Fernando and Walker 2013). Also, recent studies have investigated the applicability of using stationary three dimensional (3D) laser scanning techniques in obtaining IRI (Chang et al. 2006) by selectively extracting track profiles. Despite the developments in using 3D laser scanning technology in identifying surface features and IRIs it is believed that more information can be inferred from the data rich 3D laser point clouds.

This study will introduce a procedure and associated algorithms used in processing 3D point clouds obtained for pavement sections, and to obtain spatial surface maps of point wise indices that characterise roughness. The backbone of the indices is a quarter-car model

simulation over a 3D mesh grid representing the pavement surface. Based on the simulation, several dynamic responses and inferences (suspension, acceleration and jerk) are determined at each point in the domain. As part of the study, the variability in the indices is discussed and compared for a “smooth” section and a comparatively “rough” section. Roughness variations were studied in the spatial domain, at different speeds of the quarter-car model, and summarised using univariate statistics. The procedural steps and algorithms are described in sufficient detail to allow the reader to replicate the calculations.

Data Collection Using Stationary Laser Scanner

LIDAR systems use a laser to measure information (spatial coordinates usually) of a 3D space and store the information in a 3D point cloud. The term LIDAR is generic: however, it usually refers to the airborne laser scanning technologies or mobile scanners mounted on vehicles. An additional configuration for this technology is stationary laser scanning or stationary terrestrial laser scanning (STLS), where the laser scanner is fixed at a station with known coordinates and based on the distance between the scanner and the detected points, a geospatially referenced 3D point cloud is constructed. Trimble CX 3D STLS system was used in this study to acquire the 3D laser scans. Figure 5 shows the equipment and set-up.

The process of scanning starts with an initial scan that acquires reference points in 3D space. This initial scan produces a *TZS file that is considered the mother file. Area scans are then conducted to acquire denser point clouds for the areas of interest. Criterion specified in this study for the point cloud spacing was a maximum spacing of 100 mm in both spatial directions (longitudinal and transverse) between two consecutive points in the region of interest. By several trials it was found that a density of 50 mm at 100,000 mm for the TZS scan and a density of 30 mm at 100,000 mm for the area scans, with approximately 25-m

spacing between the stations, produced sufficiently dense clouds to satisfy the 100 mm spacing criterion.

Figure 5. Laser scanner setup at "rough" pavement section showing scanner, GPS equipment and targets.

After acquiring the data, the equipment manufacturer's software (Trimble RealWorks 8.0) was used to register the point clouds. Registration of clouds is done by identifying common targets (spheres as shown in Figure 5) appearing in the *TZS scans of each consecutive station that share a common spatial domain with other stations. These targets are used as benchmarks to geospatially reference scans by matching the common target locations in each scan, and thus stitching the scans to produce a full 3D cloud. Using this process, the program was able to automatically detect the targets and align all scans acquired for a particular pavement section. Figure 6 shows examples of the registered point clouds. The variation in colour indicates the material reflectivity.

(a)

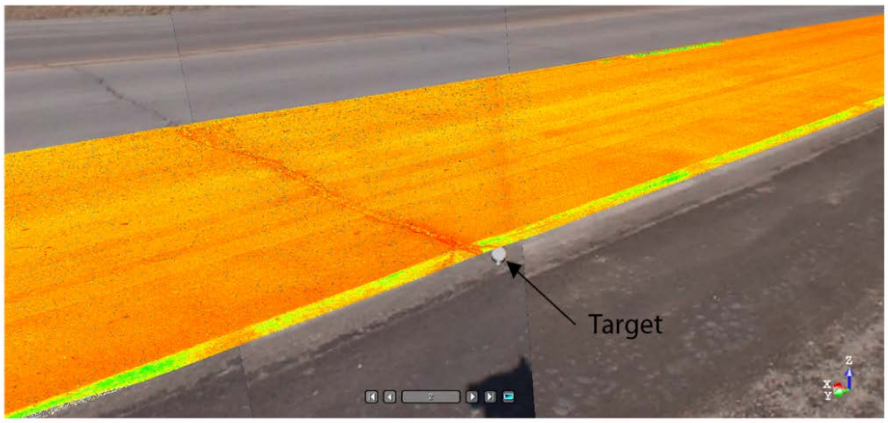

(b)

Figure 6. Registered point clouds for (a) “smooth” pavement and (b) “rough” pavement showing target sphere.

After registration, the point clouds are cleaned of unnecessary data points, where the sections of interest should be separated from areas beyond the edges of the sections and noise from any passing vehicles that might appear in the scans. The final data points left after cleaning were exported in ASCII file format; these files contain the x, y and z coordinates of the points in the section under consideration.

Figure 7(a) shows the “smooth” pavement section with a new full-depth hot-mix asphalt (HMA) surface. Approximately 45 meters of this pavement section was evaluated. Figure

7(b) shows the “rough” pavement section with an HMA overlay over a jointed plain concrete pavement (JPCP) pavement. This section was selected because of the observed rough pavement condition and distinct transverse cracking (reflective cracks over the underlying jointed pavement). About 60 meters of the east-bound lane was used in the evaluation. Both pavement sections were located in central Iowa, USA.

(a)

(b)

Figure 7. Sections included in the study: (a) new “smooth” full-depth HMA pavement and (b) “rough” HMA overly over JPCP.

Analysis Approach

Once the sections were cleaned and exported in ASCII format, the data points were further processed through several new algorithms, starting with (1) the visioning algorithm, then (2) the simulation algorithm and finally (3) the classification algorithm. Each algorithm is described thoroughly in the following subsection. Figure 8 shows the global processing algorithm developed for this study.

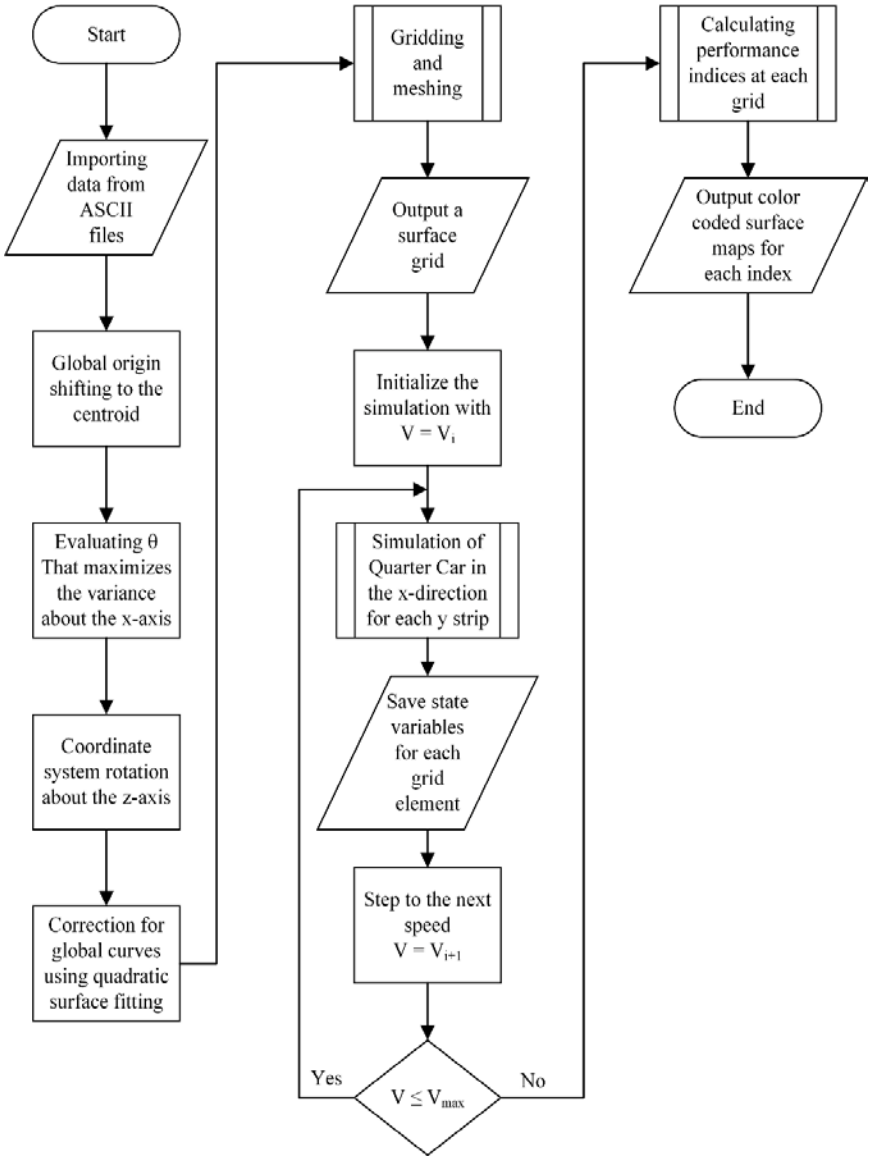

Figure 8. Global processing algorithm.

Visioning Algorithm

The first step in analysing the data is to form a mesh grid from the discrete measurement points. The grid elements have predefined *x* and *y* edge dimensions to form a grid region. The grid center elevation is calculated as the average of all cloud points falling in that grid region. All points are rotated and translated to a local coordinate system corresponding to the longitudinal and transverse axes (Zalama et al. 2011). Transformation for high accuracy and processing along curves can be achieved by constructing a curvilinear local coordinate system; however, for the purposes of this research the origin was translated to the center of the cloud and rotation was done for the *x* and *y* axes only. The elevation was corrected by subtracting the z elevation along a quadratic fit from the *z* coordinate of the corresponding point. Translation for each point can be described using the following vector operation shown in Equation (1):

$$\begin{Bmatrix} x_t \\ y_t \\ z_t \end{Bmatrix} = \begin{Bmatrix} x \\ y \\ z \end{Bmatrix} + T, \quad T = -\frac{1}{n}\begin{Bmatrix} \sum_{i=1}^{n} x_i \\ \sum_{i=1}^{n} y_i \\ \sum_{i=1}^{n} z_i \end{Bmatrix} \tag{1}$$

where the subscript *t* indicates the translated coordinates and *n* is the number of data points to be analysed in the point cloud. Spatial coordinates are then rotated by the matrix operation presented in Equation (2):

$$\begin{bmatrix} x_1' & x_2' & \cdots & x_n' \\ y_1' & y_2' & \cdots & y_n' \\ z_1' & z_2' & \cdots & z_n' \end{bmatrix} = R\begin{bmatrix} x_{t,1} & x_{t,2} & \cdots & x_{t,n} \\ y_{t,1} & y_{t,2} & \cdots & y_{t,n} \\ z_{t,1} & z_{t,2} & \cdots & z_{t,n} \end{bmatrix}, \quad R = \begin{bmatrix} \cos\theta & -\sin\theta & 0 \\ \sin\theta & \cos\theta & 0 \\ 0 & 0 & 1 \end{bmatrix} \tag{2}$$

The primed variables are centred and rotated. Herein, θ was determined using the principle component analysis (PCA) technique (Jolliffe 2005). PCA is based on rotating the axes to maximise the variance in the directions of orthogonal axes. PCA was implemented for the projection of the points into the *x*-*y* plane, where the variance was maximised in the *x*-axis direction as provided in Equation (3):

$$\theta = \max_{\theta} \left(x_t \cos\theta + y_t \sin\theta \right)^2 \tag{3}$$

After transforming the global coordinate system to a local system, least squares regression was performed on the points to fit the form shown in Equation (4) – quadratic with respect to *x* (longitudinal direction) and linear with respect to *y* (transverse direction). This fit surface was chosen to account for global vertical curves and side slopes. The lengths of the fitted segments were 44.7 and 58.5 m and the widths were 4.7 and 3.3 m. Due to the large dimensions of the fitted surfaces, only details with low frequencies have been removed. Removing the low frequency contentdoes not affect the analysis results and as for other segment dimensions, fitting parameters should be finely tuned to achieve the same purpose described here. The corrections can be translated to Equation (5):

$$z_b = \beta_1 x^2 + \beta_2 x + \beta_3 y + \beta_4 \tag{4}$$

Thus,

$$\begin{bmatrix} x_1'' & y_1'' & z_1'' \\ x_2'' & y_2'' & z_2'' \\ \vdots & \vdots & \vdots \\ x_n'' & y_n'' & z_n'' \end{bmatrix} = \begin{bmatrix} x_1' & y_1' & z_1' \\ x_2' & y_2' & z_2' \\ \vdots & \vdots & \vdots \\ x_n' & y_n' & z_n' \end{bmatrix} - \begin{bmatrix} x_1^2 & x_1 & y_1 & 1 \\ x_2^2 & x_2 & y_2 & 1 \\ \vdots & \vdots & \vdots & \vdots \\ x_n^2 & x_n & y_3 & 1 \end{bmatrix} \begin{bmatrix} 0 & 0 & \beta_1 \\ 0 & 0 & \beta_2 \\ 0 & 0 & \beta_3 \\ 0 & 0 & \beta_4 \end{bmatrix} \tag{5}$$

The double-primed coordinates in Equation 5 represent the corrected coordinates used to form the mesh grid for the pavement surface. Constructing a mesh starts by defining the boundaries of the section based on the location of extreme points in the cloud, then a grid of predefined element size is laid on the surface. Next points in the double-primed matrix are assigned to the corresponding grid element and the elevations of the points in a grid are averaged and assigned as the element centre elevation. This step simplifies the subsequent analysis procedures and reduces the large number of points (original point clouds with millions of data points) by about two orders of magnitude, therefore significantly improving computation time.

Figure 9 shows the “rough” pavement section point cloud data after processing in the visioning algorithm.

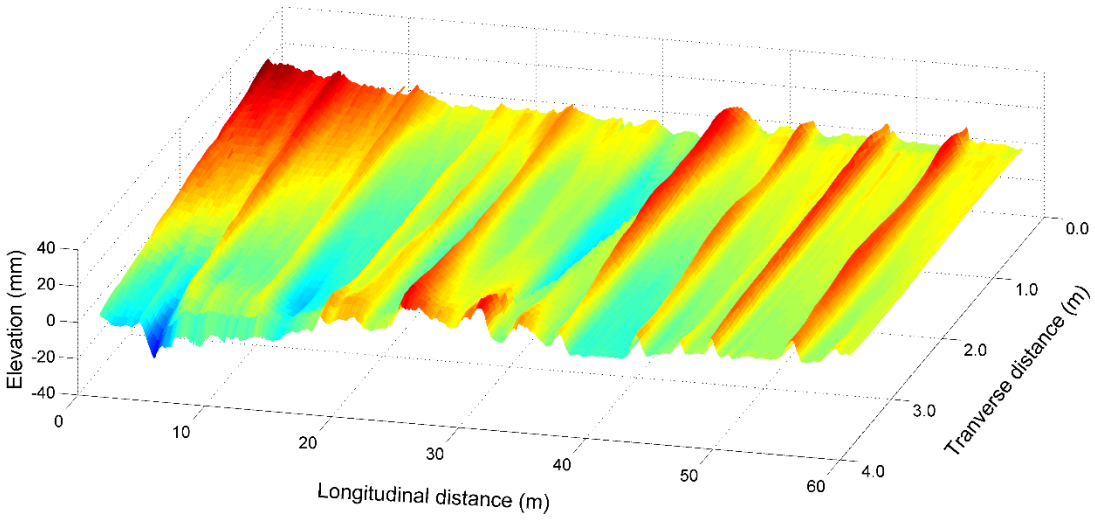

Figure 9. Point cloud data after processing in the visioning algorithm for the “rough” pavement section.

Simulation Algorithm

Evaluation of roughness in this study is based on the responses of a mechanical system that would approximate the response of a passenger vehicle. The mechanical system simulated herein is the quarter-car model described in (ASTM E1926-08). The quarter-car model was chosen over other models (i.e., half-car or full-car models) to define point wise mechanical responses of a single profile. Other models require incorporation of two or four points on a surface to define the mechanical responses for a simulated vehicle, which would change the details required to produce spatial maps of pavement roughness.

Figure 10 presents a schematic of the quarter-car model. M_s and M_u are the sprung and unsprung masses, respectively, k_s and k_t are the suspension and tire spring coefficients, respectively, and c_s is the suspension damping rate.

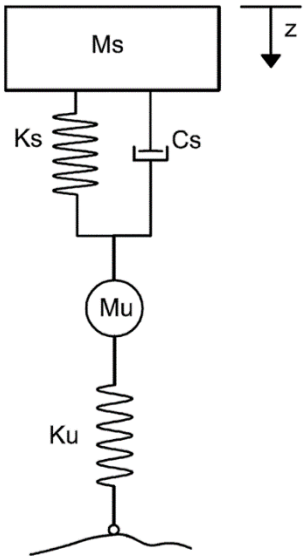

Figure 10. Quarter-car model.

The dynamics of the system can be described by four first-order differential equations presented in a matrix form (Sayers and Karamihas 1996) Equations (6)-(9):

$$\dot{X} = AX + B h_{ps} \tag{6}$$

where;

$$X = \begin{bmatrix} z_S & \dot{z}_S & z_u & \dot{z}_u \end{bmatrix}^T \tag{7}$$

$$A = \begin{bmatrix} 0 & 1 & 0 & 0 \\ -k_2 & -c & k_2 & c \\ 0 & 0 & 0 & 1 \\ \frac{k_2}{\mu} & \frac{c}{\mu} & -\frac{(k_1 + k_2)}{\mu} & -\frac{c}{\mu} \end{bmatrix} \tag{8}$$

$$B = \begin{bmatrix} 0 & 0 & 0 & k_1/\mu \end{bmatrix}^T \tag{9}$$

where h_{ps} is the elevation of the profile after applying the moving average smoother; z_S and z_u are the elevations of sprung and unsprung masses; $\dot{z}_S$ and $\dot{z}_u$ are elevation time derivatives of sprung and unsprung masses; k_1 is the tire spring coefficient divided by the sprung mass; k_2 is the suspension spring coefficient divided by the sprung mass; c is the suspension damping rate divided by the sprung mass; and μ is the ratio of the unsprung to sprung mass. FORTRAN code is provided in (ASTM E1926-08) to solve this system. In this paper, the code was translated to MATLAB code and used to simulate the quarter-car model over each longitudinal strip in the grid. A longitudinal strip is defined as a sequence of grid elements in the-x direction having one y coordinate. The longitudinal strips were then used as an input file for simulations. This approach leads to a 2D model where the elevation input *z* is a continuous function of the variable *x* and the fixed coordinate *y*. However, the discreteness

of the measurements and additional discreteness introduced by gridding the data mean that a finite number of profiles can be simulated to approximate the continuous 2D function. Because each profile is simulated independently, transverse effects such as rolling and pitch are not included.

Indexing Algorithm

Roughness index values interpreted from the simulation are suspension, which is the difference between the rates of change in the sprung and unsprung mass elevations; acceleration, which is the rate of change in the suspension; and jerk. These values are based on spatial derivatives where the base interval is in the longitudinal direction. In theory, the roughness index values are related, where suspension is the derivative of the elevation profile with respect to distance; (for time rate it will be with respect to time), and accordingly the acceleration would be the second derivative of the profile, etc.

To emphasise the human comfort level based on suspension values, the roughness index values are filtered to amplify and attenuate certain frequencies. The frequency filter can be presented by a gain function described in early studies (Liu and Herman 1998). The analytical description is best explained in terms of random signal analysis, where Fourier analysis techniques can be a helpful tool for such analysis.

The basic assumption in the approach used is that any profile can be decomposed into building sinusoids. For infinite precision, the signal should be decomposed to an infinite number of sinusoids; however, only a finite number of sinusoids can be used to describe a signal. Equations (10) and (11) represent the forward and backward discrete Fourier transforms of a signal.

$$\mathcal{F}(x) = X_k = \sum_{n=0}^{N-1} x_n \exp(-i 2\pi k n / N) \tag{10}$$

$$\mathcal{F}^{-1}(X) = x_n = \frac{1}{N} \sum_{k=0}^{N-1} X_k \exp(i 2\pi k n / N) \tag{11}$$

where the lower case variable *x* represents the signal in spatial (or time) domain, the uppercase variable *X* represents the function magnitude evaluated in the frequency domain, *k* is the frequency, *n* is the spatial coordinate (corresponding to time *t*), *N* is the number of points acquired in a signal and *I* is the imaginary number. The forward transformation evaluates the signal at each frequency *k* in the frequency domain given a signal in the spatial domain. The backward or inverse transformation evaluates the signal at each point *n* in the spatial domain given the frequency spectrum of the signal. Equation (11) can be rewritten in the general form to describe a profile as:

$$z(x) = \mathrm{Re}\left\{ \sum_k A_k \exp i(\omega_k t + \varphi_k) \right\} \tag{12}$$

where *A* is the amplitude of the signal for a frequency ω_k and ϕ_k is a random phase angle in the range ($-\pi$, π) to allow for phase shift. A periodic sinusoid with an angular frequency ω would stimulate the quarter car and induce the state variables described in Equation (7), and accordingly three response indices: velocity, acceleration and jerk, which can be identified for a single longitudinal profile. For sufficiently long profiles that approximately satisfy Fourier analyses assumptions, the exact response for a random profile can be obtained by superposition of the constituting sinusoids as described in Equation (13). Formulations of Equations (12) and (13) are described in (Liu and Herman 1998)).

$$j_n(t) = z_s^{(n)} - z_u^{(n)} = -\sum_i \overline{A}_{n,i} \sin^{(n-1)}\left[\varphi_s(\omega) + \omega_i t + \varphi_k\right] \tag{13}$$

where;

$$\overline{A}_{n,i} = \omega_i^n A_k R(\omega_i) \tag{14}$$

where j is the index at time t, n is the index number (n = 1 for velocity index, n = 2 for acceleration and n = 3 for jerk), the superscripts in parenthesis indicate the differentiation order, ϕ_s is a phase angle function of the frequency and R is the response function that depends on the system parameters and can be thought of as a band pass filter in the Fourier domain. Velocity index is the time rate at which the sprung mass is moving in the z-direction relative to the unsprung mass. This index reflects the suspension rate for a quarter-car model, and is commonly known as the average rectified slope (ARS) when transformed to a spatial derivative in the x-direction. Rectified slope (velocity index) can be calculated by taking the difference between the first and third elements in the state variable vector described in Equation (7). Transformation from time domain to spatial domain is achieved by dividing the outputs over a constant speed (80 km/h).

The acceleration index is related to human comfort while traversing the full profile and is computed by taking the absolute difference between the second and the fourth elements in the state variable vector. Finally, the spatial jerk describes the change in acceleration and thus relates to localised features and abrupt changes in the vertical acceleration. Spatial jerk is calculated by differentiating the acceleration with respect to x, keeping in mind the proper transformation from time domain to spatial domain.

Implementing the Fourier analysis here would only suite stationary profiles, where no localized features are present or frequency content changes occur as a function of distance. For more random profiles, where different frequencies are included, this approach suffers from higher errors and low resolution in spatial domain due to the boundary conditions and the violation of the described assumptions (Stein and Shakarchi 2011); thus quarter-car simulation is preferred in producing the surface maps.

Results and Discussion

Visioning Algorithm

As described previously, the algorithm starts by transforming the global coordinate system to a local system, where PCA is implemented to define the rotation angle (θ) required to maximise the variance about two orthogonal axes.

Regression diagnostics show that the assumed parameters of the least squared model are significant where $p < 0.05$ (Table 4). The adjusted R^2 are greater than 0.99, which indicates that more than 99% of the variation in the data can be explained by the proposed models. This step can be embedded as a part of the algorithm, where if a certain parameter is insignificant, a new model should be fitted excluding insignificant parameters to reduce the variance of the model. For any fitted model, total error is a combination of the irreducible error, bias and variance. Irreducible error cannot be controlled; bias is induced by a shift between estimated models and real measurements; and variance results from over fitting and including insignificant parameters that can induce errors. In this study, irreducible error and bias are less important than variance because the key role of the model is to predict the surface trend rather than exact positions of the surface.

After transforming the global coordinate system to a local system via the data modelling, the elevation of each element in the grid is calculated as the average of the elevations of the points bounded inside that element. The grid size of the "rough" pavement section was 588 x 34 grid regions, where each grid region is 100 mm x 100 mm as mentioned before; thus this section is 58.8-m long and 3.4-m wide. The "smooth" pavement section is 45.0-m long x 4.7-m wide.

Table 4. Statistic results for quadratic model fit to mesh grid.

Pavement Section	Coefficient	Estimated Parameter	Standard Error	t-value	Probability ($>\|t\|$)	Model Statistics
Lincoln Way (Rough)	β_1	$2.179\text{x}10^{-8}$	$9.309\text{x}10^{-12}$	2341	$<2\text{x}10^{-16}$	$R^2_{adj} = 0.999$, $F = 5\text{x}10^9$, $p < 2 \text{ x } 10^{-16}$
	β_2	$9.806\text{x}10^{-3}$	$8.648\text{x}10^{-8}$	113389	$<2\text{x}10^{-16}$	
	β_3	$-2.014\text{x}10^{-2}$	$1.175\text{x}10^{-6}$	-17135	$<2\text{x}10^{-16}$	
	β_4	-3.919	$2.000\text{x}10^{-3}$	-1960	$<2\text{x}10^{-16}$	
10^{th} St. (Smooth)	β_1	$-1.305\text{x}10^{-8}$	$1.972\text{x}10^{-11}$	-662	$<2\text{x}10^{-16}$	$R^2_{adj} = 0.994$, $F = 9\text{x}10^8$, $p < 2 \text{ x } 10^{-16}$
	β_2	$-9.427\text{x}10^{-3}$	$2.016\text{x}10^{-7}$	-46753	$<2\text{x}10^{-16}$	
	β_3	$-6.253\text{x}10^{-3}$	$1.070\text{x}10^{-6}$	-5845.1	$<2\text{x}10^{-16}$	
	β_4	$9.882\text{x}10^{-1}$	$2.166\text{x}10^{-3}$	456.3	$<2\text{x}10^{-16}$	

Simulation Algorithm Results

As described previously, simulation is conducted using the output grid where each strip in the x-direction is considered an independent profile. To validate the simulation algorithm, each strip was used as an input to ProVAL 3.4 (2013) to obtain the IRI values. The IRI values were compared with the IRI results for each strip obtained from the algorithms, which is the average rectified slope at each point along the strip. Traditionally, IRI is obtained using a line profile, representing the wheel track. Both right and left wheel tracks can be used to compute an average IRI, which is statistically close to the results from the half-car model simulation where the profiles should be synchronised to be used as an input for the model.

Despite the elegancy and simplicity of the theory underlying IRI, debates are usually raised regarding the representativeness of the chosen profile(s), and the repeatability of the profile measurement. Figure 11 shows IRI values for multiple wheel tracks across the full width of the pavement sections. For the “rough” pavement section, IRI varies from 4.3 to 6.5 m/km, depending on the selected wheel track. In comparison, the “smooth” pavement IRI varies from 1.2 to 2.8 m/km across the width. Figure 11 shows the estimated wheel track locations spaced 1.8 m between the axels, and assumed the car is centered in the lane, as shown in Figure 11. It can be seen that small shifts in the wheel paths might result in appreciable differences.

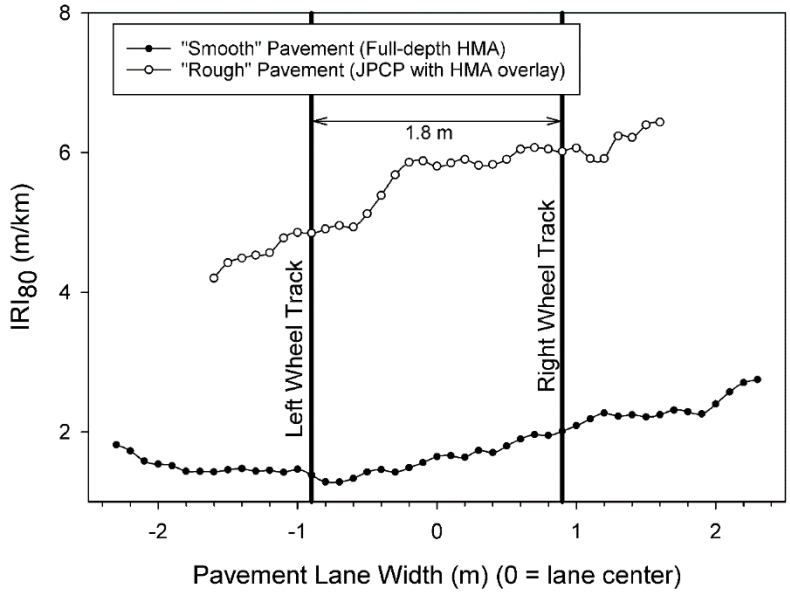

Figure 11. IRI versus width for both pavement sections included in the study.

Figure 12 presents a histogram for the IRIs obtained for all wheel tracks for both pavement sections. The bin widths were tuned using the method described in Wand (1997). High variability in the IRI values across the widths demonstrates that even with 2D analysis (e.g., wheel track profiles), it would be hard to specify a single number to characterise the

condition. With the results presented here, it is proposed that the mean and standard deviation provide useful information to characterise the observed physical variations.

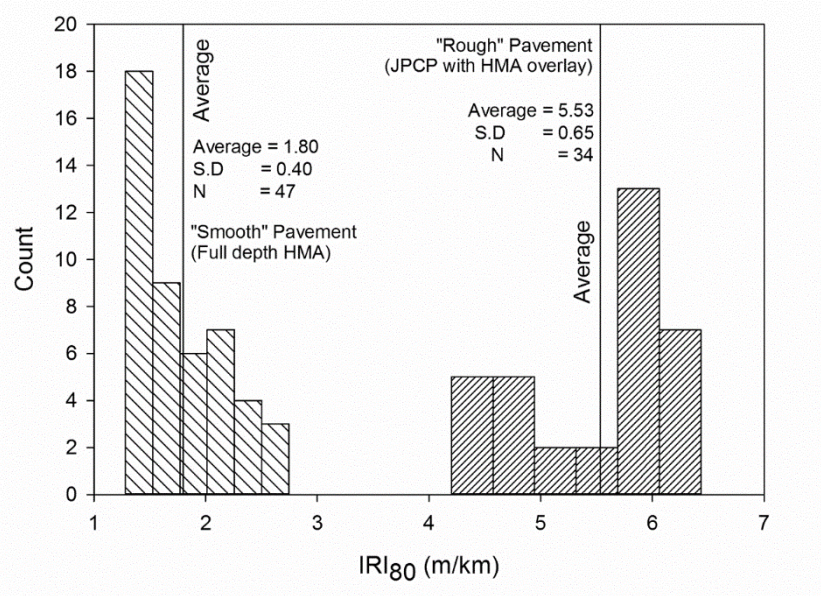

Figure 12. Histogram of IRI values for both pavement sections included in the study.

Indexing Algorithm Results

Figure 13 and Figure 14 show the surface maps produced from the simulations. These maps aid in visualising the spatial roughness based on rideability criteria. Localised areas of distress are clearly distinguishable in these maps. Although the maps are highly detailed, they suffer from the trade-off between high details (pointwise indices) and the ability to simulate full-car models that would include rolling and pitch reactions. This trade-off arises from the fact that full car models incorporate multiple points in the analysis to produce one index at time *t*, unlike the quarter-car model, where each instant of time corresponds to a single point. Another aspect of that trade-off is how representative this model is to actual ride condition. The results obtained are not necessarily equal to the actual vertical acceleration a rider would

feel; however, it gives some very good indication and it can be used as an index, where it is more important to specify a level of roughness that can be scaled and used for evaluation, rather than emulating the exact response. Also, absolute values for all indices are normally reported because the normally true values would have averages close to zero, and thus it will not reflect the true rideability conditions. It is also more important to evaluate the level of severity in the road, unless detailed analysis is needed to evaluate the vehicle behaviour at a single feature in the section.

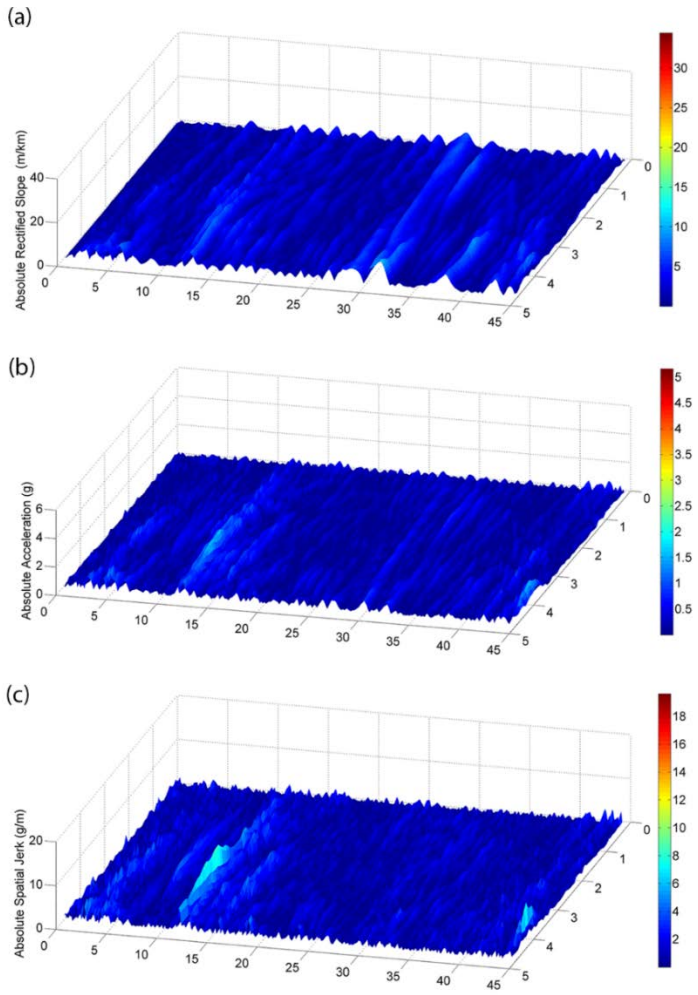

Figure 13. "Smooth" pavement section surface maps of (a) absolute rectified slope, (b) absolute acceleration and (c) absolute spatial jerk.

The spatial jerk map is obtained by differentiating the acceleration map with respect to x, where this differentiation can be done by several numerical differentiation techniques that include centered differencing, forward differencing, backward differencing and the differentiation in Fourier space, where a vector can be transformed to the Fourier space, then each element is multiplied by the frequency it corresponds to and finally Fourier inversion is applied to get back a vector congaing the numerical derivatives. Centered differencing was chosen due to its simplicity, and it gives good approximations similar to the ones obtained using the Fourier conversion.

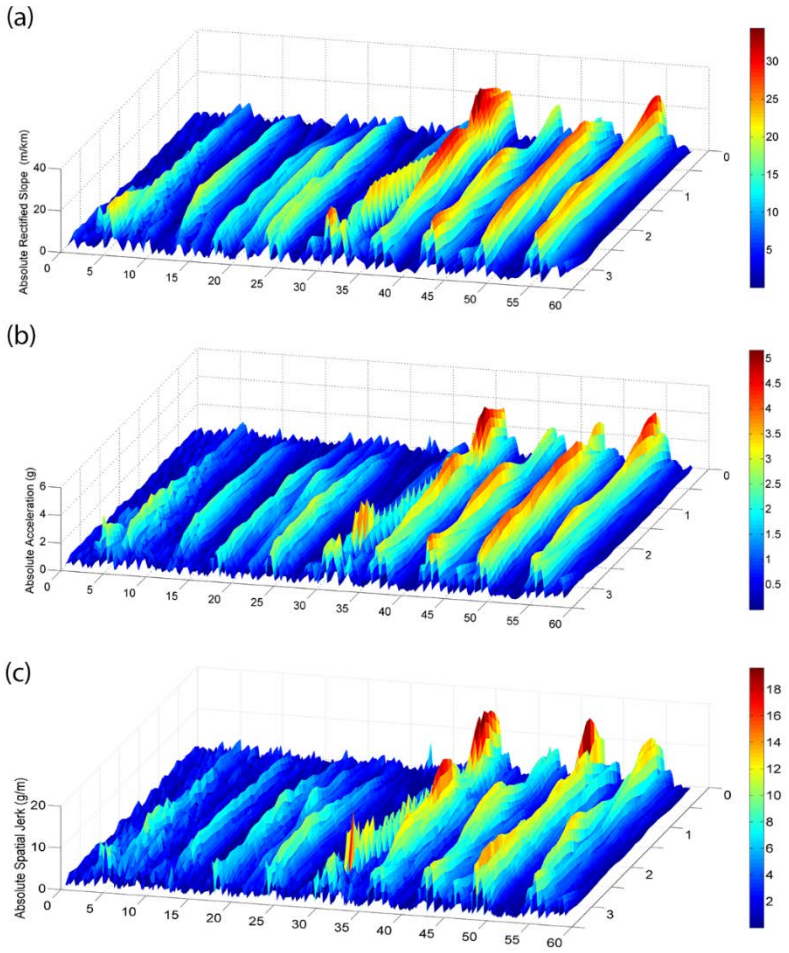

Figure 14. "Rough" pavement section surface maps of (a) absolute rectified slope, (b) absolute acceleration and (c) absolute spatial jerk.

It is clear that even though the maps have similar trends there is a phase shift due to differentiation; also, the trends do not exactly match, for example, in the “smooth” pavement section, the bump in the spatial jerk map between stations 10 and 15 is not as clear in the rectified slope map. On the other hand, bumps in the rectified slope map between stations 20 and 45 have disappeared in the spatial jerk map. Similar features can be observed in the “rough” pavement section. This observation emphasises the difference in information carried by each index map and the need to utilise the information these indices hold.

Another aspect that was investigated is the dependency of analysis on speed. For a single sinusoid, detection is straightforward; however, for random profiles, the response would differ. As shown in Figure 15(smooth) and Figure 16 (rough), the rectified slope increases up to a maximum peak and then decreases at higher speeds. The trend of the rectified slope curve and some of its features, such as the location and number of peaks depends on the profile. This dependency was observed in the surface maps of the same section at different speeds, where certain features were amplified at selected speeds, while the others were tampered. Such behavior can be explained by the band pass filtering procedure that amplifies certain frequencies in favor of other frequencies.

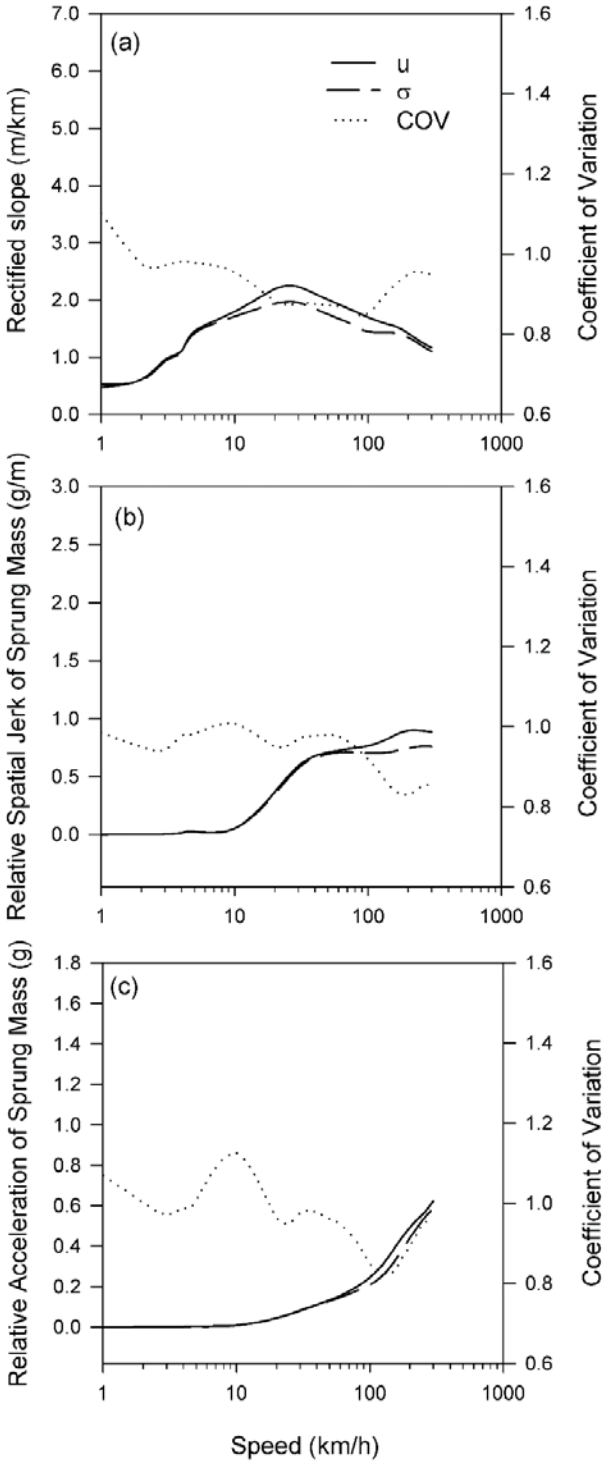

Figure 15. "Smooth" pavement index parameters as a function of speed: (a) rectified slope, (b) acceleration and (c) spatial jerk.

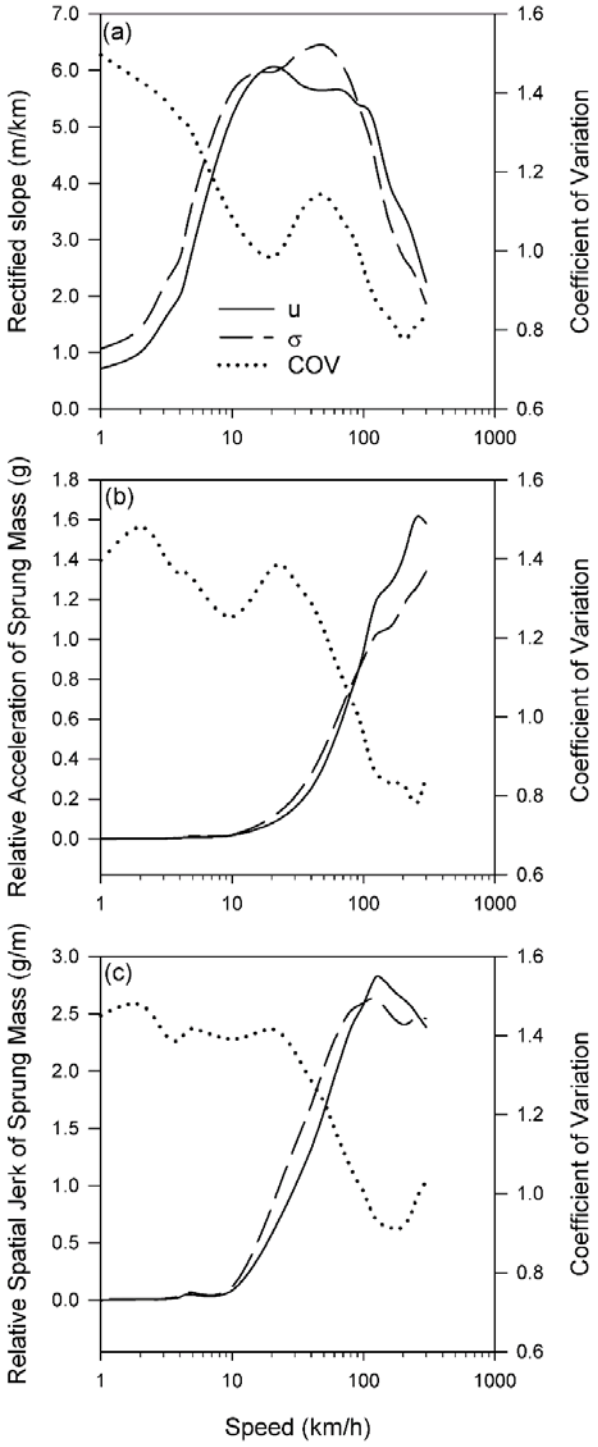

Figure 16. "Rough" pavement index parameters as a function of speed: (a) rectified slope; (b) acceleration; and (c) spatial jerk.

Acceleration increased in both sections with increase in the speed, reaching an oblique asymptote in the given domain; however, the same interaction with the profile input is apparent, where the inflection points in the curves are different. The spatial jerk seems to reach a horizontal asymptote for the “smooth” section and a peak followed by a slight decrease for the “rough” section. It is clear that the spatial jerk is the derivative of acceleration; however, it is as clear as the relationship between the rectified slope and acceleration because differentiation is done at each point and not on the curve itself and the variability between points is confounded between the two curves.

In all curves, it can be seen that the calculated standard deviation is very high, where sometimes it exceeds the mean value of all the readings. To get a better sense of high standard deviation, the normalised standard deviations (coefficient of variation) were plotted in the same graph, where the values were normalised by dividing over the mean.

Summary and Conclusions

Stationary laser scanning techniques were used to acquire 3D point clouds of pavement surfaces. These clouds were then filtered to remove noise and arranged to form the input for the algorithms developed herein to quantify surface roughness. The point coordinates were processed in three stages: visioning, simulation and indexing. In the visioning stage, PCA was used to identify the longitudinal direction and then global curves were corrected. Next, the points were arranged in grids to simplify the analysis and reduce the large number of points to be analysed. Quarter-car model simulation was then performed by passing each strip (i.e., wheel track) in the domain in the longitudinal direction to produce a response space that describes the vehicle dynamics. Based on the results obtained from the simulation, surface maps were produced in the last stage that assign one of three indices to each point on

the road surface (rectified slope, acceleration and spatial jerk). Speed effect on the results was investigated as part of the study.

At this stage, high resolution terrestrial laser scans are time-consuming and require trained personnel; however, this technique is encouraged for field evaluation during construction, especially when measurements cannot be obtained (i.e., fresh PCC pavements that cannot support the weight of a profiler) or for monitoring purposes where the locations of certain features are of interest. In the near term, newer terrestrial laser scanners will be able to reduce the data acquisition time significantly due to faster scanning rates and longer ranges. Further, other laser scanning devices, such as mobile laser scanners and UAV laser scanners, might be a faster alternative to acquire laser scans. The analysis algorithms presented in this paper are appropriate for any such 3D data set.

Based on the analysis conducted the following conclusions can be drawn:

- Three dimensional laser scanning techniques are powerful tools to provide detailed measurements, and can be used in the analysis of pavement roughness characterisation.
- The analysis was automated, and it can be developed further to be fully autonomous starting from the scanning stage.
- The proposed analysis technique can be used to identify localized rough features.
- Filtering of the profiles in Fourier space as a tool to get the spatial indices suffer from errors induced by the boundary conditions and high randomness in the input profile.
- IRI is highly variable across the width of the section for relatively short sections.
- Each index (rectified slope, acceleration, and spatial jerk) holds different information than the other indices and has its own significance.

- There is a high interaction between the speed effect and the profile, where each section would have unique curves of the indices vs. speed.
- The proposed technique warrants additional development and verifications to be standardized and used as a valuable tool for evaluating rideability and smoothness of road surfaces.

Work Cited in Chapter 2

Ahlin, K., and Granlund, N. J. (2002). "Relating road roughness and vehicle speeds to human whole body vibration and exposure limits." *International Journal of Pavement Engineering*, 3(4), 207-216.

ASTM E1926-08 (2015). "Standard Practice for Computing International Roughness Index of Roads from Longitudinal Profile Measurements." ASTM International, West Conshohocken, PA, 2015, www.astm.org.

Attoh-Okine, N. O. (2001). "Grouping Pavement Condition Variables for Performance Modeling Using Self-Organizing Maps." *Computer-Aided Civil and Infrastructure Engineering*, 16(2), 112-125.

Bogsjö, K., and Rychlik, I. (2009). "Vehicle fatigue damage caused by road irregularities." *Fatigue & Fracture of Engineering Materials & Structures*, 32(5), 391-402.

Byrne, M., Albrecht, D., Sanjayan, J., and Kodikara, J. (2009). "Recognizing patterns in seasonal variation of pavement roughness using minimum message length inference." *Computer-Aided Civil and Infrastructure Engineering*, 24(2), 120-129.

Chang, J.-R., Chang, K.-T., and Chen, D.-H. (2006). "Application of 3D laser scanning on measuring pavement roughness." *ASTM Journal of Testing and Evaluation*, 34(2), 83-91.

E950M-09, A. E. "Standard Test Method for Measuring the Longitudinal Profile of Traveled Surfaces with an Accelerometer Established Inertial Profiling Reference."ASTM International, West Conshohocken, PA, 2008, www.astm.org.

Fernando, E., Walker, R., and Mikhail, M. (2014). "Comparative testing of lasers for ride quality measurement on hot-mix asphalt pavements." *Transportation Research Record: Journal of the Transportation Research Board*, 2457, 19-29.

Fernando, E. G., and Walker, R. S. (2013). "Impact of changes in profile measurement technology on QA testing of pavement smoothness: Technical Report."Alexandria, VA: National Technical Information Service., 188p.

Fu, P., Lea, J. D., Lee, J. N., and Harvey, J. T. (2013). "Comprehensive evaluation of automated pavement condition survey service providers' technical competence." *International Journal of Pavement Engineering*, 14(1), 36-49.

Gao, H., and Zhang, X. (2013). "A Markov-based road maintenance optimization model considering user costs." *Computer-Aided Civil and Infrastructure Engineering*, 28(6), 451-464.

Gillespie, T., Sayers, M., and Segel, L. (1980). "Calibration of response-type road roughness measuring systems." Washington, DC: Transportation Research Board, National Research Council, NCHRP Report 228, Available from: http://www.trb.org/Publications/Pages/262.aspx.

Herabat, P., and Songchitruksa, P. (2003). "A decision support system for flexible pavement treatment selection." *Computer-Aided Civil and Infrastructure Engineering*, 18(2), 147-160.

Jolliffe, I. (2005). *Principal component analysis*, Wiley Online Library. doi:10.1002/0470013192.bsa501.

Kuo, C. M., Fu, C. R., and Chen, K. Y. (2011). "Effects of Pavement Roughness on Rigid Pavement Stress." *Journal of Mechanics*, 27(1), 1-8.

Laurent, J., Savard, Y., and Lefebvre, D. (2014). "3D laser road profiling for the automated survey of road surface conditions and geometry." *The 17th IRF World Meeting & Exhibition*, Proceedings of the Institute of Radio Engineers, 30. Riyadh, Saudi Arabia, November.

Liu, C., and Herman, R. (1998). "Road profiles, vehicle dynamics, and human judgment of serviceability of roads: spectral frequency domain analysis." *Journal of transportation engineering*, 124(2), 106-111.

Liu, C., and Herman, R. (1999). "Road profile, vehicle dynamics, and ride quality rating." *Journal of Transportation Engineering*, 125(2), 123-128.

Loizos, A., and Plati, C. (2008). "An alternative approach to pavement roughness evaluation." *International Journal of Pavement Engineering*, 9(1), 69-78.

Marcondes, J., Burgess, G. J., Harichandran, R., and Snyder, M. B. (1991). "Spectral analysis of highway pavement roughness." *Journal of transportation engineering*, 117(5), 540-549.

Oijer, F., and Edlund, S. (2004). "Identification of transient road obstacle distributions and their impact on vehicle durability and driver comfort." *Vehicle System Dynamics*, 41, 744-753.

Ouyang, W., and Xu, B. (2013). "Pavement cracking measurements using 3d laser-scan images." *Measurement Science and Technology*, 24(10), 105204.

Ouyang, Y., and Madanat, S. (2004). "Optimal scheduling of rehabilitation activities for multiple pavement facilities: exact and approximate solutions." *Transportation Research Part A: Policy and Practice*, 38(5), 347-365.

Rahim, A. M., Fiegel, G., Ghuzlan, K., and Khumann, D. (2009). "Evaluation of international roughness index for asphalt overlays placed over cracked and seated concrete pavements." *International Journal of Pavement Engineering*, 10(3), 201-207.

Sayers, M. W., Gillespie, T. D., and Paterson, W. D. (1986). "Guidelines for conducting and calibrating road roughness measurements." *Technical Report UMTRI-84-13, Washington, DC: The World Bank.*

Sayers, M. W., Gillespie, T. D., and Queiroz, A. (1986). "The international road roughness experiment. Establishing correlation and a calibration standard for measurements." *Technical Report HS-039 586, Washington, DC: The World Bank.*

Sayers, M. W., and Karamihas, S. M. (1996). "Interpretation of road roughness profile data." University of Michigan Transportation Research Institute.

Stein, E. M., and Shakarchi, R. (2011). *Fourier analysis: an introduction*, Princeton University Press.

Steinwolf, A., Giacomin, J., and Staszewski, W. (2002). "On the need for bump event correction in vibration test profiles representing road excitations in automobiles." *Proceedings of the Institution of Mechanical Engineers, Part D: Journal of Automobile Engineering*, 216(4), 279-295.

Sun, L. (2003). "Simulation of pavement roughness and IRI based on power spectral density." *Mathematics and computers in simulation*, 61(2), 77-88.

Tsai, Y. J., Wu, J., Wang, Z., and Hu, Z. (2010). "Horizontal roadway curvature computation algorithm using vision technology." *Computer-Aided Civil and Infrastructure Engineering*, 25(2), 78-88.

Tsunokawa, K., and Schofer, J. L. (1994). "Trend curve optimal control model for highway pavement maintenance: Case study and evaluation." *Transportation Research Part A: Policy and Practice*, 28(2), 151-166.

Wand, M. (1997). "Data-based choice of histogram bin width." *The American Statistician*, 51(1), 59-64.

Zalama, E., Gómez-García-Bermejo, J., Llamas, J., and Medina, R. (2011). "An effective texture mapping approach for 3D models obtained from laser scanner data to building documentation." *Computer-Aided Civil and Infrastructure Engineering*, 26(5), 381-392.

Zhang, C., and Elaksher, A. (2012). "An Unmanned Aerial Vehicle-Based Imaging System for 3D Measurement of Unpaved Road Surface Distresses1." *Computer-Aided Civil and Infrastructure Engineering*, 27(2), 118-129.

CHAPTER 3. QUANTIFYING UNPAVED ROAD ROUGHNESS FROM TERRESTRIAL LASER SCANNING

A paper accepted by The *Transportation Research Record: Journal of the Transportation Research Board*

Ahmad Alhasan[1,2,3], David J. White[4], Kris De Brabanter[5]

Abstract

Unpaved roads represent a major component of the roadway network in Iowa and require regular surface grading to control roughness (e.g., corrugation). This paper presents a study that shows how terrestrial laser scanning can characterize road roughness in terms of (1) spatially analyzed international roughness index (IRI); (2) fast Fourier transform (FFT) spectral analysis; and (3) surface texture characterization using statistical analysis. Algorithms are presented for each of the roughness calculations. The spatial nature of terrestrial laser scanning makes it possible to determine IRI values along any selected path within the scan area. In this study, median IRI values were used to characterize overall road roughness. To characterize the nature of road roughness, FFT was used to decompose the laser scan height spectrum. Examples are presented for unpaved road sections with a relatively smooth surface, a smooth surface with corrugations, an unsystematically rough surface, and an unsystematically rough surface with corrugations. Based on the observation

[1] Graduate research assistant, Department of Civil, Construction, and Environmental Engineering, Iowa State University.
[2] Primary researcher and author.
[3] Author for correspondence.
[4] Richard L. Handy Professor of Civil Engineering, Department of Civil, Construction, and Environmental Engineering, Iowa State University.
[5] Assistant Professor, Department of Statistics, Department of Computer Science, Iowa State University.

that the surface aggregate materials were segregated, selected small regions were studied using a 0.5 mm point spacing scan. These scans were filtered and statistically analysed for variations in height using root mean square, skewness, and kurtosis parameters. These parameters were studied in relationship to the particle size index values for the surface materials for three distinct gradations. The algorithms presented will be of value to terrestrial laser scanning users who are interested in characterizing unpaved roadway conditions.

Key words: unpaved roads, laser scanning, international roughness index, algorithms

In 2012, over one third of the roadway network in the U.S was unpaved, and in Iowa approximately 72,000 of 115,000 miles were unpaved (Bureau of Transportation Statistics 2015; Research and analytics 2012). Road geometry (e.g., curves, cross sections) and the surface quality of unpaved roads (e.g., corrugation, loose aggregate, ruts, potholes) are the major features that affect road users' travel experience, safety, and vehicle operating costs (Archondo-Callao 2007; McDonald and Sperry 2013).

The International Roughness Index (IRI) is widely used to assess paved roads because it is stable and correlates well with rideability and vehicle operating cost (Dewan and Smith 2002; Gao and Zhang 2013; Ouyang and Madanat 2004; Sayers and Karamihas 1996). Surface features are classified on a scale that ranges from less than 0.5 mm (microtexture); 0.5 to 50 mm (macrotexture); 50 to 500 mm (megatexture); and 500 mm to 50 m (gigatexture). In contrast, IRI values are classified by wavelengths on a scale from 0.1 to 100 m (i.e., classified as megatexture or gigatexture). As such, IRI values cannot be assigned to the wavelengths of aggregates or loose materials that typically fall below 50 mm (i.e.,

classified macrotexture or microtexture) (2003). Several studies have pointed out the importance of precise assessment of unpaved road conditions to help transportation agencies decide whether to maintain or upgrade these roads (Archondo-Callao 2007; Huntington and Ksaibati 2011; McDonald and Sperry 2013; Zimmerman and Wolters 2004). However, despite the lack of a common set of criteria, many local agencies use visual inspection to estimate an IRI value (Archondo-Callao 1999; Walker et al. 2002). Some agencies combine visual inspection with direct measurement of defects (e.g., pothole depth, corrugation spacing) (Soria and Fontenele 2003; Woll et al. 2008).

Researchers have evaluated non-contact, wide-footprint sensors and multi-point height sensors that obtain elevations across tire width unlike traditional profilers where elevations are acquired along a line (Fernando and Walker 2013; Fernando et al. 2014). Indirect data acquisition methods such as unmanned aerial vehicles (UAV), ground penetrating radar (GPR), and accelerometers have been explored for use on unpaved roads (Berthelot et al. 2008; Brown et al. 2003; Zhang 2009). Zhang and Elaksher (Zhang and Elaksher 2012) used a UAV-based digital imaging system to create 3D surface models and developed algorithms to extract and characterize road features, but they did not assign IRI values.

Abbas et al. (Abbas et al. 2007) used X-ray computed tomography to investigate the effectiveness of different mathematical methods in describing the 3D surface texture of Portland cement concrete pavements. Flintsch et al. (Flintsch et al. 2003) compared two indirect data acquisition systems, a circular texture meter and a laser inertial road profiler, to measure the macrotexture of hot mix asphalt pavement and concluded that the circular texture meter correlated better with the sand patch measurement described in ASTM E-965. Chang et al. (Chang et al. 2006) is the only study reported in the literature to use a terrestrial

3D laser scanner on a paved road to acquire data points. These data were used to systematically and accurately identify surface distresses and generate sample profiles for IRI ratings that were verified by matching results obtained from an inertial profiler. The accuracy and the ability of the terrestrial 3D scanner to generate multiple profiles suggest this as a promising approach to evaluate unpaved roads.

Laser scanning, or light detection and ranging (LIDAR) systems use a laser beam to measure spatial coordinates in three-dimensional (3D) space by calculating the travel time and angles of incident and reception. The spatial coordinates are then stored in a 3D point cloud. LIDAR technology includes airborne laser scanning devices, mobile scanners, and terrestrial laser scanners. The main advantage of terrestrial laser scanning is the ability to generate a rich high resolution 3D point cloud for selected road sections. The data enables the detection of localized features and distresses, however it requires training demand relatively high data storage capacity, and involves specialized techniques for detailed post processing.

The study reported here used data from a 3D terrestrial laser scanner to develop 2D surface maps of rectified slopes (RS) that were averaged in the longitudinal direction to calculate IRI values across road sections. Fast Fourier transform (FFT) spectral analysis of scanned height values revealed that sources of road roughness can be quantified. Further, a method for quantifying surface textures is presented and related to laboratory-confirmed gradations of loose surface material. These analysis methods should be of interest to users of laser scanners and engineers who want to better understand the range of surface features from 0.5 mm to 50 m (macrotexture to unevenness) of unpaved roads.

Methods

Data Acquisition

A Trimble CX 3D light detection and ranging (LIDAR) device was used to acquire data points. This system works by sending laser pulses and measuring ranges based on the time and angle of the reflected pulse. The CX 3D collects 50,000 points per second and has 360° x 300° field of view and 80 m range, but 50 m is the furthest distance for acquiring representative measurements. Scan density (the distance between measured points) is defined as adjacent points spaced at 100 m. The position accuracy of a single point is 4.5 mm at 30 m and drops to 7.3 mm at 50 m. The distance accuracy is 1.2 mm at 30 m and drops to 2 mm at 50 m.

The main components of the set-up are the scanning device, tripod, power supply, a tablet to control and store acquired data, and spherical targets for using multiple stations (Figure 17).

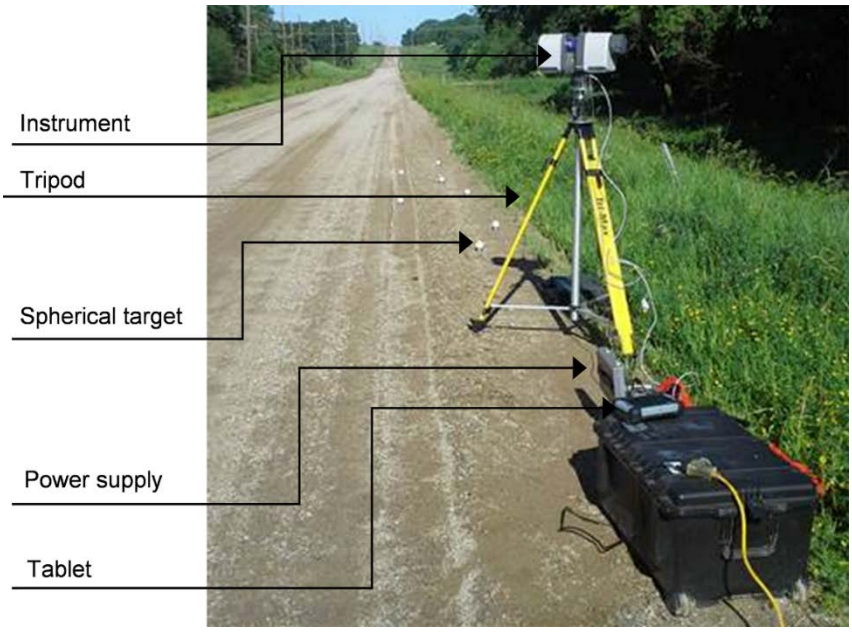

Figure 17. Trimble CX 3D laser scanner set-up.

In this study, scans were performed on two 55 m long rural road sections, 160th and 170th Streets, near Ames, Iowa. The streets serve residential areas and farms with a few agricultural facilities. The surface materials are classified as A-1-a to A-1-b, and generally the sections were well maintained and bladed on a regular basis (~ weekly). Both sections evaluated in this study were scanned within two days after blading with a motor grader. Two stations 15 m apart were selected to cover the full 55 m, and three stages of scanning were applied at each station. A full 3D scan was performed in the first stage to acquire data points for all objects within range in the field of view. The density of the full scan was 55 mm at 100 m. In the second stage, high density (30 mm at 100 m) area scans were performed to capture the megatexture of the road surface. The third stage acquired denser area scans (15 mm at 100 m) on small patches to capture macrotexture data for surface texture analysis. Gravel material from the patch areas was carefully scraped from the surfaces to obtain representative samples for particle size distribution analysis.

Analysis Approach

After the three scanning stages, scans were registered in Trimble RealWorks for initial processing and segmentation. Registration overlaps the scans obtained at different stations to construct a 3D point cloud (Figure 18). The spherical targets appearing in the data acquired at both stations make it possible to combine multiple scans into one spatially referenced dataset. Unwanted details (e.g., data points outside the area of interest and those reflected from passing vehicles) were removed from the cloud, then the x, y, and z coordinates of points that represent the road surface were exported to an ASCII file.

Figure 18. Registered point cloud for data acquired from two stations.

IRI Road Roughness

ASCII files were imported into MATLAB and processed to construct a grid with 100 mm elements in both the x and y directions. The center point of each grid element had an elevation equal to the average elevation of all data points in that element. Each strip in the longitudinal direction was considered a profile.

The quarter-car model described in ASTM E1170-97 was used to simulate vehicular response along each longitudinal profile. This model quantifies rectified slopes at each point along a profile and was run on all profiles across the surface grids. The combined response profiles produced a 2D rectified slope map that was attached to the surface grid. This dynamic system can be thought of as a mechanical filter that attenuates frequencies that correspond to the strokes absorbed by suspension systems and amplifies frequencies where the vehicle body resonates (Sayers and Karamihas 1996).

Figure 19 presents a schematic of the quarter-car model. The schematic shows a two degrees of freedom model where both sprung (M_s) and unsprung (M_u) masses move in the z-direction.

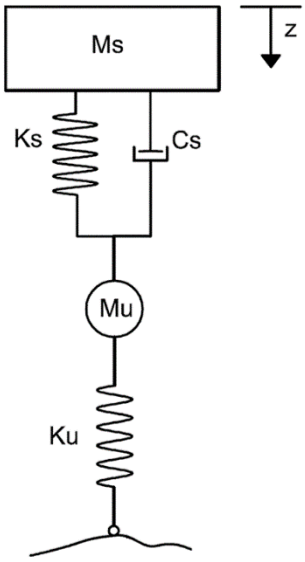

Figure 19. Quarter-car model (Alhasan 2015).

Equation 1 is the differential equation of motion used in analyzing the models response. A FORTRAN code is provided in ASTM E1926-08 to solve this equation. The code was translated to a MATLAB code and incorporated in the algorithm that produces 2D rectified slope maps by looping over all profiles.

$$\dot{X} = AX + B h_{ps} \tag{1}$$

where

$$X = \begin{bmatrix} z_S & \dot{z}_S & z_u & \dot{z}_u \end{bmatrix}^T$$

$$A = \begin{bmatrix} 0 & 1 & 0 & 0 \\ -k_2 & -c & k_2 & c \\ 0 & 0 & 0 & 1 \\ \frac{k_2}{\mu} & \frac{c}{\mu} & -\frac{(k_1+k_2)}{\mu} & -\frac{c}{\mu} \end{bmatrix}$$

$$B = \begin{bmatrix} 0 & 0 & 0 & k_1/\mu \end{bmatrix}^T \quad (2)$$

The dot indicates the time derivative, h_{ps} is the elevation of the profile after applying the moving average smoother, z_s is the elevation of the sprung mass, z_u is the elevation of the unsprung mass, k_1 is the tire spring coefficient divided by the sprung mass, k_2 is the suspension spring coefficient divided by the sprung mass, c is the suspension damping rate divided by the sprung mass, and μ is the ratio of unsprung to sprung mass.

Rectified slope is defined mathematically as the absolute difference in elevation between the sprung and unsprung masses over the distance between the two points, and the average of all rectified slope values along a profile is the IRI. Median values are calculated to represent the road roughness. For unpaved roads, wheel paths and lanes are ill-defined and normally drivers maneuver between lanes to avoid potholes or ruts, thus it is proposed examine IRI values for profiles across the full road width.

FFT Spectral Road Roughness

To further characterize the nature of road roughness, FFT was used to decompose the laser scan height spectrum into the constituent sinusoids (Broughton and Bryan 2011; Liu and Herman 1998). Before applying the FFT on the profiles, global curves were removed and the deviation for all points was measured from the fitted line representing the global curve. Global curves represent the designed vertical curve, which can be assumed as a second

degree polynomial. This step is crucial because all points have high altitudes from the assumed origin surface, and the distance between the lowest point and the origin appear in the analysis as a high amplitude component at frequency zero. Results for the FFT analysis were characterized by examining the height amplitude versus spatial frequency plots.

Based on the results, sections of unpaved road surfaces were identified with the following roughness features:

- a relatively smooth surface,
- a smooth surface with corrugations,
- an unsystematically rough surface, and
- an unsystematically rough surface with corrugations.

Characterizing the roughness in these terms brings meaning to the surface condition assessment and is a link to the source of IRI road roughness.

Surface Texture Analysis

Three patches were densely scanned to analyze macrotexture features, and the points in these scans were spaced at about 0.5 mm. The scans acquired megatexture information so a 2D high pass filter was applied on the data. High pass filtering was done by applying a low pass filter (smoother) and subtracting the filtered surface from original data as described in Equation 3.

$$P_H(x, y) = P(x, y) - P_L(x, y) \tag{3}$$

Where, P is an original data point defined at x and y, P_H is a high pass filtered data point, and P_L is a point projected on a smoothed-mean surface. A thin-plate smoothing spline was

used to fit that surface from the original data. Due to the large number of points in a scan, points were sampled to reduce the processing time for surface smoothening. Figure 20 shows the sampled points in a patch with the fitted surface.

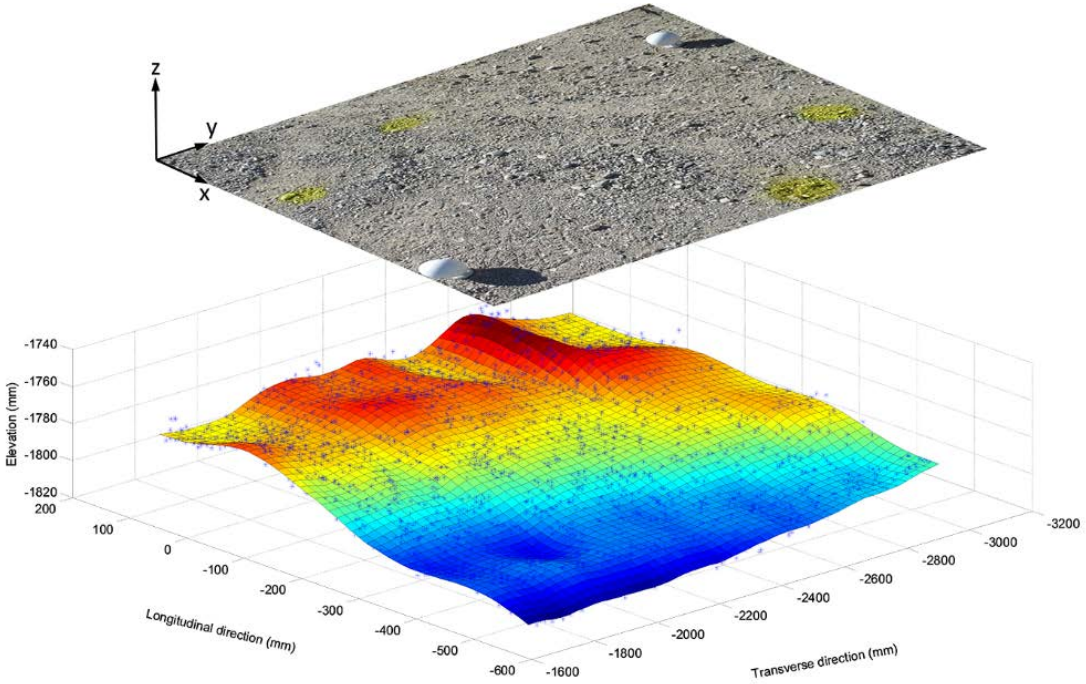

Figure 20. Photo of the scanned area (top) and the smoothed surface showing sampled points (3D representation).

After filtering the data, all points were shifted to a mean zero plane to simplify areal field analysis in three categories: function, height, and volume characteristics. However function-related data were specifically developed to characterize machined surface roughness so this category was outside the scope of this study (Blateyron 2013). Height parameters include: root mean square height (S_q), skewness (S_{sk}), and kurtosis (S_{ku}). Root mean square height (Equation 4) is equal to the standard deviation.

$$S_q = \sqrt{\frac{1}{n_x n_y} \sum_{y=0}^{n_y-1} \sum_{x=0}^{n_x-1} z(x,y)^2} \tag{4}$$

Where n_x and n_y represent the spacing between points in x and y directions respectively, for equally spaced points in both directions $n_x n_y$ reduces to the total number of points, and z is the elevation of the point measured from the mean plane.

Skewness is a unitless parameter that represents bias in height distribution about the zero plane (Equation 5). Gaussian surfaces have zero skewness ($S_{sk} = 0$). Negatively skewed surfaces ($S_{sk} < 0$) would have more peaks, and positively skewed surfaces would have more valleys.

$$S_{sk} = \frac{1}{S_q^{\,3}} \frac{1}{n_x n_y} \sum_{y=0}^{n_y-1} \sum_{x=0}^{n_x-1} z(x,y)^3 \tag{5}$$

Equation 6 is the mathematical formula for surface kurtosis. This parameter is positive and unitless. Gaussian surfaces have a kurtosis equal to 3,and smaller values indicate a spiky surface and larger values indicate bumpy surfaces.

$$S_{ku} = \frac{1}{S_q^{\,4}} \frac{1}{n_x n_y} \sum_{y=0}^{n_y-1} \sum_{x=0}^{n_x-1} z(x,y)^4 \tag{6}$$

Height distribution and material ratio curves were also developed for the patches. Height distribution is a histogram calculated across the height. The normalized integral of a histogram yields the material distribution curve.

Results and Discussion

Road Roughness

On the rectified slope maps of 160th Street (Figure 21a) and 170th Street (Figure 21b), the left lane extends between stations 0 and 3 in the transverse distance, and the right lane extends between stations 0 and -3. These maps illustrate road roughness features. For example, the central region of 160th Street (Figure 21a) is unsystematically rough compared

to the rest of the scanned area with a localized rough region (i.e., a loose pile of aggregate) in the left lane between stations 50 and 55. 170th Street (Figure 21b) shows that the section is smoother overall with a few defined ridges.

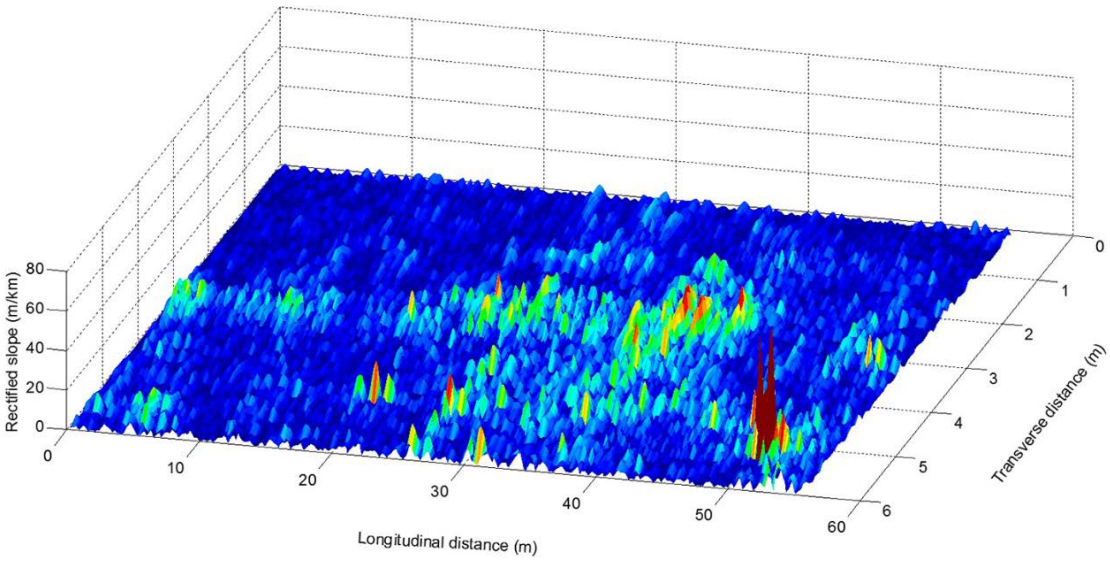

(5a)

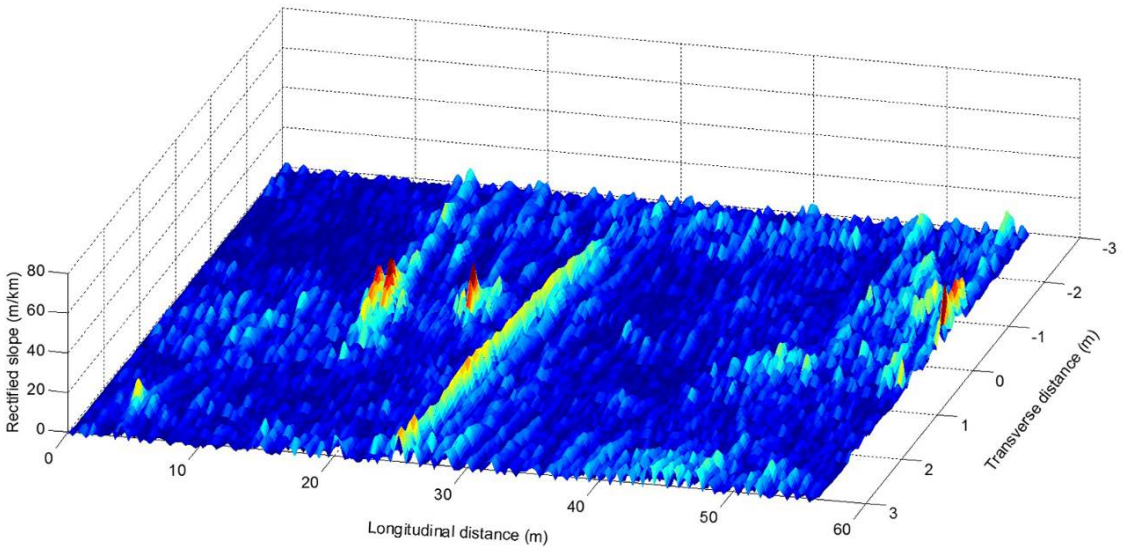

(5b)

Figure 21. Rectified slope maps for 160th Street (5a) and 170th Street (5b).

The IRI value of each longitudinal profile is the average of the rectified slope values of the profile. A plot of the IRI values versus width for both roads (Figure 22) shows the variability of IRI values, and that the higher IRI values between stations -1 and 1 correspond with peaks shown on the rectified surface maps. Because IRI values vary widely, plots of IRI versus width may better describe surface roughness, and, if a single summary index is needed, median IRI values may better describe overall roughness than average IRI values (e.g., the median IRI value of 160th Street is 2.60 m/km and is 2.36 m/km for 170th Street). Robustness to outliers would be an advantage of median IRI summary values.

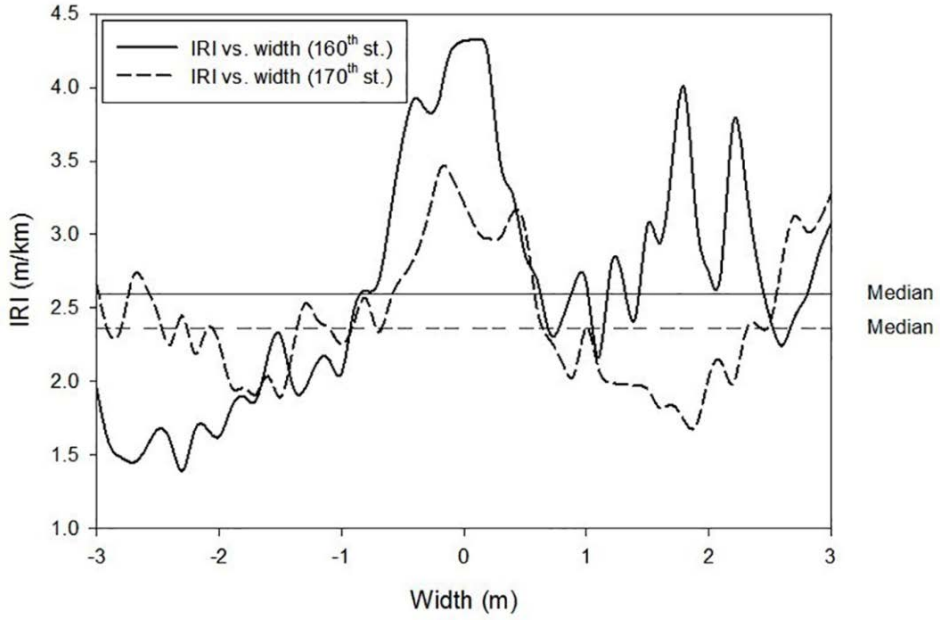

Figure 22. IRI vs. width.

FFT Spectra

To investigate variability in IRI values, two profiles were analyzed for each section, the profile corresponding to maximum IRI value and the profile corresponding to minimum IRI value. Each profile was decomposed into its constituent spectrum using the FFT. Presenting

the results as height amplitude versus spatial frequency clearly shows different components of amplitude and frequency. The threshold for “smooth” was set at amplitude less than 0.4 mm. “Unsystematically rough” is defines as amplitude greater than 0.4 mm, but variable over a range of spatial frequencies. “Corrugation” is defined as amplitude with a central peak of greater than 0.7 mm and a spatial frequency of 1.5 to 2.5 (1/m). By examining the results this way, the source of roughness can be distinguished. In the future, these features should be studied for links to surface material types, trafficking, environmental factors, etc.

Figure 23 clearly shows that 160th street has a smooth surface with distinct corrugations that have a wavelength of approximately 0.5 m. Also it is obvious that the profile at 0.1 m from the center is unsymmetrically rough with higher amplitude corrugations and thus it is expected to have higher IRI value than the other profile at -2.3 m. It should be noticed that these amplitudes are not always equal to the height of corrugation, the actual height is equal to the Fourier summation of different amplitudes at different frequencies. 170th street had smoother profiles, the profile at 1.9 m is relatively smooth, unlike the other profile at -0.2 m that is unsystematically rough.

One explanation of higher corrugation in the middle of the road would be the higher thickness of loose gravel (Mahgoub et al. 2011). It was observed that the routine surface grading for this road left more loose material than the outside edges in a crown for drainage.

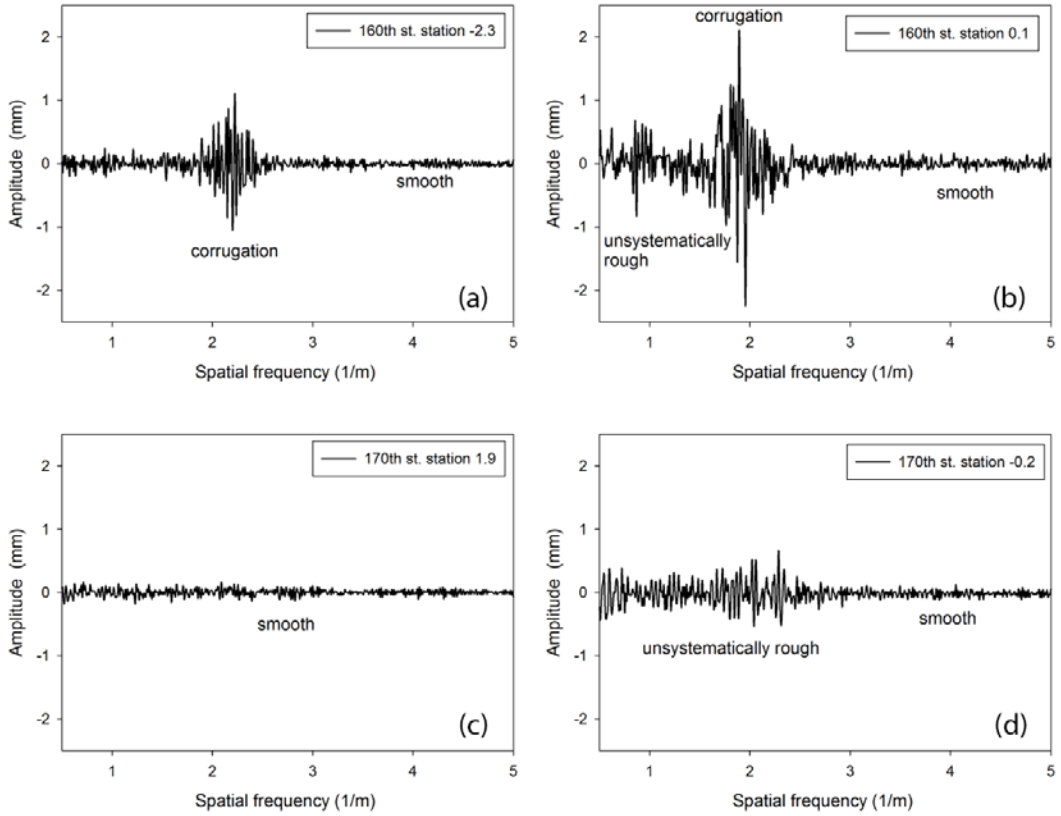

Figure 23. FFT for road profiles in (a) smooth surface with corrugations, (b) unsystematically rough surface with corrugations, (c) relatively smooth surface, and (d) unsystematically rough surface.

Surface Texture

The three patches under consideration were labelled T.P1, T.P2, and T.P3. Loose surface materials were scraped gently after scanning and particle size analysis was performed on the collected material. Figure 24 shows the grain size distribution curves of the material. T.P3 is the finest graded material and T.P2 is the coarsest. According to AASHTO classification materials in T.P1 and T.P2 are A-1-a, and material in T.P3 is A-1-b class, based on that and the uniformity coefficient, T.P2 is the most well graded and T.P3 has the poorest gradation relative to others.

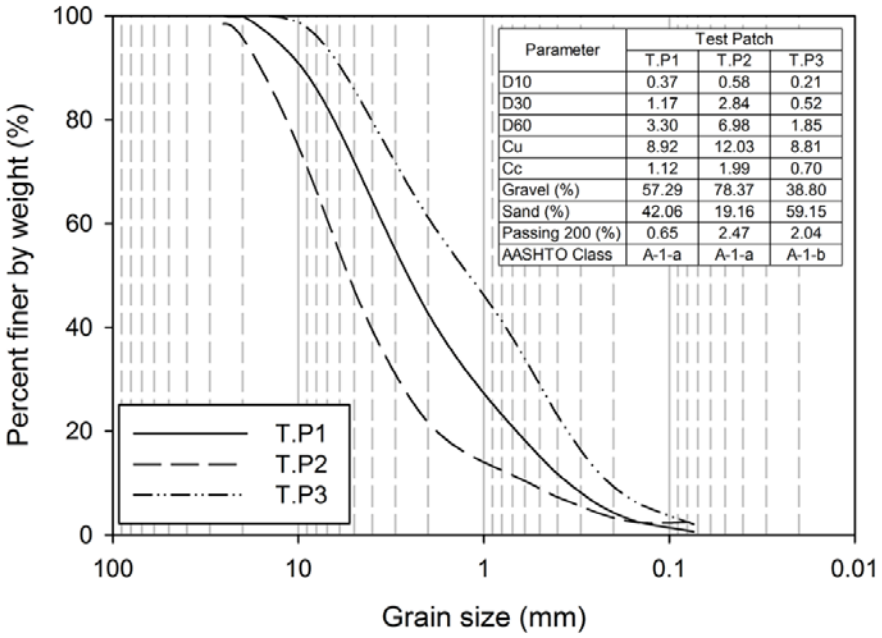

Parameter	Test Patch		
	T.P1	T.P2	T.P3
D10	0.37	0.58	0.21
D30	1.17	2.84	0.52
D60	3.30	6.98	1.85
Cu	8.92	12.03	8.81
Cc	1.12	1.99	0.70
Gravel (%)	57.29	78.37	38.80
Sand (%)	42.06	19.16	59.15
Passing 200 (%)	0.65	2.47	2.04
AASHTO Class	A-1-a	A-1-a	A-1-b

Figure 24. Grain size distribution of surface material for the three patches.

Figure 25 shows the test patch scans with the calculated height parameters. Total height indicates the extent of particles protruding from the surface. From the gradation analysis. T.P3 had the smallest maximum and nominal aggregate size and accordingly had the smallest total height. T.P1 and T.P2 had equal nominal aggregate size, however the largest aggregate size was different and thus there is a slight difference in the total height. Based on that it can be seen that total height is more sensitive to nominal aggregate size and still could detect the maximum aggregate size.

The root mean square (S_q) relates to the spread of material across the height—surfaces with low S_q values have more material lumped in a small height range as compared to surfaces with high S_q values. Comparing S_q with grain size distribution shows that with higher uniformity coefficient S_q values are lower. S_{sk} reflects the primary surface texture where peak dominant surfaces have positive values while valley dominant surfaces have negative values. Surfaces dominated by peaks are expected to form by lifting aggregate and

forming a layer of loose aggregates, on the other hand surfaces dominated by valleys are expected to form by loss of fines where coarse particles remain intact while fine particles get removed. Since all test patches have S_{ku} greater than 3, there are peaks, and T.P1 has the most extreme peaks relative to others. This finding supports the field observations.

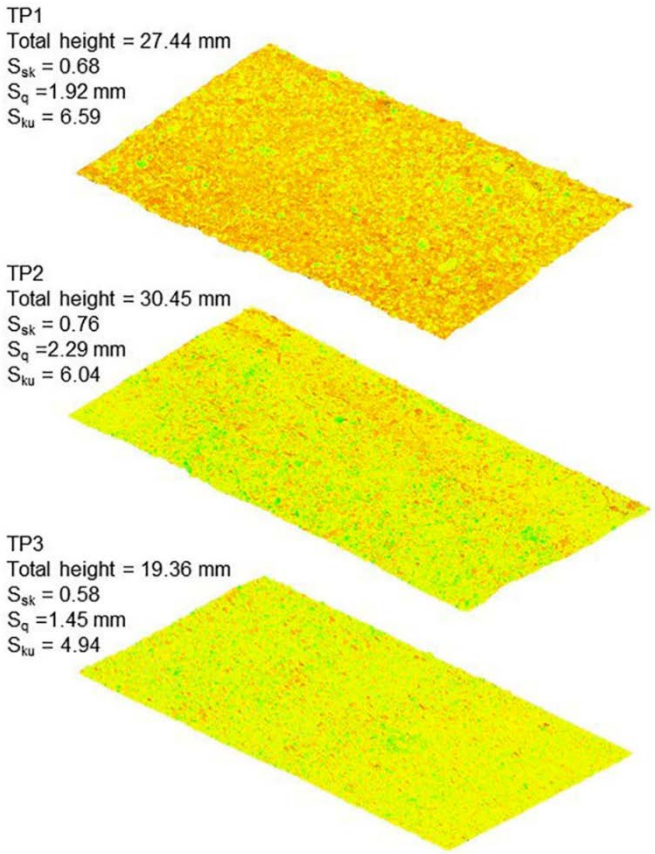

Figure 25. 3D surfaces for the three patches with the calculated areal parameters.

Height distribution and material ratio curves (Figure 26) provide a visual mean to better understand the properties of surface materials. It can be seen that T.P3 had the narrowest distribution curve, and this coincides with the root mean square height values. Skewness relates to the symmetry and bias in distribution curves. Kurtosis higher than 3 defines a peaked distributions while lower kurtosis value defines flat distributions. The last two

parameters are hard to detect visually. It should be mentioned that the size of the histogram does not hold significant information for scans with equal densities, it only relates to the number of points included in the calculation, and thus the size of the patch.

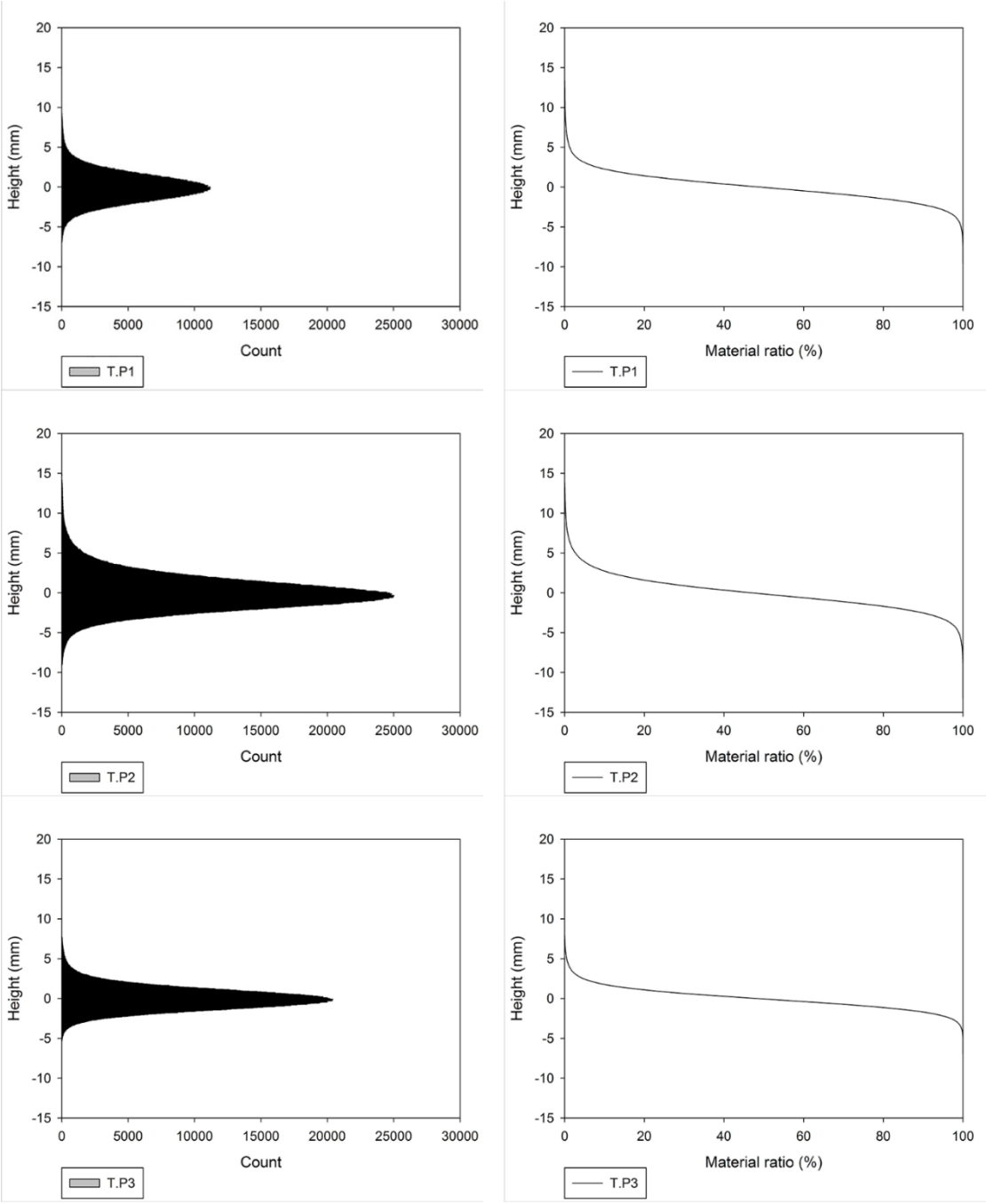

Figure 26. Height distribution and material ratio curves.

Material ratio curves present the cumulative material points above a cutting plain at a given height. The slope of the middle region in these curves relates to the smoothness of a surface, where lower slopes mean that all measured points appear in a narrow height range and thus the surface would be smoother. The curves indicate that the slopes decrease as materials get finer.

Conclusions

This paper introduces quantitative techniques for evaluating the surface roughness of unpaved roads. Methods for characterizing the surface roughness were presented in terms of three different analysis techniques: IRI, FFT, and statistical analysis of height measurements. The key findings from this research are:

- Dense point clouds of x,y,z data obtained from terrestrial laser scanning is a promising technology to assess a range of surface conditions for unpaved roads.
- Spatial surface roughness maps were developed using the information obtained from the point cloud data.
- Algorithms used in producing the roughness maps are semi-automated, and further developments are expected to introduce fully automated data analysis algorithms.
- Because IRI values are variable across the road section, selection of a representative profile(s) should account for this variability.
- Corrugation is a major factor that affects ride quality in the absence of other major distresses.
- Fourier analysis can identify corrugation and other forms of roughness.

- Areal field parameters hold important characteristics of the surface material, and more investigation is needed to correlate areal parameters with surface material characteristics and features.

Recommendations

At this stage, high resolution terrestrial laser scanning is time consuming and requires trained personnel; however, this technique is encouraged for field evaluations to gain better understandings of unpaved road performance. In the near term, newer terrestrial laser scanners with faster scanning rates and longer ranges will be able to significantly reduce data acquisition times. Other laser scanning devices, such as mobile laser scanners and UAV laser scanners, might be faster alternatives to terrestrial laser scanners. The analysis algorithms presented in this paper are appropriate for any 3D data set.

Work Cited in Chapter 3

Abbas, A., Kutay, M. E., Azari, H., and Rasmussen, R. (2007). "Three-Dimensional Surface Texture Characterization of Portland Cement Concrete Pavements." *Computer-Aided Civil and Infrastructure Engineering*, 22(3), 197-209.

Archondo-Callao, R. (1999). "Unpaved roads roughness estimation by subjective evaluation." *The World Bank*.

Archondo-Callao, R. (2007). "Evaluating economically justified road works expenditures on unpaved roads in developing countries." *Transportation Research Record: Journal of the Transportation Research Board*(1989), 41-49.

Berthelot, C. F., Podborochynski, D., Stuber, E., Prang, C., and Marjerison, B. "Saskatchewan case studies of network and project level applications of a structural asset management system." *Proc., Seventh International Conference on Managing Pavement Assets*.

Blateyron, F. (2013). "The Areal Field Parameters." *Characterisation of Areal Surface Texture*, R. K. Leach, ed., Springer, 15-43.

Broughton, S. A., and Bryan, K. M. (2011). *Discrete Fourier analysis and wavelets: applications to signal and image processing*, John Wiley & Sons.

Brown, M., Mercier, S., and Provencher, Y. (2003). "Road maintenance with Opti-Grade®: Maintaining road networks to achieve the best value." *Transportation Research Record: Journal of the Transportation Research Board*, 1819(1), 282-286.

Bureau of Transportation Statistics (2015). "Table 1-4: Public Road and Street Mileage in the United States by Type of Surface (Thousands of miles)." <http://www.rita.dot.gov/bts/sites/rita.dot.gov.bts/files/publications/national_transportation_statistics/html/table_01_04.html>. (February 20, 2015).

Chang, J.-R., Chang, K.-T., and Chen, D.-H. (2006). "Application of 3D laser scanning on measuring pavement roughness." *ASTM Journal of Testing and Evaluation*, 34(2), 83-91.

Dewan, S., and Smith, R. (2002). "Estimating International Roughness Index from Pavement Distresses to Calculate Vehicle Operating Costs for the San Francisco Bay Area." *Transportation Research Record*, 1816(1), 65-72.

Fernando, E. G., and Walker, R. S. (2013). "Impact of changes in profile measurement technology on QA testing of pavement smoothness: Technical Report."Alexandria, VA: National Technical Information Service., 188p.

Fernando, E. G., Walker, R. S., and Mikhail, M. "Comparative Testing of Lasers for Ride Quality Measurement on HMA Pavements." *Proc., Transportation Research Board 93rd Annual Meeting*.

Flintsch, G., de León, E., McGhee, K., and Al-Qadi, I. (2003). "Pavement Surface Macrotexture Measurement and Applications." *Transportation Research Record: Journal of the Transportation Research Board*, 1860(1), 168-177.

Gao, H., and Zhang, X. (2013). "A Markov-based road maintenance optimization model considering user costs." *Computer-Aided Civil and Infrastructure Engineering*, 28(6), 451-464.

Huntington, G., and Ksaibati, K. (2011). "Implementation guide for the management of unsealed gravel roads." *Transportation Research Record: Journal of the Transportation Research Board*, 2205(1), 189-197.

Liu, C., and Herman, R. (1998). "Road profiles, vehicle dynamics, and human judgment of serviceability of roads: spectral frequency domain analysis." *Journal of transportation engineering*, 124(2), 106-111.

Mahgoub, H., Bennett, C., and Selim, A. (2011). "Analysis of Factors Causing Corrugation of Gravel Roads." *Transportation Research Record: Journal of the Transportation Research Board*, 2204(-1), 3-10.

McDonald, T., and Sperry, R. (2013). "Evaluation of mitigation for safety concerns on low-volume, unpaved rural roads." Institute for Transportation, Iowa State University, Ames, IA.

Ouyang, Y., and Madanat, S. (2004). "Optimal scheduling of rehabilitation activities for multiple pavement facilities: exact and approximate solutions." *Transportation Research Part A: Policy and Practice*, 38(5), 347-365.

Research, and analytics (2012). "Miles of public roads in Iowa by surface type." <http://www.iowadot.gov/research/analytics/publicroads.html>. (February 20, 2015).

Sayers, M. W., and Karamihas, S. M. (1996). "Interpretation of road roughness profile data." University of Michigan Transportation Research Institute.

Soria, M., and Fontenele, E. (2003). "Field evaluation of method for rating unsurfaced road conditions." *Transportation Research Record: Journal of the Transportation Research Board*, 1819(-1), 267-272.

Walker, D., Entine, L., and Kummer, S. (2002). "Gravel-Paser Manual: pavement surface evaluation and rating." Wisconsin Transportation Information Center.

Woll, J. H., Surdahl, R. W., Everett, R., and Andresen, R. (2008). "Road stabilizer product performance: Seedskadee national wildlife refuge." *FHWA-CFL/TD-08-005*.

Zhang, C. (2009). "Monitoring the condition of unpaved roads with remote sensing and other technology." Geographic Information Science Center of Excellence, South Dakota State University.

Zhang, C., and Elaksher, A. (2012). "An Unmanned Aerial Vehicle-Based Imaging System for 3D Measurement of Unpaved Road Surface Distresses1." *Computer-Aided Civil and Infrastructure Engineering*, 27(2), 118-129.

Zimmerman, K., and Wolters, A. (2004). "Local road surfacing criteria." South Dakota Department of Transportation, Federal Highway Administration, Applied Pavement Technology, Inc.

CHAPTER 4. CONTINUOUS WAVELET ANALYSIS OF PAVEMENT PROFILES

A paper submitted to *Automation in Construction*

Ahmad Alhasan[1,2,3], David J. White[4], Kris De Brabanter [5]

Abstract

Pavement roughness can be quantified by analyzing the response of vehicle suspensions to road geometry or by analyzing basic geometric measurements (e.g., crack width and depth). These analyses can be either summative or pointwise. In recent studies, wavelet transform has been used to quantify road roughness by correlating the energies of wavebands to summative IRI values rather than identifying localized features and their effect on vehicle suspension response (SR) using quarter-car (QC) simulations. Because pointwise SR analysis can identify localized features, the objective of this study is to investigate the applicability and advantages of analyzing asphaltic and Portland cement pavements with QC simulation and continuous wavelet transform (CWT). This approach provides spatial assessment of roughness as a function of both frequency band and position and allows statistical comparisons of SR at different frequency bands. An advantage of this method is analyzing relatively short segments which can support near real-time assessment.

[1] Graduate research assistant, Department of Civil, Construction, and Environmental Engineering, Iowa State University.
[2] Primary researcher and author.
[3] Author for correspondence.
[4] Richard L. Handy Professor of Civil Engineering, Department of Civil, Construction, and Environmental Engineering, Iowa State University.
[5] Assistant Professor, Department of Statistics, Department of Computer Science, Iowa State University.

Keyword: Pavements, Surface roughness, Wavelet, Fourier analysis, Vibration, Dynamic analysis, Mathematical models, Data analysis.

Pavement surface roughness increases vehicle operation and travel delay costs (Gao and Zhang 2013; Ouyang and Madanat 2004); reduces vehicle durability (Bogsjö and Rychlik 2009; Oijer and Edlund 2004); and reduces ride quality and structural performance (Al-Omari and Darter 1994). Structural performance diminishes faster on rough roads because roughness features increase dynamic stresses that accelerate pavement deterioration (Lin et al. 2003). Accurate evaluation of pavement roughness levels and modes is a key factor in optimizing maintenance decisions (Chootinan et al. 2006; Kilpeläinen et al. 2011; Lamptey et al. 2008).

Roughness can be quantified by analyzing the response of vehicle suspensions to road geometry, using, for example, the quarter- or half-car models or actual vehicle responses, or by analyzing basic geometric measurements (e.g., crack and pothole width and depth). These analyses can be either summative (i.e., results in summary indices) or pointwise (i.e., results in a response profile or map). The most widely used summative method, the International Roughness Index (IRI), calculates the average rectified slope (i.e., vehicle suspension rate) of a pavement elevation profile, but does not provide sufficient detail to indicate the roughness mode or describe localized features (Herabat and Songchitruksa 2003; Nitsche et al. 2014; Ueckermann and Steinauer 2008).

Pointwise analysis of vehicle responses can identify localized features, but this approach is still open for research and technology development. Studies of geometry-based pointwise quantification have classified pavement features by size and extent (Cheng and Miyojim

1998; Cheng et al. 1999; Georgopoulos et al. 1995; Mahler et al. 1991). Tsai et al. (2012) developed a crack fundamental element model to extract, cluster, and classify pavement cracks. Gavilán et al. (2011) proposed a seed-based linear support vector machine approach to develop a fully automated distress classifier that uses textural properties as inputs. Radopoulou and Brilakis (2015) developed an automated system to detect road patches from video data based on the surface elevation and texture. Zalama et al. (2014) used Gabor filters and a statistical learning system that had been trained from a large database to detect longitudinal and transverse cracks. Other studies (Nejad and Zakeri 2011; Nejad and Zakeri 2011) have demonstrated the advantages of using wavelet analysis as inputs to neural network schemes in classifying pavement distresses. Bosché and Guenet (Bosché and Biotteau 2015) investigated the use of continuous wavelet transform in evaluating surface flatness based on terrestrial laser scanning data (Bosché and Guenet 2014).

Several response-based studies have used signal processing techniques, such as power spectral density (PSD) and discrete wavelet transform (DWT), to quantify pavement roughness. DWT outperformed PSD analysis in verifying road roughness features and detecting localized defects such as cracks and potholes (Hesami and McManus 2009; Shokouhi et al. 2005). Wei et al. (2005) calculated energies of wavebands and correlated these energies to IRI values. Sen et al. (2012) used wavelet analysis to assess changes in pavement elevation profile characteristics over time and linked the changes to traffic loading, climate conditions, pavement composition, and subgrade soil type.

Taken together these studies suggest that wavelet analysis is a promising technique for pavement roughness assessment, for locating problematic segments of any road, and for identifying possible causes of deterioration. Most previous wavelet analysis studies have

used pointwise analysis (i.e., decomposing profiles into wavebands) but have correlated the energies of the wavebands to summative IRI values rather than identifying localized features.

Papagiannakis et al. (2007) used DWT to analyze suspension responses obtained from a 5-axle semi-trailer truck equipped with an air suspension on the driver axle and a rubber suspension on the trailer axles. Total energies of 11 wavebands were calculated and compared with dynamic loads. Dynamic loads correlated best with sub-bands with pseudo-frequencies between 0.65 and 3.76 cycle/m. Tomiyama et al. (2014) analyzed data collected with a response-type profiler that used a lifting wavelet transform to detect and quantify pavement distresses that identified target distresses with an average accuracy of 78%.

In this paper, 30 elevation profiles of both asphalt concrete (AC) and Portland cement concrete pavements (PCC) sections obtained from the Long Term Pavement Performance (LTPP) database (2014) were analyzed with quarter-car simulations and continuous wavelet transform (CWT). The simulation results are reported as suspension rate profiles. The variance of suspension rate profiles has been used as a summary index because variance is a more common statistical parameter. The advantage of this approach is that CWT decomposes profiles in greater detail and provides spatial assessment of roughness as a function of both frequency band and position.

Continuous Wavelet Transform

Wavelet analysis techniques were developed independently in different fields (i.e., pure mathematics, physics, and engineering) to overcome the time-frequency resolution issue in Fourier analysis (Aslaksen and Klauder 1968; Boggess 2009; Calderón 1964; Daubechies 1992; Morlet 1983). This issue results from the assumption that sines and cosines, which are infinitely periodic functions, are the building blocks for any function. This assumption

induces uncertainty in the analysis, where high resolution cannot be achieved simultaneously in both the frequency and the spatial domains. Pinsky (2002) and Stein and Shakarchi (2011) reported that as the dispersion of a function in the spatial domain about a fixed point x_0 decreases (i.e., higher resolution) the dispersion of the transformed function in the frequency domain about a fixed frequency ξ_0 increases to satisfy the inequality condition expressed in Eq. 1,

$$D_0(f)D_0\left(\hat{f}\right) \geq \frac{1}{16\pi^2} \tag{1}$$

where

$$D_0(f) = \int_{-\infty}^{+\infty} (x - x_0)^2 \left| f(x) \right|^2 dx$$

$$D_0\left(\hat{f}\right) = \int_{-\infty}^{+\infty} (\xi - \xi_0)^2 \left| \hat{f}(\xi) \right|^2 d\xi$$

and f is a signal (profile) in the spatial domain represented as a function of x; $\hat{f}$ is the Fourier transform of the signal; and D_0 is the second moment about point x_0 or ξ_0.

Wavelets, which can be thought of as wave pulses that translate in the spatial domain and can change size (i.e., dilate or shrink), are used as building blocks to overcome the time-frequency resolution issue. Wavelets come in families, and for each family there is a wavelet function (mother wavelet) and a scaling function (father wavelet), although some continuous wavelet families do not include scaling functions. Wavelet dispersion is controlled by a scale factor a, where larger scale factors correspond to dilated waves and smaller scale factors correspond to shrunken waves. A wavelet function is expressed by Eq. 2, decision

$$\psi_{a,b}(x) = \frac{1}{\sqrt{a}}\psi\left(\frac{x-b}{a}\right) \tag{2}$$

where a is the translation factor, b is the position of the wavelet center, and x is a longitudinal coordinate in a profile.

In this study, CWT was used rather than DWT because DWT decomposes data into layers at widely spaced discrete frequency bands, which means that fine details at a narrow frequency band cannot be examined. However, CWT decomposes profiles into layers at closely spaced frequency bands proportional to scale factors, which means that the layers have the same length and point spacing as the elevation profile before decomposition. For CWT analysis, wavelets should satisfy two conditions: $\psi(x)$ is continuous and has exponential decay and the integral of $\psi(x)$ over all space equals zero. CWT analysis also assumes that $\psi(x)$ equals zero outside the effective support interval [-A, A]. The Morlet wavelet was used in this study because it approximates profiles within a reasonable tolerance. Eq. 3 shows the explicit form for Morlet wavelet.

$$\psi(x) = e^{\frac{-x^2}{2}}\cos(5x) \tag{3}$$

Figure 27 shows the Morlet wavelet at three scale factors. Scale factor 1.0 corresponds to the original function with no dilation or shrinkage, scale factor 2.0 corresponds to a dilated wavelet, and scale factor 0.5 corresponds to a shrunken wavelet.

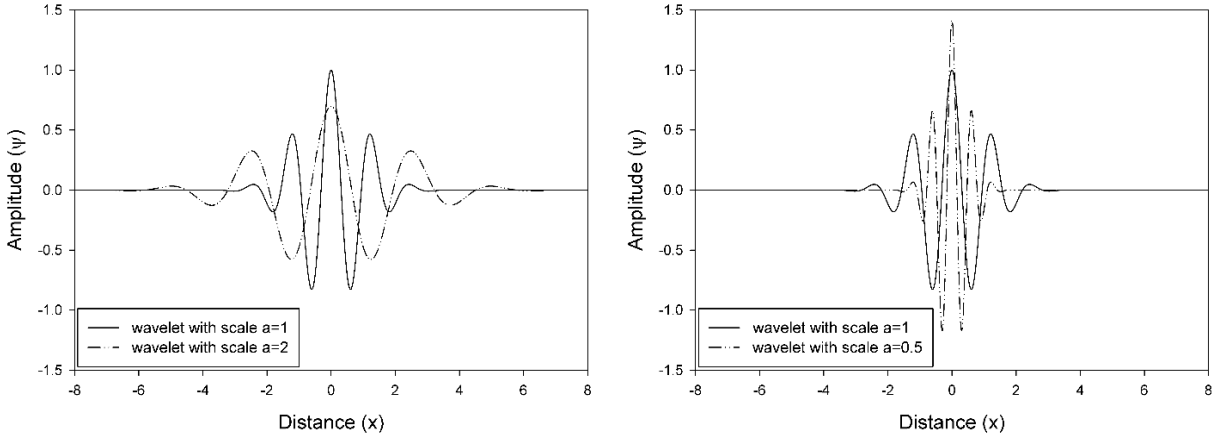

Figure 27. Morlet wavelet comparisons for different scale factors: (left) a = 1 and 2, and (right) a = 1 and 0.5.

The Fourier transform of a wavelet results in a narrow frequency band with a central frequency ξ_c. This frequency is the most dominant frequency component in a wavelet and it corresponds to the frequency of a sinusoidal wave that best matches the wavelet (Figure 28). Scale factor changes the dominant frequency of a wavelet. The new frequency is referred to as the pseudo-frequency ($\tilde{\xi}$) and is proportional to 1/*a* (Eq. 4), and the wave period ($\tilde{\lambda}$) is proportional to *a* (Eq. 5).

$$\tilde{\xi} = \xi_c / a \tag{4}$$

$$\tilde{\lambda} = a / \xi_c \tag{5}$$

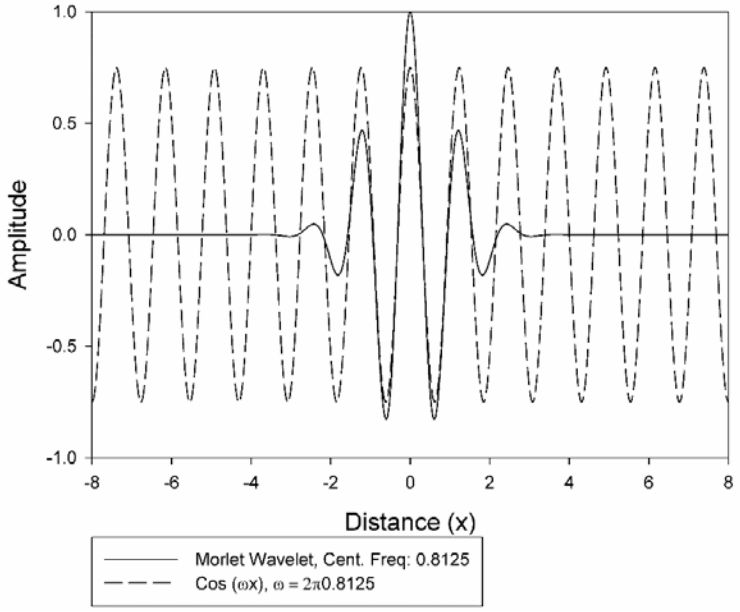

Figure 28. Morlet wavelet overlapped with sinusoidal wave (frequency = 0. 8125).

CWT transforms or projects the profile on a wavelet function at different scale factors (layers of details) to result in wavelet coefficients that describe the correlation between the signal and the wavelet function. Eq. 6 defines the wavelet transform (W_f) of a profile *f*, at a spatial coordinate *b* and onto a wavelet with a scale factor *a*. The original profile can be retrieved by applying the inverse wavelet transform as defined in Eq. 7.

$$W_f(a,b) = \left\langle \psi_{a,b} \middle| f \right\rangle = \int_{-\infty}^{+\infty} f(x)\overline{\psi}_{a,b}(x)dx \tag{6}$$

$$f(x) = \frac{1}{C_\psi}\int_{-\infty}^{+\infty}\int_{-\infty}^{+\infty} |a|^{-1/2}\psi\left(\frac{x-b}{a}\right)W_f(a,b)\frac{dbda}{a^2} \tag{7}$$

where

$$C_\psi = 2\pi\int_{-\infty}^{+\infty}\frac{|\hat{\psi}(\xi)|^2}{|\xi|}d\xi$$

and $\overline{\psi}_{a,b}(x)$ is the wavelet function complex conjugate and $\hat{\psi}(\xi)$ is the Fourier transform of the wavelet function.

Analysis Approach

Road Profiles

Thirty elevation profiles, 15 asphalt concrete (AC) and 15 Portland cement concrete (PCC) pavements, with a wide range of IRI values (0.32 m/km to 7.95 m/km) were selected from the LTPP database without regard to location or profiling date (Table 5).

Table 5. LTPP profile information.

State code	SHRP code	Pavement Type	IRI	State code	SHRP code	Pavement Type	IRI
49	A351	AC	3.23	90	6420	AC	1.78
49	C331	AC	0.76	06	B441	PCC	7.95
90	B340	AC	3.11	48	C430	PCC	2.68
01	0101	AC	0.82	49	E458	PCC	2.31
04	1062	AC	0.32	06	3005	PCC	4.71
06	8535	AC	0.93	12	4138	PCC	5.21
12	4137	AC	0.36	19	0222	PCC	2.10
25	1002	AC	4.28	19	3055	PCC	0.40
34	0502	AC	1.24	21	3016	PCC	0.65
47	3075	AC	2.09	40	0160	PCC	1.27
48	1065	AC	4.96	42	1613	PCC	1.18
51	0120	AC	1.05	42	1617	PCC	0.99
81	0503	AC	2.51	46	0661	PCC	1.20
85	1801	AC	4.80	49	7083	PCC	1.26
90	6420	AC	6.05	89	3015	PCC	2.61

CWT and Profile Decomposition

Elevation profiles were decomposed into 26 layers of detail (profile 06B441 was decomposed into 23 layers due to this pavement sections length being 44.25 m, whereas all other sections were 152.55 m). Each layer represents the projection of the elevation profile into the wavelet with scale a_j, the maximum scale value corresponds to wave period twice the

length of the profile. Table 6 represents the scale factors used and the corresponding pseudo-frequencies and pseudo-periods.

Table 6. Scale factors, pseudo-frequencies, and pseudo-periods.

Scale (a)	Pseudo-frequency, $\tilde{\xi}$ (cycle/m)	Pseudo-period, $\tilde{\lambda}$ (m)	Scale (a)	Pseudo-frequency, $\tilde{\xi}$ (cycle/m)	Pseudo-period, $\tilde{\lambda}$ (m)
0.05	16.25	0.06	4.04	0.20	4.98
0.07	11.59	0.09	5.67	0.14	6.98
0.10	8.27	0.12	7.95	0.10	9.78
0.14	5.90	0.17	11.14	0.07	13.71
0.19	4.21	0.24	15.62	0.05	19.23
0.27	3.00	0.33	21.90	0.04	26.96
0.38	2.14	0.47	30.71	0.03	37.80
0.53	1.53	0.66	43.05	0.02	52.99
0.75	1.09	0.92	60.36	0.01	74.29
1.05	0.78	1.29	84.63	0.01	104.16
1.47	0.55	1.81	118.65	0.01	146.03
2.06	0.39	2.53	166.35	<0.01*	204.74
2.88	0.28	3.55	233.22	<0.01*	287.04

Note: * values < 0.01 are too small to affect vehicle response

Elevation profile decomposition and reconstruction were performed in Matlab (2013). The algorithm calculates the wavelet coefficient at each point for all scale factors. To acquire a layer at a scale factor a_j, coefficients are zeroed for all layers with scale factors unequal to a_j. The new layers are then used to reconstruct a filtered profile. Using this approach, the mean elevation of all the layers are equal to the mean elevation of the elevation profile before decomposition.

To reconstruct the elevation profile, all the decomposed layers can be summed, but this introduces an approximation error as shown in Eq. 8. The error layer was considered as a separate layer to be used in further analysis and define its impact in the simulation results.

$$f(x) = \sum_{j=1}^{N} f_R(a_j, x) + error(x) + (N-1)\overline{f(x)} \tag{8}$$

where $f_R(a_j,x)$ is the inverted detail layer with scale factor a_j; $error(x)$ is the approximation error layer; N is the number of the detail layers of a profile; and $\overline{f(x)}$ is the mean elevation of the original profile.

Quarter-Car Filter

Elevation profiles and their corresponding decomposition layers were filtered using a quarter-car (QC) model. This mathematical model simulates a tire with unsprung mass M_u and a spring coefficient K_u, connected in series with a Kelvin–Voigt element supporting a sprung mass M_s (Figure 29).

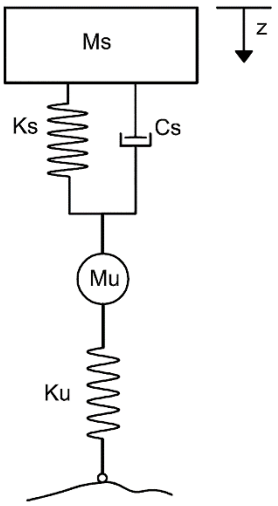

Figure 29. Quarter-car model schematic.

QC model is described in ASTM E 1926-98 to calculate IRI, which is defined as the accumulated suspension stroke divided by the traveled distance, or the absolute average suspension rate of a filtered elevation profile, QC filter is a band pass filter that attenuates certain frequencies and amplifies others (Sayers and Karamihas 1996). The simulation is based on solving a first order differential equation (Eq. 9).

$$\dot{X} = AX + B h_{ps} \tag{9}$$

where;

$$X = \begin{bmatrix} z_S & \dot{z}_S & z_u & \dot{z}_u \end{bmatrix}^T$$

$$A = \begin{bmatrix} 0 & 1 & 0 & 0 \\ -k_2 & -c & k_2 & c \\ 0 & 0 & 0 & 1 \\ \frac{k_2}{\mu} & \frac{c}{\mu} & -\frac{(k_1 + k_2)}{\mu} & -\frac{c}{\mu} \end{bmatrix}$$

$$B = \begin{bmatrix} 0 & 0 & 0 & k_1/\mu \end{bmatrix}^T$$

and h_{ps} is the elevation of the profile after applying the moving average smoother; z_S and z_u are the elevations of sprung and unsprung masses; $\dot{z}_S$ and $\dot{z}_u$ are elevation time derivatives of sprung and unsprung masses; k_1 is the tire spring coefficient divided by the sprung mass, k_2 is the suspension spring coefficient divided by the sprung mass, c is the suspension damping rate divided by the sprung mass, and μ is the ratio of unsprung to sprung mass.

To calculate the suspension rate (SR) values at each point, the elevation profile is first smoothed with a moving average filter that has a base length of 250 mm, then numerical simulation generates an SR profile. This simulation was performed on each layer of detail along with the original elevation profile. Based on the linear superposition principle, the sum of simulated layers equals the simulated elevation profile.

A summary index of the simulated layers is needed to determine the layers that contribute significantly to the SR profile. One of the common summative indices in wavelet analysis is the relative wavelet energy (P_j) of each layer (Eq. 10), where relative energy represents the

l^2-norm (magnitude) squared of the wavelet coefficients in a layer divided by the sum of l^2-norm squared for all layers. However the variance of inverted layers of details was used as a summary index because it can be used in other statistical tests (e.g. ANOVA).

$$P_j = \frac{E_j}{\sum_{i=1}^{N} E_i} \tag{10}$$

where

$$E_j = \sum_{b=-L/2}^{L/2} \left| W_f\left(a_j, b\right) \right|^2$$

and N is the number of detail layers and L is the length of the profile. The amplification and attenuation behavior of the QC filter on layers at different scale factors is analyzed by constructing gain graphs, where the gain value is defined as the ratio of the SR layer variance to the elevation layer variance.

Results and Discussion

Variance as a Summary Index

First to validate the use of variance as a summary index, the thirty elevation profiles were filtered using the QC filter algorithm. IRIs were calculated as the average of the absolute values in the SR profile, the results matched those results obtained from the LTPP database (2014). Figure 30(a) shows a strong correlation ($R^2 = 0.995$) between the natural logarithms of IRI and SR variance of the filtered elevation profiles. Log transformation was applied because the suspension variance values have a growing spread as IRI increase. The variance of individual elevation profiles was plotted against IRI values (Figure 30(b)) to show that the correlation between the natural logarithm of IRI and its elevation profile variance is not as

strong as the correlation between the natural logarithm of IRI and its suspension rate variance. This is because not all features in the elevation profiles induce suspension motion (Papagiannakis et al. 2007).

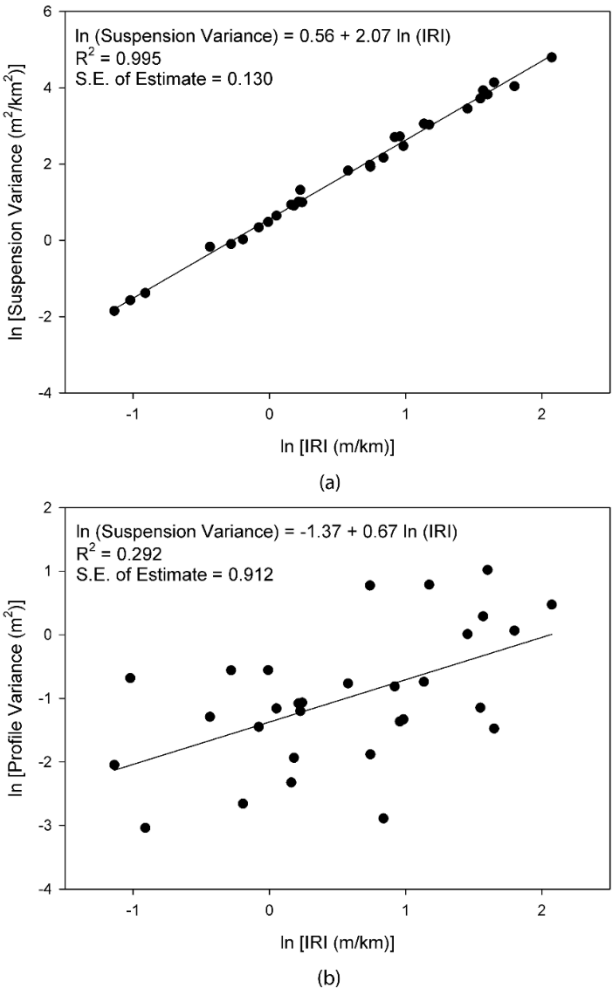

Figure 30. Profile variance vs. IRI for (a) suspension rate profiles and (b) elevation profiles.

Two sections, 124138 which is a jointed PCC section and 906420 which is an AC section, were studied closely because the PCC section has a lower IRI value compared to the AC section, yet the PCC section has a higher variance. The SR profiles of both sections are presented in Figure 31. In this case, the PCC profile has more extreme values compared to

the ACC profile. This suggests that variance might hold information about the overall roughness and the magnitude of extreme values in the SR profile, which indicates localized features.

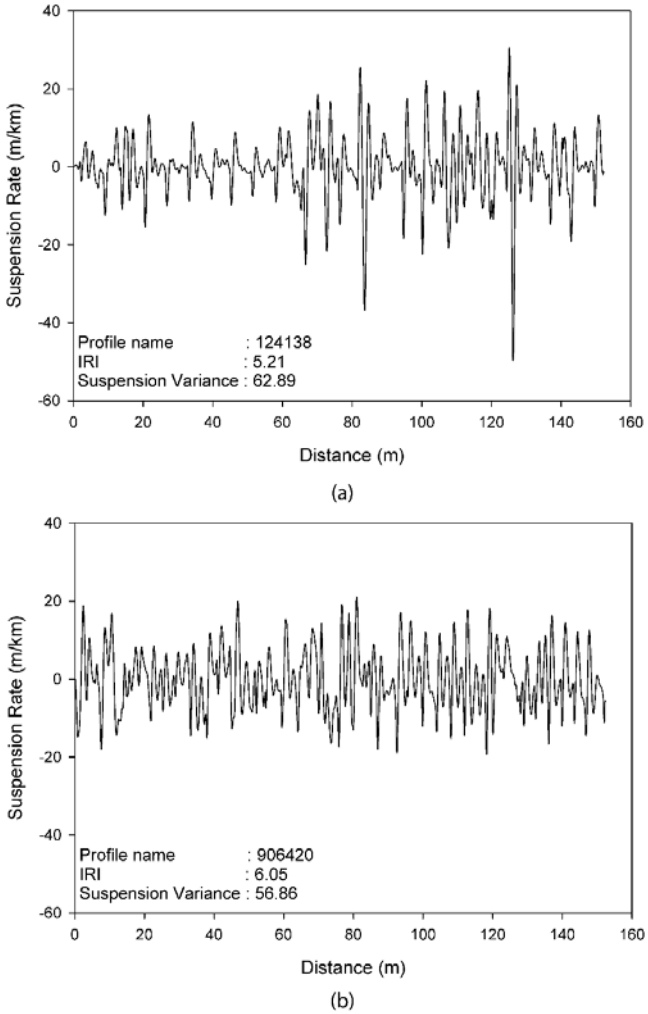

Figure 31. Suspension rate profile for (a) PCC section (124138) and (b) AC section (906420).

Statistical Analysis of AC and PCC Profiles

To compare the roughness of the AC and PCC sections, hypothesis tests (Welch ANOVA) were performed to investigate if the mean value of IRI or SR profile variance were

different for AC and PCC at significance level $\alpha = 0.05$. IRI values do not follow a normal distribution and thus the tests were performed on the natural logarithm of IRI values that asymptotically follow a normal distribution, normal distribution of the test statistic is required for hypothesis testing. Table 7 shows that there is not sufficient evidence to reject the null hypothesis (H_0) that the summary indices are different for AC and PCC sections.

Table 7. Welch's ANOVA results for summary indices.

Hypothesis	Mean summary index	F Ratio	P-Value
H_0: $\mu_{ln[IRI,AC]} = \mu_{ln[IRI,PCC]}$ H_a: $\mu_{ln[IRI,AC]} \neq \mu_{ln[IRI,PCC]}$	$IRI_{AC} = 2.39$ $IRI_{PCC} = 2.47$	0.03	0.86
H_0: $\mu_{SR\ Variance,\ AC} = \mu_{SR\ Variance,\ PCC}$ H_a: $\mu_{SR\ Variance,\ AC} \neq \mu_{SR\ Variance,\ PCC}$	$SR\text{-}Variance_{AC} = 16.51$ $SR\text{-}Variance_{PCC} = 20.14$	0.12	0.73

All points in the elevation and SR profiles and layers of details were pooled in two distribution families one for AC sections and one for PCC sections. Hypothesis tests (Levene's test) were performed to investigate if the distribution variance of the layers or the elevation or SR profiles are different for AC and PCC sections, the null and alternative hypotheses are described in Eq. 11.

$$\begin{aligned} H_0 &: \sigma^2_{Elevation\_AC} = \sigma^2_{Elevation\_PCC} \\ H_a &: \sigma^2_{Elevation\_AC} \neq \sigma^2_{Elevation\_PCC} \end{aligned} \quad \text{or} \quad \begin{aligned} H_0 &: \sigma^2_{Suspension\_AC} = \sigma^2_{Suspension\_PCC} \\ H_a &: \sigma^2_{Suspension\_AC} \neq \sigma^2_{Suspension\_PCC} \end{aligned} \tag{11}$$

From Table 8 it can be seen that the null hypothesis is rejected for all elevation distributions and that AC sections have higher distribution variance compared to PCC except for elevation layers corresponding to scales 0.07–0.38, 2.06, and 5.67. Also it can be observed that for the SR distributions there is not enough evidence to reject the null hypothesis for layers corresponding to scales 0.05, 0.07, and 2.06, and that AC sections have higher variance compared to PCC for layers corresponding to scales 0.27, 0.38, and 5.67.

Table 8. Levene's test results for elevation and suspension rate distribution variance.

Scale, a	Elevation distribution variance (cm^2)		P-value	Suspension rate distribution variance (cm^2)		P-value
	AC	PCC		AC	PCC	
0.05	1.70E-05	1.63E-05	<0.01	7.82E-05	7.09E-05	0.96
0.07	5.17E-05	5.84E-05	<0.01	1.23E-04	1.12E-04	0.19
0.10	9.53E-05	1.01E-04	<0.01	1.15E-04	1.09E-04	<0.01
0.14	1.27E-04	1.43E-04	<0.01	1.98E-04	1.87E-04	<0.01
0.19	1.57E-04	1.99E-04	<0.01	2.28E-04	1.78E-04	<0.01
0.27	2.26E-04	2.70E-04	<0.01	5.17E-04	5.53E-04	<0.01
0.38	3.35E-04	3.72E-04	<0.01	6.29E-03	6.34E-03	<0.01
0.53	4.97E-04	4.77E-04	<0.01	2.75E-02	2.45E-02	<0.01
0.75	8.66E-04	5.16E-04	<0.01	1.21E-01	7.17E-02	<0.01
1.05	9.44E-04	6.38E-04	<0.01	3.62E-01	2.59E-01	<0.01
1.47	1.09E-03	9.77E-04	<0.01	1.36E+00	1.22E+00	<0.01
2.06	1.62E-03	1.69E-03	<0.01	2.88E+00	3.12E+00	0.46
2.88	2.51E-03	2.19E-03	<0.01	2.15E+00	1.87E+00	<0.01
4.04	2.77E-03	2.63E-03	<0.01	8.95E-01	8.46E-01	<0.01
5.67	3.01E-03	3.81E-03	<0.01	4.33E-01	5.24E-01	<0.01
7.95	5.64E-03	5.02E-03	<0.01	4.23E-01	3.98E-01	<0.01
11.14	1.03E-02	4.59E-03	<0.01	5.07E-01	2.32E-01	<0.01
15.62	1.58E-02	9.63E-03	<0.01	4.35E-01	2.64E-01	<0.01
21.90	2.70E-02	1.81E-02	<0.01	1.90E-01	1.15E-01	<0.01
30.71	3.60E-02	1.92E-02	<0.01	1.82E-02	1.26E-02	<0.01
43.05	8.46E-02	2.44E-02	<0.01	5.71E-03	2.66E-03	<0.01
60.36	8.40E-02	1.39E-02	<0.01	7.49E-04	1.27E-04	<0.01
84.63	7.88E-02	1.34E-02	<0.01	3.09E-04	5.45E-05	<0.01
118.65	3.40E-02	8.83E-03	<0.01	8.37E-06	1.61E-06	<0.01
166.35	5.62E-02	1.45E-02	<0.01	1.39E-05	2.63E-06	<0.01
233.22	2.54E-07	6.44E-08	<0.01	6.32E-11	1.17E-11	<0.01
Full profile	9.48E-01	2.86E-01	<0.01	1.65E+01	1.47E+01	<0.01

These statistical tests indicate that although the AC and PCC pavements in this study had similar roughness indices, the SR variance in the AC pavements is larger. This finding is consistent with earlier work (Darter et al. 1973; Kher and Darter 1973) that compared initial AC and PCC serviceability indexes, where AC demonstrated a larger variance compared to PCC.

CWT Contour Plots

The thirty elevation profiles were decomposed into 26 layers (except for profile 06B441) using continuous Morlet wavelet, and the QC filter was applied to each elevation layer to obtain SR layers. In the decomposed elevation profiles (left columns in cm) and filtered SR layers (right columns in m/km) shown for three AC (Figure 32) and three PCC (Figure 33) where X axes are distance and Y axes represent scale factors from zero to 70 for elevation and zero to 30 for SR layers. From any point along the X axis, the color scale along the Y axis indicates the wavelet content (i.e., analogous to frequency content in Fourier terminology) that corresponds to roughness features. As might be expected, at higher scales the AC sections exhibit higher variability than the PCC sections; features with longer wavelength appear in AC sections as compared to PCC sections, where features have shorter wavelengths.

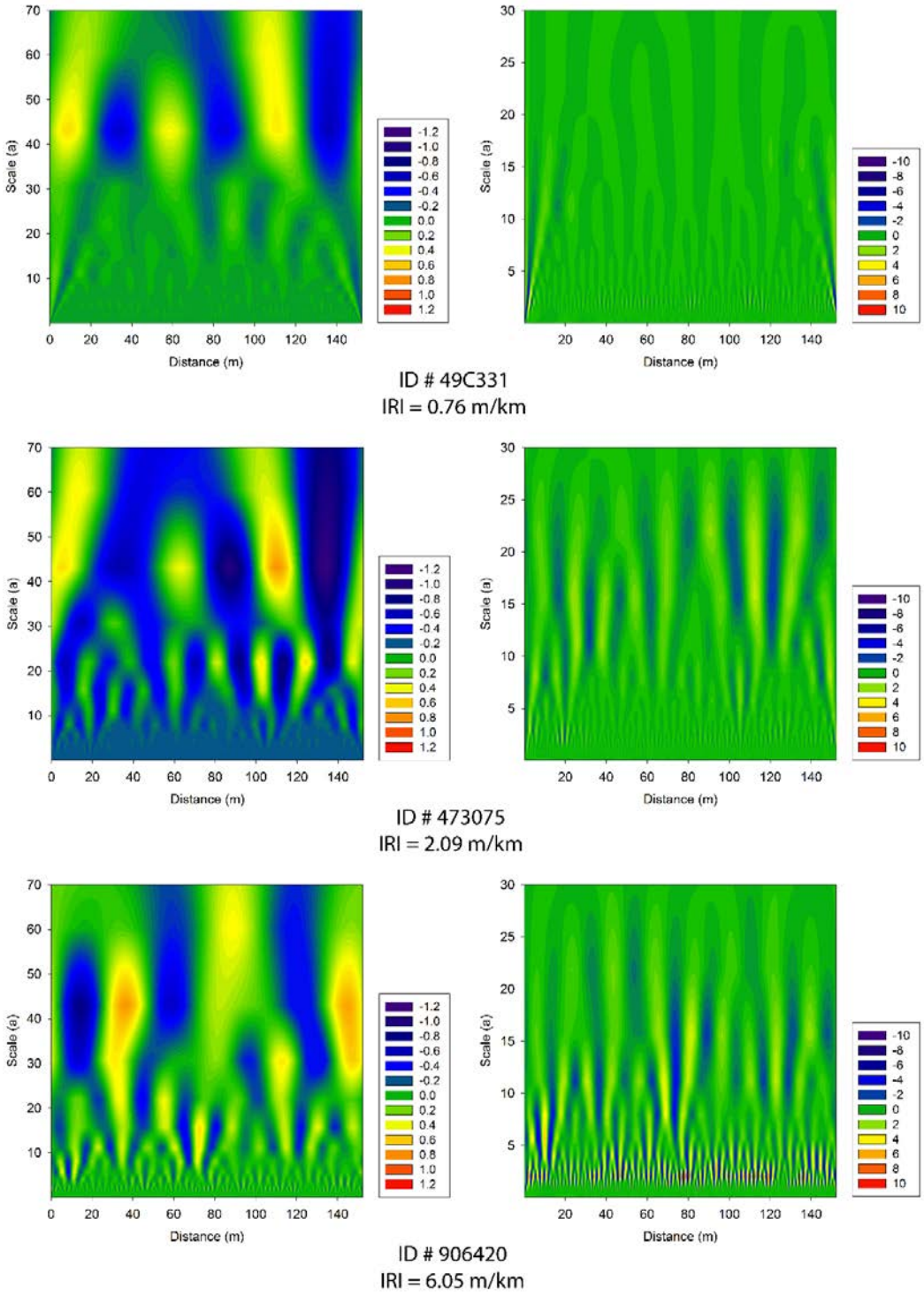

Figure 32. Wavelet decomposition amplitude contours for elevation (left) and SR profiles (right) in scale-distance domain for three AC sections with low, medium, or high roughness.

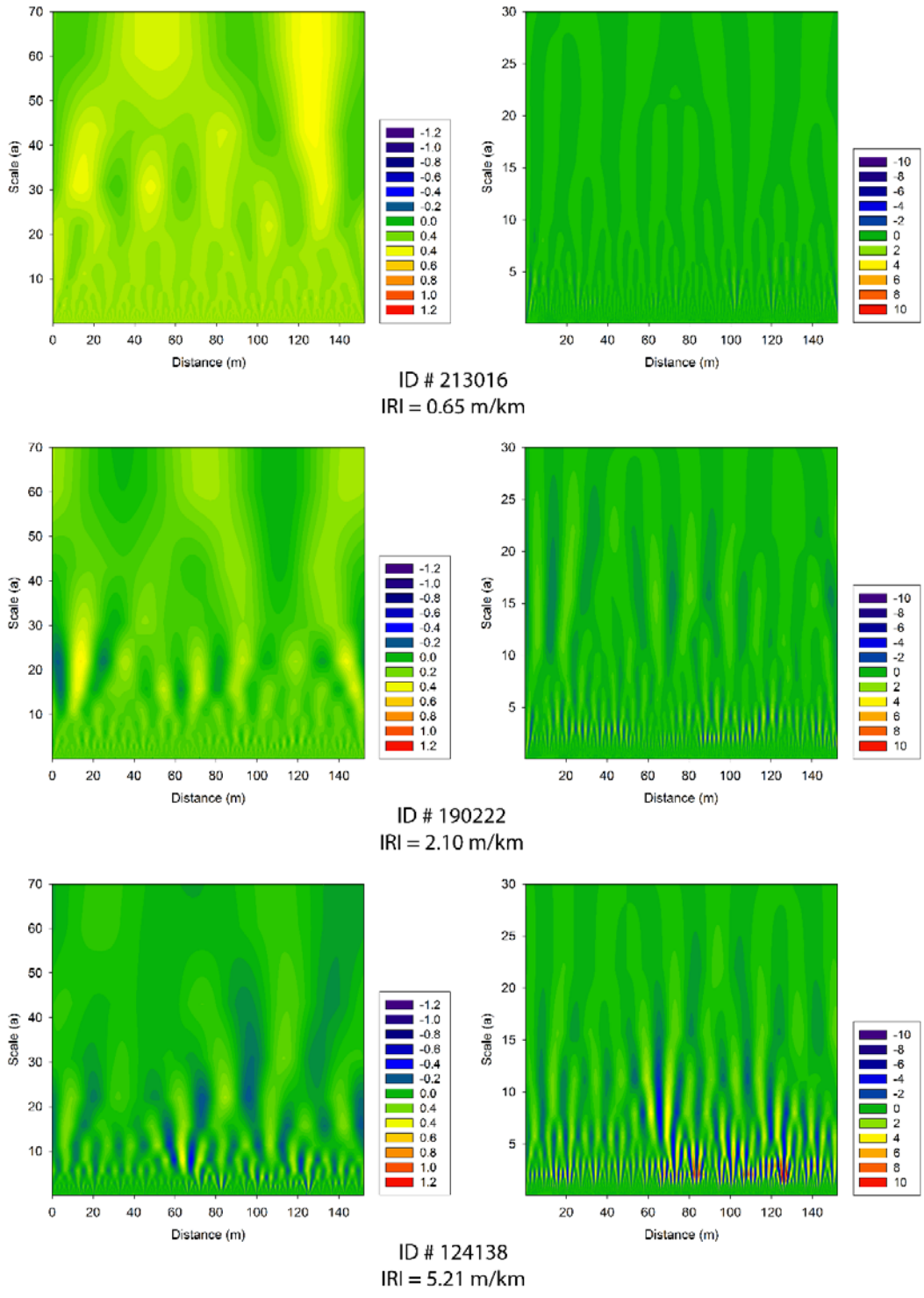

Figure 33. Wavelet decomposition amplitude contours for elevation profiles (left) and SR profiles (right) in scale-distance domain for three PCC sections with low, medium, or high roughness.

Significant Layers of Detail

To identify the layers with the highest SR magnitudes, the variance of each layer for both elevation profiles and SR profiles was calculated, and the percentage of information contained in a layer is defined as the ratio of its variance to the sum of all other variances including the error profile, and referred to as % variance.

Figure 34(a) shows two curves representing the average % variance of all elevation layers for AC and PCC sections. In general, both curves have dominant peaks around the scale factor of 43 (pseudo-frequency 0.019 cycle/m) and at the scale factor 165 (pseudo-frequency 0.005 cycle/m). It can be seen also that PCC sections had higher average variance up to a scale factor 31 (pseudo-frequency 0.027 cycle/m), and AC sections had higher average variance at higher scale factors.

Figure 34(b) shows two curves representing the average % variance of SR layers for AC and PCC sections. The figure shows that both types of pavement exhibit similar trends, and that the curves have only two peaks occurring at the scale factors 2.06 and 15.62 (pseudo-frequencies 0.395 and 0.052 cycle/m respectively). These peaks occur at pseudo-frequencies approximately equal to the frequencies corresponding to the peaks of the IRI filter (0.42 and 0.065 cycle/m) where the first peak corresponds to the tire hop mode and the second to the body bounce mode of vibration. On average 98% of the variance in the SR profile is attributed to the variance in the layers having scale factors between 0.75 and 21.90 (0.04–1.09 cycle/m).

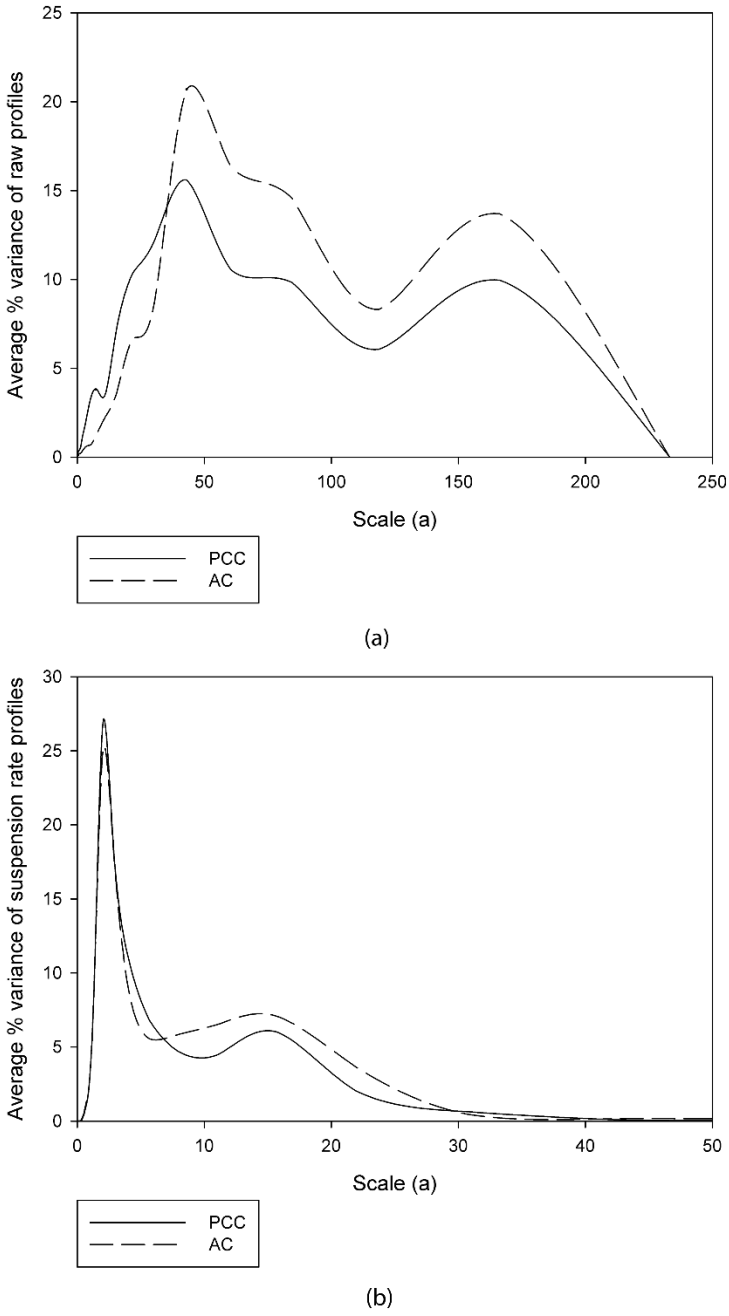

Figure 34. Average % variance of (a) elevation profiles and (b) suspension rate profiles at different scales for AC and PCC sections.

The wavelet analysis can be utilized as a filtering technique, where only the significant layers can be superimposed to result in a filtered profile. The derivative of the filtered profile

can be used to identify the location of rough features in a road. Figure 35 shows the derivatives for the elevation profile (a), the wavelet filtered profile (b), and the SR profile from QC simulations (c) for section 06B441. The wavelet filtered elevation profile was composed of 10 layers out of the 23 elevation layers (i.e., from scale factor 1.05 to 21.90). The cumulative % variance of the elevation layers from scale factor 1.05 to 21.90 is 53%, however cumulative % variance of these layers is 99%. It is clear the derivative of the wavelet filtered profile is very similar to the SR profile, unlike the derivative of the original profile, where it is very noisy and has several high peaks that are attenuated in the SR profile.

An important application of wavelet filter as described herein is the ability to analyze relatively short pavement segments, relative to using the traditional finite difference QC simulation. Using the Morlet wavelet, 11 m long profiles (equivalent to 0.5 sec for a vehicle traveling at 80 km/hr) can be decomposed to layers with a scale factor up to 21.90. The described approach can analyze down to 4 m without a major loss in accuracy. The advantage of assessing short segments of pavement is that it support more accurate and near real-time analysis that can be used in control system of automated paving machines (Rasmussen et al. 2013).

In theory this can be achieved by segmenting the analyzed section into short profiles, thus although CWT is computationally expensive for long profiles, it is not as expensive for short profiles, because less layers are required to cover the frequency range. After segmentation, analysis can be performed and summarized using CWT coefficients to compress the data, this compressed information can be efficiently transferred and utilized to determine the location and severity of rough features.

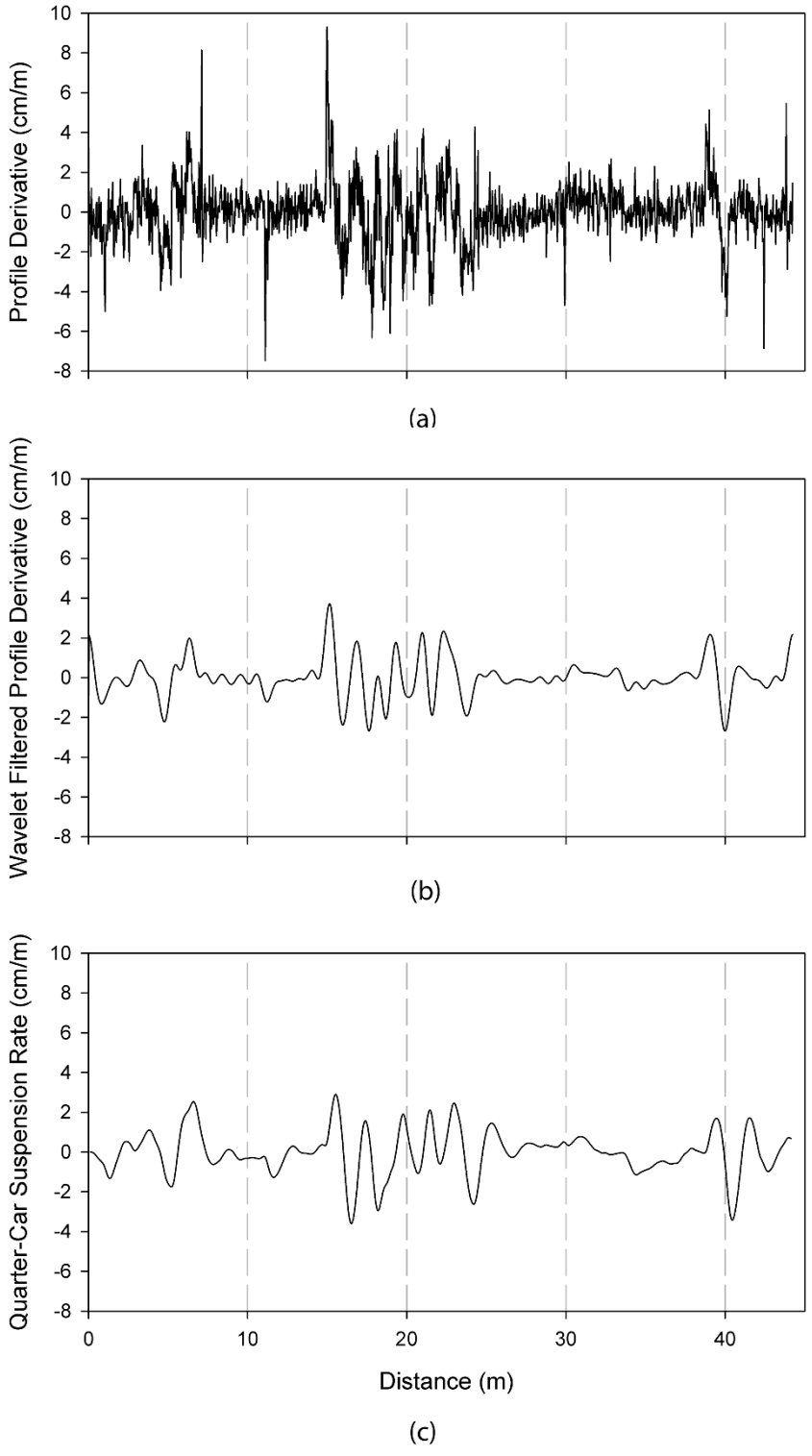

Figure 35. Section 06B441: (a) elevation profile derivative, (b) wavelet filtered elevation profile derivative, and (c) suspension rate profile from quarter-car simulations.

Conclusions

Thirty road profiles with a wide range of surface roughness and two pavement types (i.e., AC and PCC) were decomposed using CWT into different layers of details corresponding to distinct frequency band components. These layers were then filtered using a QC model to identify the most significant layers that affect that SR profile. This type of analysis has the advantage of identifying localized features in the spatial domain and at the target frequency bands that affect the ride quality of a road. However the study is limited to CWT and should be expanded to include and compare the analysis approach using DWT. Also future work should investigate the computational efficiency and provide a framework to use such computation in real time. The key conclusions from this study are:

- For the percent variance of SR profiles, only two narrow peaks appear at scale factors 2.06 and 15.62 (pseudo-frequencies 0.395 and 0.052 cycle/m respectively), and on average 98% of the variance in the SR profiles is attributed to the variance in the layers having scale factors between 0.75 and 21.90 (0.75–21.90 cycle/m).
- Although there is a strong correlation between the variance of SR profiles and IRI values, the variance is more sensitive to outliers, as a parameter, variance holds information about both the overall roughness and the range of the variance of SR profiles indicates localized features.
- Because high amplitude features in derivatives of elevation profiles might attenuate after filtering, not all features in elevation profiles affect ride quality.
- The SR profiles of the AC sections are more variable than the SR profiles of the PCC sections even though the AC and PCC sections have similar average IRI values.

- CWT proved to be a valuable tool for examining the details of SR profiles with high resolution in both frequency and the spatial domains and for decomposing relatively short segments of pavement.

Acknowledgements

The authors wish to thank Dr. Christianna White for providing review comments.

Work Cited in Chapter 4

Al-Omari, B., and Darter, M. I. (1994). "Relationships between international roughness index and present serviceability rating." *Transportation Research Record*(1435).

Aslaksen, E. W., and Klauder, J. R. (1968). "Unitary representations of the affine group." *Journal of Mathematical Physics*, 9(2), 206-211.

Boggess, A. (2009). *A First Course in Wavelets with Fourier Analysis*, Hoboken John Wiley & Sons, Hoboken, N.J.

Bogsjö, K., and Rychlik, I. (2009). "Vehicle fatigue damage caused by road irregularities." *Fatigue & Fracture of Engineering Materials & Structures*, 32(5), 391-402.

Bosché, F., and Biotteau, B. (2015). "Terrestrial laser scanning and continuous wavelet transform for controlling surface flatness in construction – A first investigation." *Advanced Engineering Informatics*.

Bosché, F., and Guenet, E. (2014). "Automating surface flatness control using terrestrial laser scanning and building information models." *Automation in Construction*, 44, 212-226.

Calderón, A. (1964). "Intermediate spaces and interpolation, the complex method." *Studia Mathematica*, 24(2), 113-190.

Cheng, H.-D., and Miyojim, M. (1998). "Automatic pavement distress detection system." *Information Sciences*, 108(1), 219-240.

Cheng, H., Chen, J., Glazier, C., and Hu, Y. (1999). "Novel approach to pavement cracking detection based on fuzzy set theory." *Journal of Computing in Civil Engineering*, 13(4), 270-280.

Chootinan, P., Chen, A., Horrocks, M. R., and Bolling, D. (2006). "A multi-year pavement maintenance program using a stochastic simulation-based genetic algorithm approach." *Transportation Research Part A: Policy and Practice*, 40(9), 725-743.

Daubechies, I. (1992). *Ten lectures on wavelets*, Philadelphia, PA : Society for Industrial and Applied Mathematics, Philadelphia, PA.

Federal Highway Administration (2014). "LTPP InfoPave." Long Term Pavement Performance.

Gao, H., and Zhang, X. (2013). "A Markov-based road maintenance optimization model considering user costs." *Computer-Aided Civil and Infrastructure Engineering*, 28(6), 451-464.

Gavilán, M., Balcones, D., Marcos, O., Llorca, D. F., Sotelo, M. A., Parra, I., Ocaña, M., Aliseda, P., Yarza, P., and Amírola, A. (2011). "Adaptive road crack detection system by pavement classification." *Sensors*, 11(10), 9628-9657.

Georgopoulos, A., Loizos, A., and Flouda, A. (1995). "Digital image processing as a tool for pavement distress evaluation." *ISPRS Journal of Photogrammetry and Remote Sensing*, 50(1), 23-33.

Herabat, P., and Songchitruksa, P. (2003). "A decision support system for flexible pavement treatment selection." *Computer-Aided Civil and Infrastructure Engineering*, 18(2), 147-160.

Hesami, R., and McManus, K. J. "Signal processing approach to road roughness analysis and measurement." *Proc., TENCON 2009-2009 IEEE Region 10 Conference*, IEEE, 1-6.

Kilpeläinen, P., Jaakkola, M., and Alanaatu, P. (2011). "Development of a control system for a multipurpose road repairing machine." *Automation in Construction*, 20(6), 662-668.

Lamptey, G., Labi, S., and Li, Z. (2008). "Decision support for optimal scheduling of highway pavement preventive maintenance within resurfacing cycle." *Decision Support Systems*, 46(1), 376-387.

Lin, J.-D., Yau, J.-T., and Hsiao, L.-H. "Correlation analysis between international roughness index (IRI) and pavement distress by neural network." *Proc., 82nd annual meeting in January, 2003*.

Mahler, D. S., Kharoufa, Z. B., Wong, E. K., and Shaw, L. G. (1991). "Pavement distress analysis using image processing techniques." *Computer-Aided Civil and Infrastructure Engineering*, 6(1), 1-14.

MathWorks. 2013. MATLAB and Wavelet Toolbox 2013bThe MathWorks, Inc., Natick, Massachusetts, United States.

Morlet, J. (1983). "Sampling theory and wave propagation." *Issues in Acoustic Signal—Image Processing and Recognition*, Springer, 233-261.

Nejad, F. M., and Zakeri, H. (2011). "An expert system based on wavelet transform and radon neural network for pavement distress classification." *Expert Systems with Applications*, 38(6), 7088-7101.

Nejad, F. M., and Zakeri, H. (2011). "An optimum feature extraction method based on Wavelet–Radon Transform and Dynamic Neural Network for pavement distress classification." *Expert Systems with Applications*, 38(8), 9442-9460.

Nitsche, P., Stütz, R., Kammer, M., and Maurer, P. (2014). "Comparison of machine learning methods for evaluating pavement roughness based on vehicle response." *Journal of Computing in Civil Engineering*, 28(4), 04014015.

Oijer, F., and Edlund, S. (2004). "Identification of transient road obstacle distributions and their impact on vehicle durability and driver comfort." *Vehicle System Dynamics*, 41, 744-753.

Ouyang, Y., and Madanat, S. (2004). "Optimal scheduling of rehabilitation activities for multiple pavement facilities: exact and approximate solutions." *Transportation Research Part A: Policy and Practice*, 38(5), 347-365.

Papagiannakis, A. T., Zelelew, H. M., and Muhunthan, B. (2007). "Wavelet analysis of energy content in pavement roughness and truck dynamic axle loads." *Transportation Research Record: Journal of the Transportation Research Board*, 2005(1), 153-159.

Papagiannakis, A. T., Zelelew, H. M., and Muhunthan, B. (2007). "A wavelet interpretation of vehicle-pavement interaction." *International Journal of Pavement Engineering*, 8(3), 245-252.

Pinsky, M. A. (2002). *Introduction to Fourier analysis and wavelets*, Brooks/Cole Pacific Grove.

Radopoulou, S. C., and Brilakis, I. (2015). "Patch detection for pavement assessment." *Automation in Construction*, 53(0), 95-104.

Rasmussen, R. O., Torres, H. N., Sohaney, R. C., Karamihas, S. M., and Fick, G. (2013). "Real-time smoothness measurements on Portland cement concrete pavements during construction." Transportation Research Board, SHRP 2 Report S2-R06E-RR-1, 143p.

Sayers, M. W., and Karamihas, S. M. (1996). "Interpretation of road roughness profile data." University of Michigan Transportation Research Institute.

Sen, R., Hassan, R. A., and Evans, R. P. (2012). "Wavelet-based detection of roughness progression in wavebands for highways in Victoria, Australia." *Transportation Research Record: Journal of the Transportation Research Board*, 2304(1), 17-27.

Shokouhi, P., Gucunski, N., Maher, A., and Zaghloul, S. M. (2005). "Wavelet-based multiresolution analysis of pavement profiles as a diagnostic tool." *Transportation Research Record: Journal of the Transportation Research Board*, 1940(1), 79-88.

Stein, E. M., and Shakarchi, R. (2011). *Fourier analysis: an introduction*, Princeton University Press.

Tomiyama, K., Kawamura, A., and Ohiro, T. "Lifting wavelet transform for distress identification using response type profilers." *Proc., Transportation Research Board 93rd Annual Meeting*.

Tsai, Y., Jiang, C., and Huang, Y. (2012). "Multiscale crack fundamental element model for real-world pavement crack classification." *Journal of Computing in Civil Engineering*, 28(4), 04014012.

Ueckermann, A., and Steinauer, B. (2008). "The weighted longitudinal profile." *Road Materials and Pavement Design*, 9(2), 135-157.

Wei, L., Fwa, T., and Zhe, Z. (2005). "Wavelet analysis and interpretation of road roughness." *Journal of transportation engineering*, 131(2), 120-130.

Zalama, E., Gómez-García-Bermejo, J., Medina, R., and Llamas, J. (2014). "Road crack detection using visual features extracted by Gabor filters." *Computer-Aided Civil and Infrastructure Engineering*, 29(5), 342-358.

CHAPTER 5. WAVELET FILTERS DESIGN FOR PAVEMENT ROUGHNESS ANALYSIS

A paper submitted to *computer aided civil and infrastructure engineering*

Ahmad Alhasan[1,2,3], David J. White[4], Kris De Brabanter [5]

Abstract

Pavement roughness can be quantified by examining built-in or deterioration features that affect surface conditions or by analyzing vehicle suspension responses (SR) to surface geometry. SR is normally estimated by quarter-car (QC) filtering in the frequency domain or by simulating the QC model in the spatial domain using a finite difference (FD) algorithm. However, emerging technologies in automated machine guidance require a systematic approach to analyze short road segments in both domains simultaneously to quantify overall and localized (i.e., spatial) roughness. In this study, multiple wavelet bases were modified in the frequency domain to define 116 new filters in the spatial domain that were used to analyze 30 road profiles. Performance of these filters in terms of assessing different lengths and accurately quantifying localized features was compared to other analysis techniques. Filters developed using db21 and morl0 outperformed other approaches in terms of consistency of filtering output at short profile lengths.

[1] Graduate research assistant, Department of Civil, Construction, and Environmental Engineering, Iowa State University.
[2] Primary researcher and author.
[3] Author for correspondence.
[4] Richard L. Handy Professor of Civil Engineering, Department of Civil, Construction, and Environmental Engineering, Iowa State University.
[5] Assistant Professor, Department of Statistics, Department of Computer Science, Iowa State University.

Keyword: Pavements, Surface roughness, Wavelet analysis, Fourier analysis, Vibration, Dynamic analysis, Mathematical models, Data analysis.

Pavement surface roughness is a key parameter in evaluating and predicting pavement performance during its life cycle (Bianchini 2012; Roberts and Attoh-Okine 1998) and pavement quality during construction (Mosa et al. 2013). Roughness increases vehicle operation and travel delay costs (Gao and Zhang 2013; Ouyang and Madanat 2004); reduces vehicle durability (Bogsjö and Rychlik 2009; Oijer and Edlund 2004); and reduces ride quality and structural performance (Al-Omari and Darter 1994).

Roughness can be quantified by examining built in or deteriorated features for severity and extent (e.g., crack and pothole width and depth measurements) or by analyzing vehicle suspension responses (SR) to road geometry. SR is typically summarized using an index value such as the International Roughness Index (IRI), the most widely used summative index that characterizes overall roughness. IRI is defined as the average of absolute rectified slopes (i.e., SR) of the pavement profile. Most IRI calculations are based on one of two approaches. One way is to calculate an SR profile using fast Fourier transform (FFT) to transform a road elevation profile to the frequency domain; applying the quarter-car (QC) filter to the transformed profile (Liu and Herman 1998; Liu and Herman 1999); and inverting the filtered profile to the spatial domain. Another way is to implement a state space solution that solves the differential equations that describe the QC model in an FD algorithm (Sayers and Karamihas 1996). However, these IRI calculations do not provide sufficient detail to identify localized features (Herabat and Songchitruksa 2003; Nitsche et al. 2014; Ueckermann and Steinauer 2008).

Quantifying localized features is crucial because they affect human comfort and cause vehicle fatigue damage (Bogsjö and Rychlik 2009; Oijer and Edlund 2004; Steinwolf et al. 2002). Sayers (1990) suggested a continuous roughness profile calculated by applying a moving average on SR profiles to detect localized features, and Swan and Karamihas (2003) demonstrated the use of continuous roughness profiles to detect localized features for smoothness specifications. Although these approaches emphasize the importance of detecting localized features, they are based on analyzing long sections and then retrieving localized features. However, emerging technologies in road construction, such as automated machine guidance (AMG), light detection and ranging (LiDAR), and 3D modeling, require a systematic approach that quantifies the roughness of short profiles (< 7.62 m) continually and in real time so corrective actions can be taken during construction without having to wait until a full section has been profiled (Perera and Kohn 2002; Rasmussen et al. 2013).

However, the QC filter in the frequency domain can suffer time-frequency uncertainty where the accuracy of the analysis decreases as the profile length decreases (Pinsky 2002; Stein and Shakarchi 2011). The state space solution is also suspected to suffer from boundary problems because the solution has a memory so the starting point of the analysis affects the results (Sayers 1990).

Wavelet analysis techniques were developed independently in different fields (e.g., pure mathematics, physics, and engineering) to overcome time-frequency uncertainty problems (Aslaksen and Klauder 1968; Boggess 2009; Calderón 1964; Daubechies 1992; Morlet 1983). Signal processing techniques, such as power spectral density (PSD) estimates and discrete wavelet transform (DWT), have been used to quantify pavement roughness. DWT outperformed PSD analysis especially in detecting localized defects such as cracks and

potholes (Hesami and McManus 2009; Shokouhi et al. 2005). Papagiannakis et al. (2007) used DWT to analyze suspension responses obtained from a 5-axle semi-trailer truck. Dynamic loads correlated with wavelets of pseudo-frequencies between 0.65 and 3.76 cycle/m. Wei et al. (2005) correlated IRI to the wave energy at different wavelet frequency bands. Tomiyama et al. (2014) used lifting wavelet transform to detect pavement distresses from a response type profile.

Other statistical and signal processing techniques extract and classify pavement defects based on geometry and not ride quality (Mahler et al. 1991). Zalama et al. (2014) developed a statistical learning system that uses a Gabor filter to detect longitudinal and transverse cracks, and Gavilán et al. (2011) developed a fully automated distress classifier that uses textural properties as inputs to a linear support vector machine framework. Nejad and Zakeri (2011; 2011) demonstrated the advantages of using wavelet analysis results as inputs to neural network schemes in classifying pavement distresses.

However, to date there are no studies that explain the development of a new filter capable of decomposing and filtering road profiles in a single step to yield continuous SR profiles at a finite number of frequency bands. Further, there are no studies that compare the performance of the QC filter in the frequency domain, FD algorithm, continuous wavelet filters, and discrete wavelet filters in analyzing road profiles of different lengths.

In this paper, multiple wavelet bases including wavelets with explicit forms (i.e., continuous wavelets) and more complicated, iteratively constructed forms (i.e., discrete wavelets) were modified to define 116 new filters in the spatial domain. These filters were formulated by transforming the wavelet bases into the frequency domain and applying the QC filter to them. The new bases were inverted to the spatial domain to define quarter-car

wavelet (QC-wavelet) filters. These new filters were used to analyze 30 AC or PCC road profiles obtained from the Long Term Pavement Performance (LTPP) Database (2014) with a wide range of surface roughness. The results were compared at varying profile lengths with FD algorithm and QC filtering in the frequency domain. The advantages of QC-wavelet filters include analyzing short road segments with accuracy and providing high resolution in the frequency and spatial domains simultaneously. QC-wavelet filters also identify localized features with higher accuracy than the FD algorithm, and the QC-wavelet filters are expected to support data compression and allow physical inferences from compressed data.

Wavelet Analysis

Wavelet analysis was developed to overcome the time-frequency resolution issue in Fourier analysis where high resolution analysis cannot be achieved simultaneously in both frequency and time (spatial) domains (Boggess 2009; Daubechies 1992). As analogues to sinusoids in Fourier transform, wavelets are the building blocks (bases) from which a signal (profile) can be composed.

Depending on the analysis scheme, there are two main categories of wavelets: wavelets used for discrete wavelet transform (DWT) and wavelets used for continuous wavelet transform (CWT). Wavelets should satisfy a set of admissibility conditions (Boggess 2009) and come in families. For each family there is a wavelet function (mother wavelet) and a scaling function (father wavelet), but some continuous wavelet families do not include scaling functions and some wavelet forms can be used in both analysis schemes. In this study, DWT wavelet functions were constructed iteratively from the scaling function, but because CWT wavelet functions have explicit forms, they do not always require scaling functions to construct wavelet functions. For CWT and DWT, the wavelet transform projects

the profile onto wavelet bases with different scales (i.e., layers of details) that correspond to different frequency bands. This results in wavelet coefficients that describe correlations between the profiles and the wavelet functions. To retrieve the profile content at a frequency band, inverse wavelet transform is applied to the coefficients in that frequency band. This process resolves the space-frequency resolution issue and allows identification of features within known frequency contents.

Continuous Wavelet Transform

The CWT base is a smooth wave pulse (Figure 36) described by explicit equation either in the spatial or the frequency domain. The Fourier transform of a wavelet function (i.e., $\hat{\psi}(\xi)$) produces a narrow function in the frequency domain with a central pseudo frequency ξ_c that is the most dominant frequency component in a wavelet function and that corresponds to the frequency of the sinusoidal wave segment that best matches the wavelet. The scale factor *a* tunes (dilates) the dominant frequency of a wavelet function, which results in a new frequency referred to as pseudo-frequency ξ that is proportional to *1/a*. Figure 1 shows how a smaller scale factor corresponds to higher frequencies and a narrower wave function.

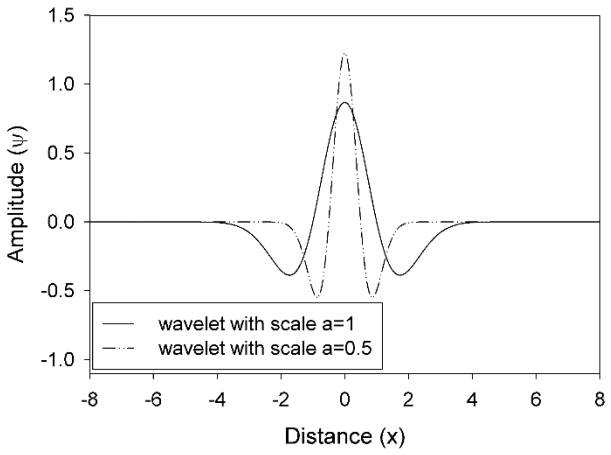

Figure 36. Mexican hat wavelet function with a scale factor a = 1 and a = 0.5.

A wavelet transform (W_f) is defined as the convolution of the wavelet function (ψ) at a scale factor *a* and a location (translation factor) *b* with the profile (*f*). Equation (1) represents the wavelet transform of a function in the inner product and in the integral notations, and Equation (2) defines the dilated wavelet function centered about the translation factor *b*.

$$W_f(a,b) = \left\langle \psi_{a,b} \middle| f \right\rangle = \int_{-\infty}^{+\infty} f(x)\overline{\psi}_{a,b}(x)dx \tag{1}$$

$$\psi_{a,b}(x) = \frac{1}{\sqrt{a}}\psi\left(\frac{x-b}{a}\right) \tag{2}$$

where $\overline{\psi}_{a,b}(x)$ is the complex conjugate of the wavelet function. The inverse wavelet transform that provides the form to retrieve the original un-decomposed profile is defined in Equation (3). However if a single layer of detail (frequency band) is of interest, the second integral over the scale factors can be eliminated and each layer is integrated separately.

$$f(x) = \frac{1}{C_\psi}\int_{-\infty}^{+\infty}\int_{-\infty}^{+\infty}|a|^{-1/2}\psi\left(\frac{x-b}{a}\right)W_f(a,b)\frac{dbda}{a^2} \tag{3}$$

where

$$C_\psi = 2\pi\int_{-\infty}^{+\infty}\frac{\left|\hat{\psi}(\xi)\right|^2}{|\xi|}d\xi$$

Discrete Wavelet Transform and Multiresolution Analysis

Unlike CWT, DWT bases are constructed iteratively and are not smooth functions with explicit forms and must satisfy a set of admissibility conditions (Boggess 2009). Wavelet families constitute a sequence of subspaces V_j in Lebesgue space $L^2(\mathbb{R})$, where V_j is a

subspace constructed from a linear combination of scaling functions ϕ as defined in Equation (4):

$$V_j = \sum_{b \in Z} A_{b,j} \phi\left(2^j x - b\right) \tag{4}$$

where $A_{b,j}$ is the amplitude of a scaling function at a level j that corresponds to a frequency band determined based on the wavelet family characteristic and a shifting factor b that determines the center of the function. Subsequently W_j is the subspace of a linear combination of wavelet functions ψ as defined in Equation (5):

$$W_j = \sum_{b \in Z} A_{b,j} \psi\left(2^j x - b\right) \tag{5}$$

Accordingly the wavelet function can be constructed as a linear combination of scaling functions as defined in Equation (6):

$$\psi_j(x) = \sum_b A_{b,j} \phi\left(2^j x - b\right) \tag{6}$$

W_j is the orthogonal complement of V_j in V_{j+1} as defined in Equation (7), which also shows that V_j is an element of V_{j+1}.

$$V_{j+1} = V_j \oplus W_j \tag{7}$$

where $\oplus$ is the orthogonal sum operator. If the collection of spaces satisfies the following five conditions, DWT is referred to as a multiresolution (Boggess 2009):

1. nested: $V_j \subset V_{j+1}$;
2. density: $\bigcup V_j$ is dense in $L^2(\mathbb{R})$;
3. separation: $\bigcap V_j = \{0\}$;

4. scaling: The function $f(x)$ belongs to V_j if and only if the function $f(2^{-j}x)$ belongs to V_0; and
5. orthonormal bases.

The nested condition can be deduced from Equation (7) that expresses the content in a layer at the level $j+1$ can be composed of two other layers, one projected onto the scaling function and the other onto the wavelet function at the level j. The density condition means that the whole space can be composed of the subspaces V_j. The separation condition means that the decomposed layers do not contain common features such that each decomposition contains a unique set of features. The scaling condition means that the scaling of a space will correspondingly affect the function contained in the space by a factor 2^j that corresponds to the down sampling of a profile when using pyramidal algorithms. The orthonormal condition ensures that the bases do not interfere and that the total energy of the decomposed layers will be equal to the energy of the original un-decomposed profile.

Analysis Approach

Road Profiles

Sixteen asphalt concrete (AC) and 14 Portland cement concrete (PCC) pavements with IRI values ranging from 0.32 m/km to 7.95 m/km were selected from the LTPP database without regard to the location or profiling date (Table 9). These profiles were analyzed in a previous study, but that analysis was limited to decomposing the road profiles and SR profiles produced by the FD algorithm using CWT (Alhasan et al. 2015).

Table 9. LTPP profile information.

State code	SHRP code	Pavement Type	IRI	State code	SHRP code	Pavement Type	IRI
49	A351	AC	3.23	90	6420	AC	1.78
49	C331	AC	0.76	06	B441	PCC	7.95
90	B340	AC	3.11	48	C430	PCC	2.68
01	0101	AC	0.82	49	E458	PCC	2.31
04	1062	AC	0.32	06	3005	PCC	4.71
06	8535	AC	0.93	12	4138	PCC	5.21
12	4137	AC	0.36	19	0222	PCC	2.10
25	1002	AC	4.28	19	3055	PCC	0.40
34	0502	AC	1.24	21	3016	PCC	0.65
47	3075	AC	2.09	40	0160	PCC	1.27
48	1065	AC	4.96	42	1613	PCC	1.18
51	0120	AC	1.05	42	1617	PCC	0.99
81	0503	AC	2.51	46	0661	PCC	1.20
85	1801	AC	4.80	49	7083	PCC	1.26
90	6420	AC	6.05	89	3015	PCC	2.61

Quarter-Car Wavelet Filter

A quarter-car (QC) model was used to evaluate the roughness of the profiles. This mathematical model simulates a tire with an unsprung mass M_u and a spring coefficient K_u, connected in series with a Kelvin–Voigt element supporting a sprung mass M_s (Figure 37).

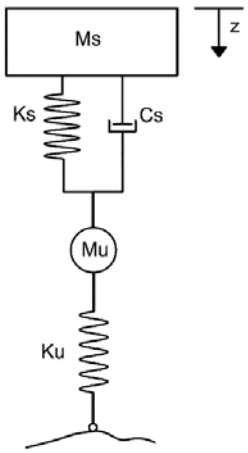

Figure 37. Quarter-car model schematic.

The QC model can be described as a band pass filter that attenuates certain frequencies and amplifies others (Sayers and Karamihas 1996). A filtered road profile is defined as an SR profile that consists of a string of rectified slope values. The average of absolute rectified slopes in an SR profile is the IRI value. Liu and Herman (1998) defined the QC band pass filter in the frequency domain as shown in Equation (9):

$$\hat{R}_0(\omega) = \alpha_0 \omega^2 \Big/ \left(1 + \alpha_1 \omega^2 + \alpha_2 \omega^4 + \alpha_3 \omega^6 + \alpha_4 \omega^8\right)^{1/2} \tag{9}$$

where

$$\alpha_0 = M_s / k_s$$

$$\alpha_1 = C_s{}^2 / k_s{}^2 - 2\left[M_s / k_s + (M_s + M_u)/k_t\right]$$

$$\alpha_2 = \left[M_s / k_s + (M_s + M_u)/k_t\right]^2 + 2\left(M_s M_u k_s - C_s{}^2 (M_s + M_u)\right) \Big/ k_s{}^2 k_t$$

$$\alpha_3 = C_s{}^2 (M_s + M_u)^2 \Big/ k_s{}^2 k_t{}^2 - 2 M_s M_u \left(k_s M_u + (k_s + k_t) M_s\right) \Big/ k_s{}^2 k_t{}^2$$

$$\alpha_4 = \left(M_s M_u / k_s k_t\right)^2$$

An elevation profile can be decomposed using CWT or DWT to obtain layers of details. Because the layers are separate and nested for DWT or approximately separate and nested for CWT, the QC filter can be applied to each layer in the frequency domain separately. Based on the superposition principle, these layers constitute the filtered profile in the spatial domain. Equation (10) is the mathematical representation of a QC filter applied to the layers obtained from a CWT analysis, and the same analogy can be used for a DWT analysis, but the filters should be applied to the wavelet and scaling functions and thus define new bases:

$$f_{QC}(x = b) = \sum_{j=1}^{N} \left\langle R_0 \middle| W_f(a_j, b) \right\rangle \tag{10}$$

where f_{QC} is the rectified slope and R_0 is the QC filter in the spatial domain. The sum runs over all possible N layers of details, and, because the QC filter is linear (a linear operator), the order of filtering can be switched as shown in Equation (11).

$$f_{QC}(a,b) = \langle \psi_{a,b} | R_0 | f_s \rangle \tag{11}$$

As such the QC filter can be applied to the wavelet function, and this new filter, the QC-wavelet filter, can be used to decompose a road profile to SR layers with different frequency bands in one step. The wavelet function should be transformed to the frequency domain and filtered using the QC filter defined in Equation (9), then inverted to the spatial domain to define a QC-wavelet filter in the spatial domain. Figure 3 shows original wavelet functions and the QC-wavelet filters produced by applying the QC filter on db21 (Figure 38a and b) and the Mexican hat (Figure 38c and d) wavelet functions in the spatial domain.

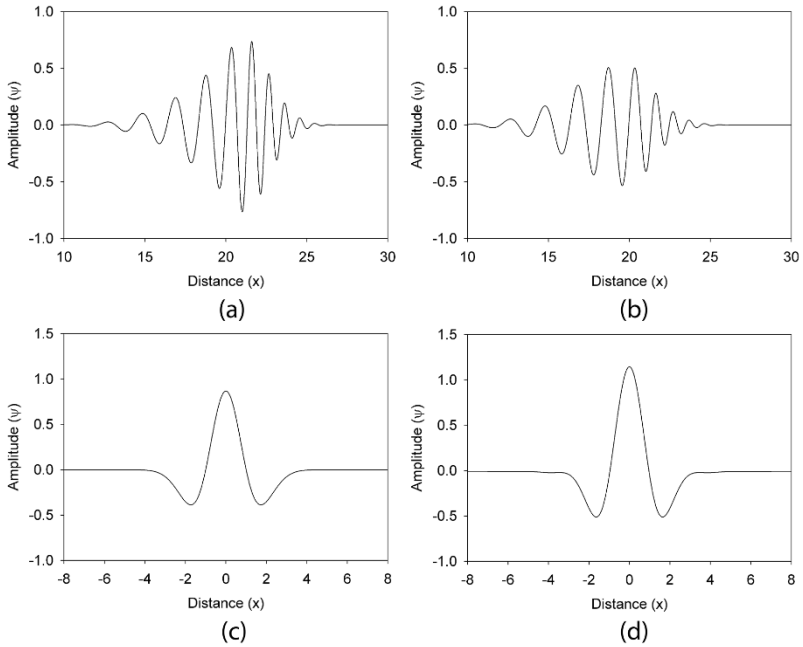

Figure 38. An (a) original Daubechies wavelet function (db21) and (b) the wavelet function after applying QC filter to it, (c) an original Mexican hat wavelet function and (d) the wavelet function after applying the QC filter to it.

In this study, three continuous and four discrete wavelet families provided in Matlab were used to analyze the 30 road profiles. A new filter bank was defined for this purpose. Table 10 provides a list of the wavelet families used in the analysis. Transforming the continuous wavelet functions to the frequency domain is straightforward because the functions have explicit forms defined in the spatial domain. However, because discrete wavelet bases are defined as functions of the points indices, profile element indices and the distance between consecutive points are used to define the spatial coordinate of a point in a wavelet basis, and accordingly define the frequency content of a wavelet basis.

Table 10. Wavelets used to design QC-wavelet filters.

Analysis scheme	Wavelet family	Wavelet Matlab name	Scaling function	Fast algorithms
Continuous Wavelet Analysis	Morlet	Analytical Morlet: morl Non-Analytical Morlet: morlex and morl0	Does not exist	Faster than traditional CWT because it utilizes FFT
	m^{th} Order Derivative of Gaussian	dog, for 2^{nd} order derivative: mexh	Does not exist	Faster than traditional CWT because it utilizes FFT
	Paul	Paul	Does not exist	Faster than traditional CWT because it utilizes FFT
Discrete Wavelet Analysis	Daubechies	db1, db2, … , db45	Exists	Available
	Symlet	sym1, sym2, … ,sym45	Exists	Available
	Coiflet	coif1, coif2, ... , coif5	Exists	Available
	Biorthogonal Wavelet Pairs	bior1.1, bior1.3, bior1.5, bior2.2, bior2.4, bior2.6, bior2.8, bior3.1, bior3.3, bior3.3, bior3.5, bior3.7, bior3.9, bior4.4, bior5.5, bior6.8	Exists	Available

To examine the accuracy of SR profiles produced by different QC-wavelet filters, all SR profiles were compared to the SR profiles produced by QC filtering in the frequency domain

and inverted to the spatial domain. Cross-correlation coefficients (C_c) were used as comparison criteria, which is a reasonable assumption since FFT analysis for long profiles will be sufficient and the boundary effects will be negligible compared to the lengths of the profiles. IRI values obtained from the FD algorithm were compared with IRI values obtained from the filters because IRI values obtained from the FD algorithm are widely used in most commercially available standard packages.

Further, to capture the effect of the analyzed profile length on the analysis, all profiles were analyzed at full length, and then shorter segments of the elevation profiles were isolated and analyzed, starting with the middle half, then the middle quarter, and then the middle one eighth and so on until reaching a length of 1.75 m. To evaluate the stability and accuracy of SR profiles produced at different lengths and using different approaches, C_c values were calculated between the SR profiles obtained from the short profile and the rectified slopes at the same points analyzed within the full length of the profile.

Results and Discussion

Long Profiles Analysis

Although 116 QC-wavelet filters were developed and tested, the results of 20 filters that effectively characterize the results are presented here. The filters were chosen to cover all families, and within the family specific wavelets were chosen based on their performance at different lengths. The Matlab bior3.1 wavelet basis is included in the summary because of its distinctly poor performance in all cases. Table 11 summarizes the sample distribution parameters; sample mean, standard deviation and range of C_c between the SR profiles produced by QC-wavelet filters and the SR profiles produced by filtering in the frequency

domain; and the absolute difference (Δ) between the IRI's obtained from the FD algorithm and the IRI obtained from the QC-wavelet filter.

Table 11. Summary of results for 20 QC-wavelet filters used to analyze the 30 profiles.

Wavelet basis	C_c summary	$\Delta = \lvert IRI_{FD} - IRI_{QCW} \rvert$ summary (m/km)	Wavelet basis	C_c summary	$\Delta = \lvert IRI_{FD} - IRI_{QCW} \rvert$ summary (m/km)
morl	$\overline{C_c} = 1.00$ $\sigma_{Cc} = 0.00$ $Range_{Cc} = 0.01$	$\overline{\Delta} = 0.06$ $\sigma\Delta = 0.05$ $Range_{\Delta} = 0.21$	sym22	$\overline{C_c} = 0.98$ $\sigma_{Cc} = 0.02$ $Range_{Cc} = 0.07$	$\overline{\Delta} = 0.12$ $\sigma\Delta = 0.11$ $Range_{\Delta} = 0.44$
morl0	$\overline{C_c} = 1.00$ $\sigma_{Cc} = 0.00$ $Range_{Cc} = 0.01$	$\overline{\Delta} = 0.20$ $\sigma\Delta = 0.13$ $Range_{\Delta} = 0.44$	sym24	$\overline{C_c} = 0.98$ $\sigma_{Cc} = 0.02$ $Range_{Cc} = 0.07$	$\overline{\Delta} = 0.12$ $\sigma\Delta = 0.11$ $Range_{\Delta} = 0.45$
mexh	$\overline{C_c} = 1.00$ $\sigma_{Cc} = 0.00$ $Range_{Cc} = 0.01$	$\overline{\Delta} = 0.05$ $\sigma\Delta = 0.08$ $Range_{\Delta} = 0.30$	coif1	$\overline{C_c} = 0.93$ $\sigma_{Cc} = 0.07$ $Range_{Cc} = 0.34$	$\overline{\Delta} = 0.07$ $\sigma\Delta = 0.10$ $Range_{\Delta} = 0.48$
paul	$\overline{C_c} = 1.00$ $\sigma_{Cc} = 0.00$ $Range_{Cc} = 0.01$	$\overline{\Delta} = 0.04$ $\sigma\Delta = 0.06$ $Range_{\Delta} = 0.23$	coif2	$\overline{C_c} = 0.96$ $\sigma_{Cc} = 0.04$ $Range_{Cc} = 0.15$	$\overline{\Delta} = 0.13$ $\sigma\Delta = 0.10$ $Range_{\Delta} = 0.53$
db18	$\overline{C_c} = 0.98$ $\sigma_{Cc} = 0.01$ $Range_{Cc} = 0.05$	$\overline{\Delta} = 0.12$ $\sigma\Delta = 0.11$ $Range_{\Delta} = 0.42$	coif3	$\overline{C_c} = 0.97$ $\sigma_{Cc} = 0.03$ $Range_{Cc} = 0.12$	$\overline{\Delta} = 0.13$ $\sigma\Delta = 0.30$ $Range_{\Delta} = 1.66$
db21	$\overline{C_c} = 0.99$ $\sigma_{Cc} = 0.01$ $Range_{Cc} = 0.05$	$\overline{\Delta} = 0.12$ $\sigma\Delta = 0.11$ $Range_{\Delta} = 0.51$	coif4	$\overline{C_c} = 0.98$ $\sigma_{Cc} = 0.02$ $Range_{Cc} = 0.09$	$\overline{\Delta} = 0.14$ $\sigma\Delta = 0.34$ $Range_{\Delta} = 1.88$
db22	$\overline{C_c} = 0.99$ $\sigma_{Cc} = 0.01$ $Range_{Cc} = 0.05$	$\overline{\Delta} = 0.12$ $\sigma\Delta = 0.12$ $Range_{\Delta} = 0.51$	bior2.4	$\overline{C_c} = 0.95$ $\sigma_{Cc} = 0.05$ $Range_{Cc} = 0.25$	$\overline{\Delta} = 0.16$ $\sigma\Delta = 0.12$ $Range_{\Delta} = 0.50$
db37	$\overline{C_c} = 0.97$ $\sigma_{Cc} = 0.01$ $Range_{Cc} = 0.05$	$\overline{\Delta} = 0.67$ $\sigma\Delta = 0.62$ $Range_{\Delta} = 1.97$	bior2.6	$\overline{C_c} = 0.96$ $\sigma_{Cc} = 0.05$ $Range_{Cc} = 0.19$	$\overline{\Delta} = 0.09$ $\sigma\Delta = 0.08$ $Range_{\Delta} = 0.32$
sym13	$\overline{C_c} = 0.98$ $\sigma_{Cc} = 0.02$ $Range_{Cc} = 0.09$	$\overline{\Delta} = 0.21$ $\sigma\Delta = 0.52$ $Range_{\Delta} = 2.94$	bior3.1	$\overline{C_c} = 0.32$ $\sigma_{Cc} = 0.19$ $Range_{Cc} = 0.72$	$\overline{\Delta} = 5.33$ $\sigma\Delta = 4.25$ $Range_{\Delta} = 15.74$
sym14	$\overline{C_c} = 0.98$ $\sigma_{Cc} = 0.02$ $Range_{Cc} = 0.08$	$\overline{\Delta} = 0.18$ $\sigma\Delta = 0.36$ $Range_{\Delta} = 2.03$	bior4.4	$\overline{C_c} = 0.96$ $\sigma_{Cc} = 0.04$ $Range_{Cc} = 0.20$	$\overline{\Delta} = 0.15$ $\sigma\Delta = 0.11$ $Range_{\Delta} = 0.53$

Results in Table 11 show that continuous wavelets outperformed all discrete wavelets in terms of C_c. This could be due to the underlying nature of the wavelets or the availability of an explicit function that allows for a more accurate Fourier transform of the wavelet and scaling functions to define the QC-wavelet filter. In this case the discrete wavelet or scaling functions sampled at a higher rate may result in a better performance for discrete wavelets.

Table 11 also shows that high C_c values do not always correspond to high correlations between the IRI obtained from the FD algorithm and the QC-wavelet filter. For example, although db18 and db37 performed similarly in terms of C_c, the range in the IRI difference for db37 is much wider, indicating that db37 results in IRI values are not comparable to the IRI values obtained from FD algorithm. Table 11 also shows that bior3.1 performed poorly compared to all 116 filters developed. The reason for the poor performance of bior3.1 is that biorthogonal pairs are defined as sets of discrete high and low pass filters with values defined at distinct points and nothing in between. As such, these filters are discontinuous unlike many other discrete wavelets where the function is continually defined however irregular. Figure 39 shows the high and low pass analysis filters for bior3.1. This function will suffer from dramatic inaccuracies if transformed into frequency domain, and this behavior cannot be mitigated using higher sampling rate of the wavelet filters.

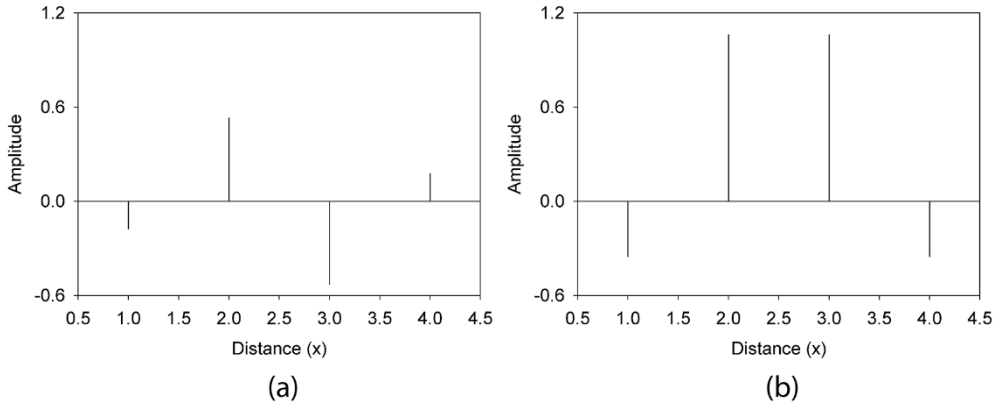

Figure 39. (a) High pass analysis filter and (b) low pass analysis filter for bior3.1 wavelet pair.

Figure 40 shows the derivative of the elevation profile for section 06B441 and the SR profile generated using the FD algorithm, the morl0 basis QC-wavelet filter, and the db21 basis QC-wavelet filter. Figure 40 also shows that the FD algorithm produced an SR profile with a phase shift, meaning that the peaks in the profile derivative (slope) will affect the SR a distance ahead, and this phase shift is not consistent. The phase shift varies depending on the nature of the profile nature, so if this technique is used for real-time autonomous monitoring it will result in spatial misallocation of the roughness. Also, even though using a morl0 basis results in a slightly higher C_c, the db21 basis will result in a closer IRI value compared to the IRI value obtained from the FD algorithm and QC filtering in the frequency domain (i.e., IRI_{FFT} = 7.70 m/km).

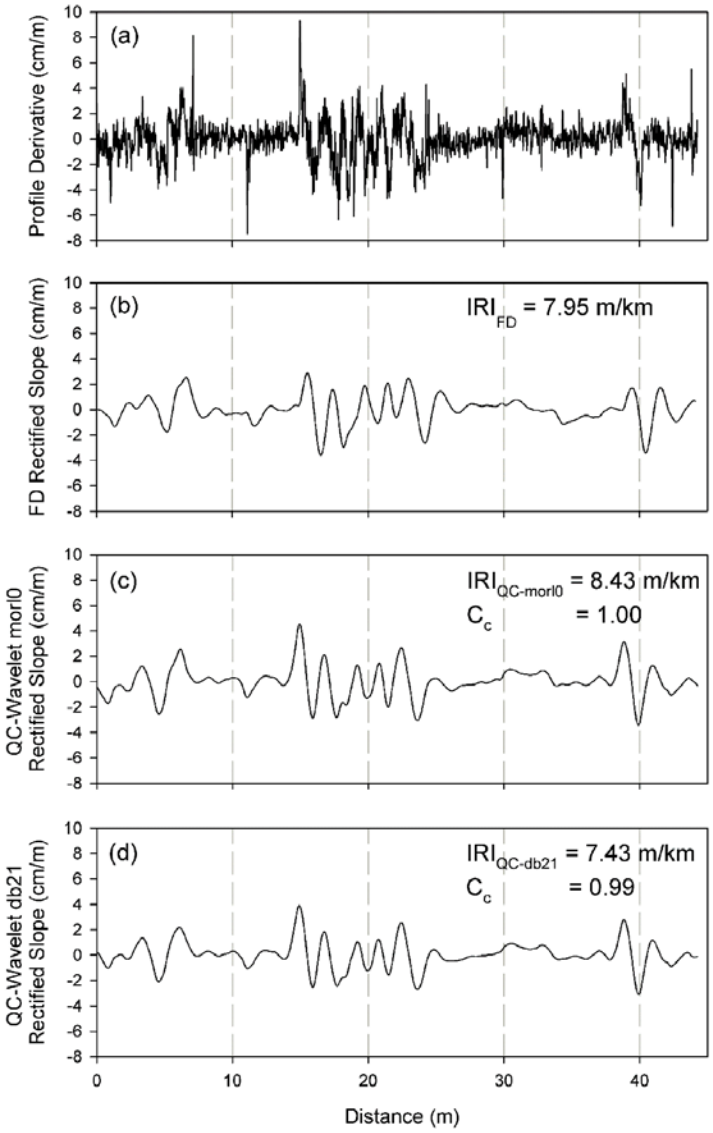

Figure 40. Comparison of (a) profile derivative, (b) rectified slope calculated using FD algorithm, (c) rectified slope calculated using QC-wavelet with morl0 basis, and (d) rectified slope calculated using QC-wavelet with db12 basis.

Stability of Analysis of Short Profiles

To capture the effect of the analyzed profile length on the analysis, the middle half of all profiles isolated and analyzed alone, then the middle quarter was isolated and analyzed, and so on until reaching the middle 1.75 m. C_c values were then calculated between the short SR

profiles and the corresponding points in the SR profile obtained for full length elevation profile. Figure 41 presents the average C_c for the 30 profiles in the study at different lengths for QC-wavelet filter with morl0 basis and one filter from each discrete family. It should be mentioned all continuous wavelets performed closely. It can be seen from the figure that morl0 basis filter out performs other filters. Also it can be seen that among discrete wavelet bases filters sym13 and db21 performed similarly and better than filters with coif3 and bior2.6 bases.

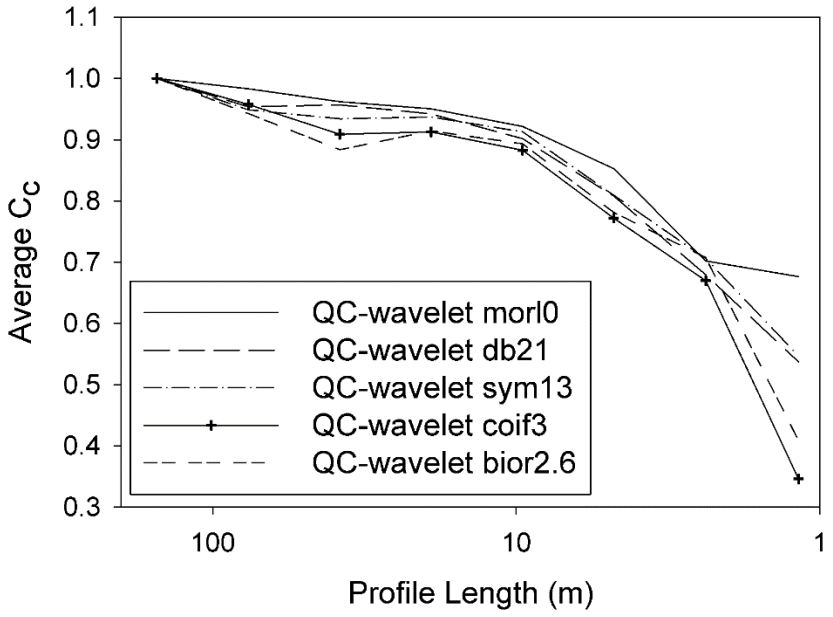

Figure 41. Average cross-correlation coefficient (C_c) versus segmented analyzed length for different QC-wavelet filters.

Figure 42 presents average C_c at different profile lengths for FD solution, QC filter applied in frequency domain, and morl0 and db21 wavelet bases QC-wavelet filters. Although the FD solution performs better than QC filter applied in frequency domain it suffers from a phase shift, while the QC-wavelet filters outperform the other approaches.

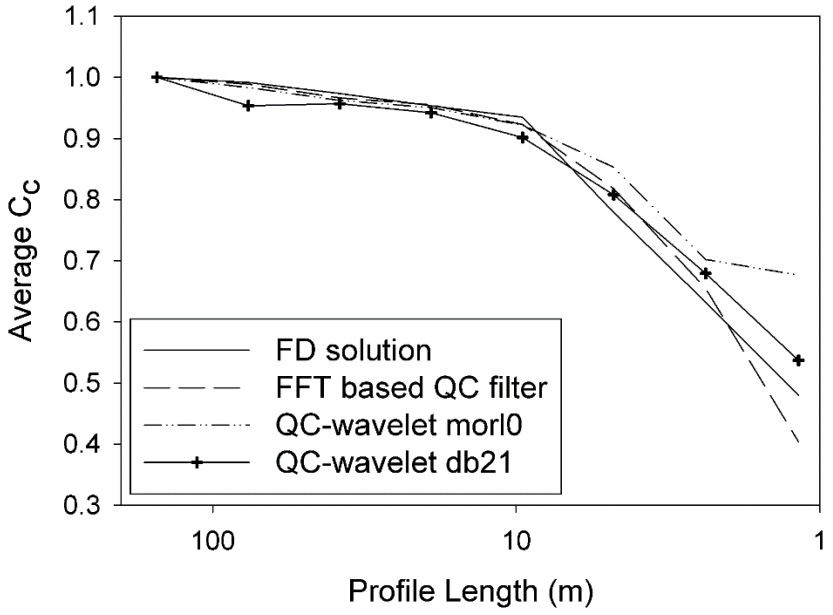

Figure 42. Average cross-correlation coefficient (C_c) versus segmented analyzed length for four approaches.

Figure 43 presents the coefficient of variation of C_c at different lengths. Coefficient of variation is defined as the sample (30 profiles) standard deviation of C_c divided over the sample mean C_c. The figure shows that db21 basis QC-wavelet filter outperforms other filters for short profiles and indicates that the solution from the db21 basis QC-wavelet filter is more consistent for different profiles. It should be mentioned that although bias and variance are two sources of error in analysis, bias indicates a consistent error in the analysis while variance describes the fluctuations in the errors.

Figure 44 presents the SR profiles for the middle 4.78 m in profile 481065. The profiles are obtained using QC filter in frequency domain, FD algorithm, QC-wavelet filter with morl0 and db21 bases. The dashed lines present the corresponding points in the full length SR profile calculated using the same algorithms. It can be seen that QC-wavelet filters are performing similar to QC filtering in the frequency domain, and different from the results

obtained from the FD algorithm. Also it can be noticed that, FD algorithm produces different results for short profiles in the first few points, however the rest of the profile matches well with the corresponding points from the full length profile. This behavior of FD algorithm is due to the fact that the algorithm autocorrelates the SR profiles for few lags, however once the distance exceeds a threshold the rest of the profile is decorrelated. In the other hand filtering algorithms analyze features with wavelengths reaching the full length of the short profile and thus produces some inaccuracies at different points in the short profile. All in all considering all profiles QC-wavelet filters are performing best.

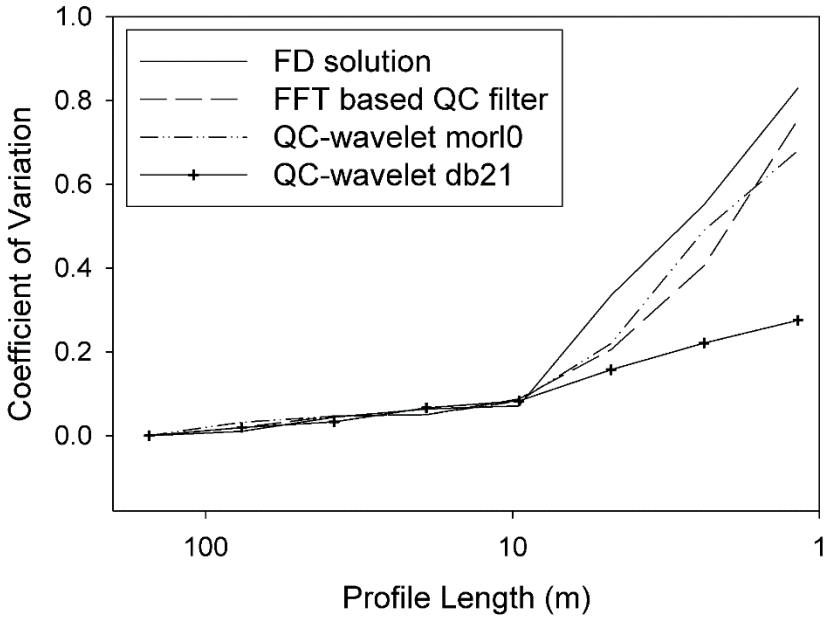

Figure 43. Coefficient of variance for the 30 profiles versus segmented analyzed length for different approaches.

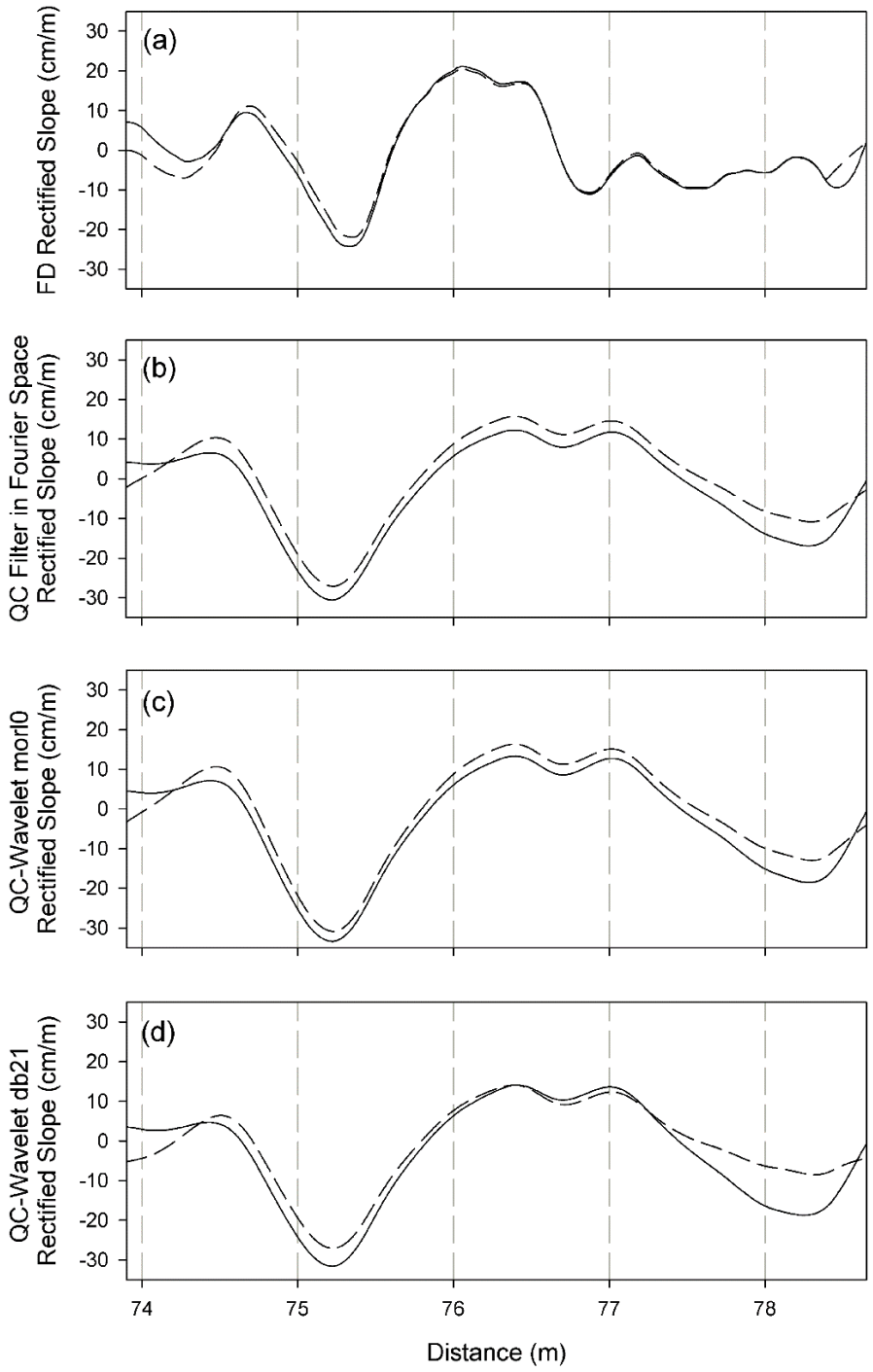

Figure 44. Rectified slopes calculated for short profiles and obtained from the full length profiles using (a) FD algorithm, (b) QC filter and FFT, (c) QC- wavelet with morl0 basis, and (d) QC- wavelet with db12 basis.

Spatial-Frequency Decomposition Using Wavelet Filters

One of the major advantages of wavelets analysis is the ability to simultaneously achieve high resolution in the spatial and frequency domains. Figure 45(a) shows the wavelet coefficients resulting from analyzing the 481065 elevation road profile using db21 wavelet. The X axis is the longitudinal distance along the profile. The Y axis indicates frequency band levels from one to seven, and the color scale on the right corresponds to the wavelet coefficients (amplitude) at analysis levels, which correspond to scale factors. Higher levels indicate features with longer wavelengths.

From any point along the X axis, the color scale along the Y axis indicates the wavelet content (i.e., analogous to frequency content in Fourier terminology) that corresponds to roughness features

Figure 45(b) represents the wavelet coefficients resulting from analyzing elevation road profiles using QC-wavelet filter with db21 basis, this is the decomposition of SR profile at different analysis levels.

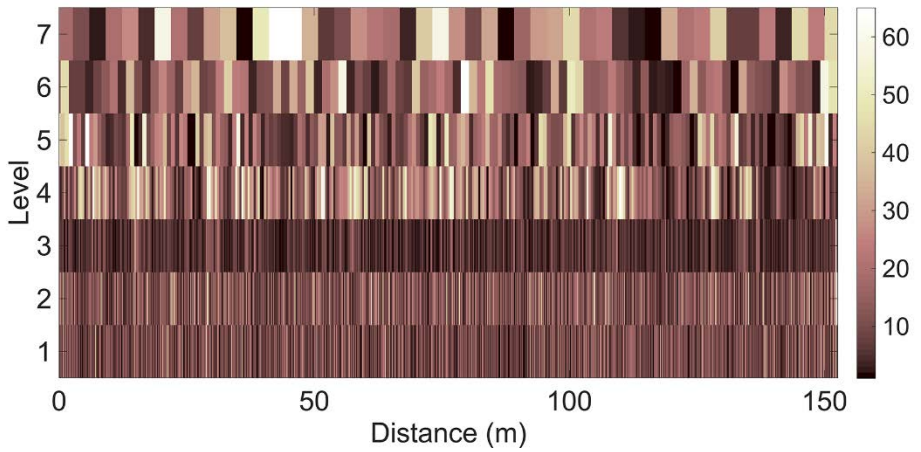

(a)

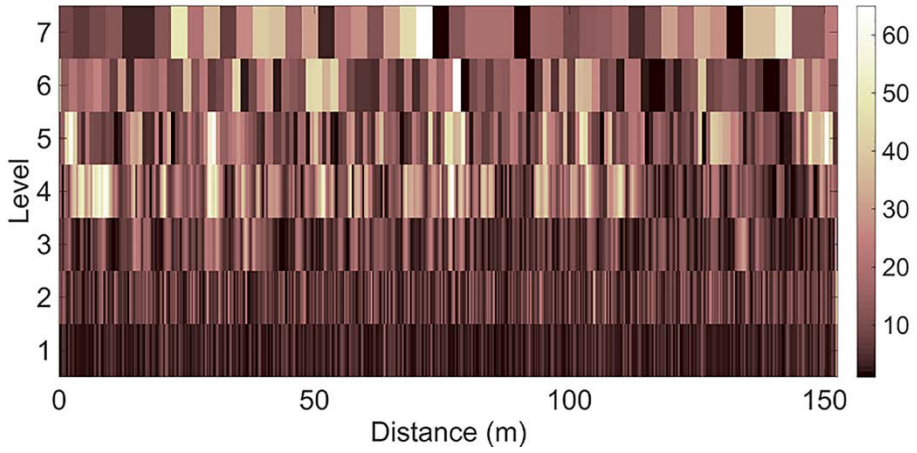

(b)

Figure 45. Wavelet decomposition amplitude contours for (a) elevation profile and (b) SR profiles using QC-wavelet filter with db21 basis.

Figure 46(a) presents the wavelet coefficients contour plot resulting from analyzing elevation road profile 481065 using morl0 wavelet. The X axis represents the distance along the road profile, moving up across the figure the color corresponds to the wavelet coefficient (amplitude) at a scale factor *a*, higher scale factors indicate features with longer wavelengths. Figure 46(b) shows the wavelet coefficients resulting from analyzing elevation road profiles using QC-wavelet filter with morl0 basis, this is the decomposition of SR profile at different scale factors. It can be noticed that these figures provide the advantage of presenting continuous scale factor range, also the scale factor can be tied directly to pseudo frequencies based on the central frequency of the wavelet, and thus it is more comprehensible and appealing than wavelet filters with discrete wavelet bases.

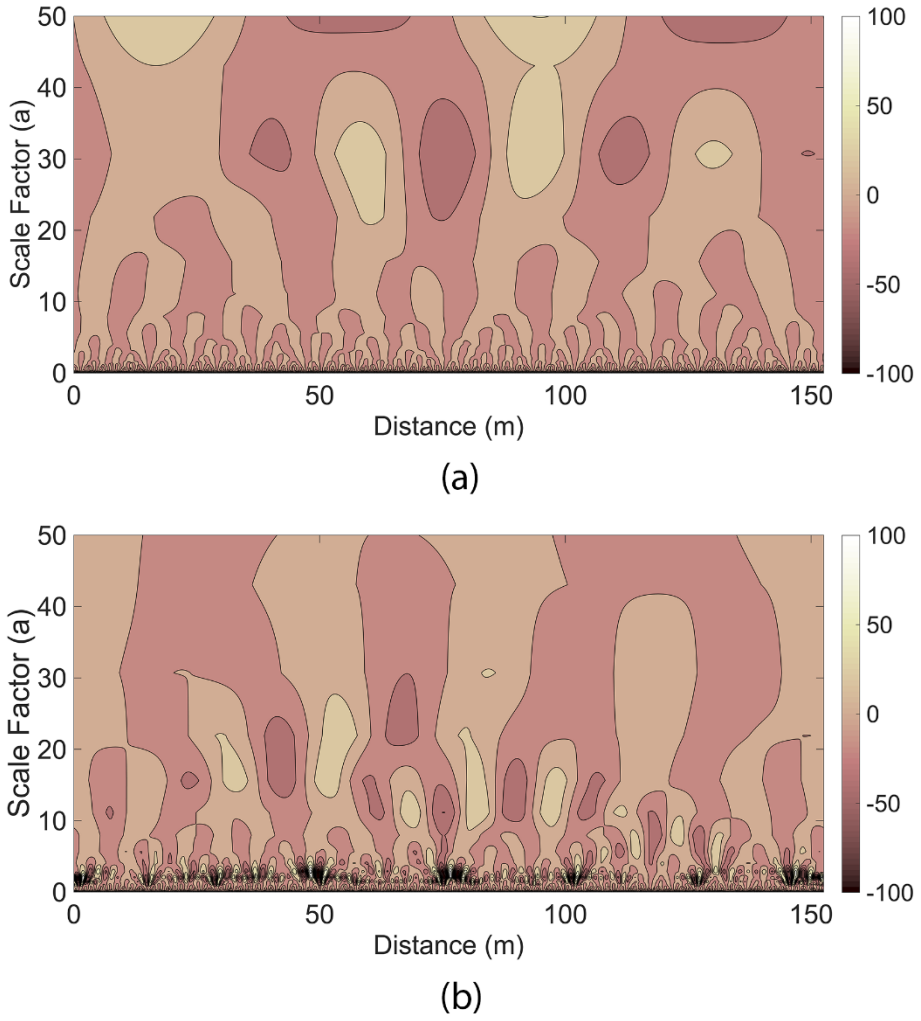

Figure 46. Wavelet decomposition amplitude contours for (a) elevation profile and (b) suspension rate profiles using QC-wavelet filter with a morl0 basis.

Conclusions

Multiple wavelet bases were modified using the QC filter in the frequency domain, including filters with explicit forms (continuous wavelets) and more complicated, iteratively constructed forms (discrete wavelets). The resulting 116 QC-wavelet filters were used to analyze 16 AC and 14 PCC road profiles with a wide range of surface roughness and the results were compared with FD algorithm and QC filtering in the frequency domain analyses.

All approaches were also tested at varying profile lengths to investigate the suitability of each approach in analyzing short segments. Of the 116 QC-wavelet filters, the filter with db21 basis outperformed other DWT bases, and the filter with morl0 basis outperformed all other QC-wavelet filters.

The key conclusions are as follows:

- Many wavelets can produce QC-wavelet filters capable of producing rectified slopes similar to those produced using QC filter in frequency domain for long enough profiles.
- Although many SR profiles have high cross-correlation coefficients with SR profiles produced by QC filtering in frequency domain, they yield different IRI values than the IRI values obtained from FD algorithm.
- FD algorithm produces a phase shift in the SR profiles, which leads to errors in identifying localized features.
- QC-wavelet filters maintain accuracy when analyzing short (i.e., $\leq$ 4.7 m) profiles.
- QC-wavelet filters with continuous wavelet bases outperform other approaches at varying lengths.
- QC-wavelet filters provide layers of detail at multiple scale factors or levels that correspond to frequency bands to locate features within specific frequency bands.

Acknowledgments

The authors wish to thank Ahmed Tamrawi for his help in developing the algorithms and Dr. Christianna White for providing review comments.

Work Cited in Chapter 5

Al-Omari, B., and Darter, M. I. (1994). "Relationships between international roughness index and present serviceability rating." *Transportation Research Record*(1435).

Alhasan, A., White, D. J., and De Brabanter, K. (2015). "Continuous wavelet analysis of pavement profiles." *Automation in Construction, Under review*.

Aslaksen, E. W., and Klauder, J. R. (1968). "Unitary representations of the affine group." *Journal of Mathematical Physics*, 9(2), 206-211.

Bianchini, A. (2012). "Fuzzy representation of pavement condition for efficient pavement management." *Computer-Aided Civil and Infrastructure Engineering*, 27(8), 608-619.

Boggess, A. (2009). *A First Course in Wavelets with Fourier Analysis*, Hoboken John Wiley & Sons, Hoboken, N.J.

Bogsjö, K., and Rychlik, I. (2009). "Vehicle fatigue damage caused by road irregularities." *Fatigue & Fracture of Engineering Materials & Structures*, 32(5), 391-402.

Calderón, A. (1964). "Intermediate spaces and interpolation, the complex method." *Studia Mathematica*, 24(2), 113-190.

Daubechies, I. (1992). *Ten lectures on wavelets*, Philadelphia, PA : Society for Industrial and Applied Mathematics, Philadelphia, PA.

Federal Highway Administration (2014). "LTPP InfoPave." Long Term Pavement Performance.

Gao, H., and Zhang, X. (2013). "A Markov-based road maintenance optimization model considering user costs." *Computer-Aided Civil and Infrastructure Engineering*, 28(6), 451-464.

Gavilán, M., Balcones, D., Marcos, O., Llorca, D. F., Sotelo, M. A., Parra, I., Ocaña, M., Aliseda, P., Yarza, P., and Amírola, A. (2011). "Adaptive road crack detection system by pavement classification." *Sensors*, 11(10), 9628-9657.

Herabat, P., and Songchitruksa, P. (2003). "A decision support system for flexible pavement treatment selection." *Computer-Aided Civil and Infrastructure Engineering*, 18(2), 147-160.

Hesami, R., and McManus, K. J. "Signal processing approach to road roughness analysis and measurement." *Proc., TENCON 2009-2009 IEEE Region 10 Conference*, IEEE, 1-6.

Liu, C., and Herman, R. (1998). "Road profiles, vehicle dynamics, and human judgment of serviceability of roads: spectral frequency domain analysis." *Journal of transportation engineering*, 124(2), 106-111.

Liu, C., and Herman, R. (1999). "Road profile, vehicle dynamics, and ride quality rating." *Journal of Transportation Engineering*, 125(2), 123-128.

Mahler, D. S., Kharoufa, Z. B., Wong, E. K., and Shaw, L. G. (1991). "Pavement distress analysis using image processing techniques." *Computer-Aided Civil and Infrastructure Engineering*, 6(1), 1-14.

Morlet, J. (1983). "Sampling theory and wave propagation." *Issues in Acoustic Signal—Image Processing and Recognition*, Springer, 233-261.

Mosa, A. M., Rahmat, R. A. O. K., Ismail, A., and Taha, M. R. (2013). "Expert System to Control Construction Problems in Flexible Pavements." *Computer-Aided Civil and Infrastructure Engineering*, 28(4), 307-323.

Nejad, F. M., and Zakeri, H. (2011). "An expert system based on wavelet transform and radon neural network for pavement distress classification." *Expert Systems with Applications*, 38(6), 7088-7101.

Nejad, F. M., and Zakeri, H. (2011). "An optimum feature extraction method based on Wavelet–Radon Transform and Dynamic Neural Network for pavement distress classification." *Expert Systems with Applications*, 38(8), 9442-9460.

Nitsche, P., Stütz, R., Kammer, M., and Maurer, P. (2014). "Comparison of machine learning methods for evaluating pavement roughness based on vehicle response." *Journal of Computing in Civil Engineering*, 28(4), 04014015.

Oijer, F., and Edlund, S. (2004). "Identification of transient road obstacle distributions and their impact on vehicle durability and driver comfort." *Vehicle System Dynamics*, 41, 744-753.

Ouyang, Y., and Madanat, S. (2004). "Optimal scheduling of rehabilitation activities for multiple pavement facilities: exact and approximate solutions." *Transportation Research Part A: Policy and Practice*, 38(5), 347-365.

Papagiannakis, A. T., Zelelew, H. M., and Muhunthan, B. (2007). "Wavelet analysis of energy content in pavement roughness and truck dynamic axle loads." *Transportation Research Record: Journal of the Transportation Research Board*, 2005(1), 153-159.

Perera, R., and Kohn, S. (2002). "Issues in pavement smoothness." *Transportation Research Board, Washington, DC*.

Pinsky, M. A. (2002). *Introduction to Fourier analysis and wavelets*, Brooks/Cole Pacific Grove.

Rasmussen, R. O., Torres, H. N., Sohaney, R. C., Karamihas, S. M., and Fick, G. (2013). "Real-time smoothness measurements on Portland cement concrete pavements during construction." Transportation Research Board, SHRP 2 Report S2-R06E-RR-1, 143p.

Roberts, C. A., and Attoh-Okine, N. O. (1998). "A comparative analysis of two artificial neural networks using pavement performance prediction." *Computer-Aided Civil and Infrastructure Engineering*, 13(5), 339-348.

Sayers, M. W. (1990). "Profiles of roughness." *Transportation Research Record*(1260), p. 106-111.

Sayers, M. W., and Karamihas, S. M. (1996). "Interpretation of road roughness profile data." University of Michigan Transportation Research Institute.

Shokouhi, P., Gucunski, N., Maher, A., and Zaghloul, S. M. (2005). "Wavelet-based multiresolution analysis of pavement profiles as a diagnostic tool." *Transportation Research Record: Journal of the Transportation Research Board*, 1940(1), 79-88.

Stein, E. M., and Shakarchi, R. (2011). *Fourier analysis: an introduction*, Princeton University Press.

Steinwolf, A., Giacomin, J., and Staszewski, W. (2002). "On the need for bump event correction in vibration test profiles representing road excitations in automobiles." *Proceedings of the Institution of Mechanical Engineers, Part D: Journal of Automobile Engineering*, 216(4), 279-295.

Swan, M., and Karamihas, S. M. (2003). "Use of a ride quality index for construction quality control and acceptance specifications." *Transportation Research Record*(1861), p. 10-16.

Tomiyama, K., Kawamura, A., and Ohiro, T. "Lifting wavelet transform for distress identification using response type profilers." *Proc., Transportation Research Board 93rd Annual Meeting*.

Ueckermann, A., and Steinauer, B. (2008). "The weighted longitudinal profile." *Road Materials and Pavement Design*, 9(2), 135-157.

Wei, L., Fwa, T., and Zhe, Z. (2005). "Wavelet analysis and interpretation of road roughness." *Journal of transportation engineering*, 131(2), 120-130.

Zalama, E., Gómez-García-Bermejo, J., Medina, R., and Llamas, J. (2014). "Road crack detection using visual features extracted by Gabor filters." *Computer-Aided Civil and Infrastructure Engineering*, 29(5), 342-358.

CHAPTER 6. GENERAL CONCLUSIONS

Road roughness is a key parameter for controlling road construction processes and for assessing ride quality during the life of paved and unpaved road systems. The quarter-car model was used as the standard mathematical tool for estimating suspension responses (SR), which can be used for summative or pointwise analysis of vehicle dynamic responses to road geometry.

In fact, transportation agencies specify roughness requirements as summative values for pavement projects that affect construction practices and contractor pay factors. The International Roughness Index (IRI), a summative statistic of quarter-car SR, is widely used to characterize overall roughness profiles of pavement stretches but does not provide sufficient detail about the frequency or spatial distribution of roughness features. This research focused on two pointwise approaches, continuous roughness maps and wavelets analysis, that both characterize overall roughness and identify localized features and compared these findings with IRI results.

Three dimensional point clouds of paved and unpaved road surfaces were acquired using a terrestrial laser scanner. The point clouds were processed in specially developed algorithms to simulate the quarter-car model using an FD algorithm to produce continuous roughness maps. It was concluded that three dimensional laser scanning techniques are powerful tools that provide detailed measurements and can be used to analyze road roughness. Also the proposed analysis technique can be used to identify localized rough features. However, varying the standard assumed speed of the quarter-car model ($V_{standard}$ = 80 km/h) indicated that not all features can be examined using SR profiles calculated in spatial domain, and for

rural roads using the standard quarter-car speed yielded unexpectedly low IRI values. This motivated the use of FFT analysis to examine the road profiles in frequency domain, and it was found that the quarter-car filter in frequency domain attenuates many rough features including the corrugations that are responsible for the low ride quality.

The limitations of the FD algorithm and FFT analysis urged the need to use different approaches that provide details in both spatial and frequency domains simultaneously. Wavelets analysis is the most well established approach to decompose signals (profiles) into layers of details with predefined frequency bands. The first intuition was to decompose road profiles and SR profiles calculated using the FD algorithm to examine the location of road contents at different frequency bands. CWT was performed on sample 30 AC or PCC road profiles with a wide range of surface roughness from the FHWA Long Term Pavement Performance data base. Further SR profiles were calculated for the layers of details using the FD algorithm, which produced the same layers of detail obtained by decomposing the SR profiles of original road profiles. This suggests that wavelet transform and quarter-car simulations (filtering) are interchangeable processes.

Despite the high resolution in both frequency and spatial domains obtained from CWT of elevation and SR profiles, the process is computationally expensive since it involves two steps of analysis, calculating SR profiles and decomposing the profile. Also the described approach in utilized FD algorithm, which suffers from phase shifts, and long distance autocorrelation of SR profiles. Since the wavelet transform and quarter-car filtering are interchangeable, QC-wavelet filters were developed by applying the quarter-car filter to CWT and DWT bases in the frequency domain, and inverted back to the spatial domain to define filters capable of filtering and decomposing road profiles in a single step. QC-wavelet

filters with bases db21 and morl0 were the best performers amongst the 116 filters developed in the study. QC-wavelet filters are expected to support data compression and allow physical inferences from compressed data.

At this stage, high resolution terrestrial laser scans are time-consuming and require trained personnel; however, this technique is encouraged for field evaluation during construction, especially when measurements cannot be obtained (i.e., fresh PCC pavements that cannot support the weight of a profiler) or for monitoring purposes where the locations of certain features are of interest. In the near term, improved terrestrial laser scanning technology with faster scanning rates and longer ranges will be able to reduce the data acquisition time significantly. Further, other laser scanning devices, such as mobile lane wide laser scanners (e.g. laser crack measurement system) and UAV laser scanners, might be a faster alternative to acquire laser scans. Future research should include alternatives to process sparse and nonuniform 3D point clouds, alternative approaches might include surface fittings or filtering data with variable spacing.

Also future studies should include improvements on QC-filters, by defining discrete wavelets with higher sampling rate. QC-wavelet filters are perfect candidates to perform analysis in real-time. The analysis can be achieved by segmenting the road sections into shorter segments, that can be processed in real-time. Also QC-wavelet filters promote the ability to compress data and make inferences on compressed data since the coefficients tie to SR profile content.

CHAPTER 7. WORKS CITED

Abbas, A., Kutay, M. E., Azari, H., and Rasmussen, R. (2007). "Three-Dimensional Surface Texture Characterization of Portland Cement Concrete Pavements." *Computer-Aided Civil and Infrastructure Engineering*, 22(3), 197-209.

Ahlin, K., and Granlund, N. J. (2002). "Relating road roughness and vehicle speeds to human whole body vibration and exposure limits." *International Journal of Pavement Engineering*, 3(4), 207-216.

Al-Omari, B., and Darter, M. I. (1994). "Relationships between international roughness index and present serviceability rating." *Transportation Research Record*(1435).

Alhasan, A., White, D. J., and De Brabanter, K. (2015). "Continuous wavelet analysis of pavement profiles." *Automation in Construction, Under review*.

Anderegg, R., and Kaufmann, K. (2004). "Intelligent compaction with vibratory rollers: Feedback control systems in automatic compaction and compaction control." *Transportation Research Record: Journal of the Transportation Research Board*, 1868(1), 124-134.

Archondo-Callao, R. (1999). "Unpaved roads roughness estimation by subjective evaluation." *The World Bank*.

Archondo-Callao, R. (2007). "Evaluating economically justified road works expenditures on unpaved roads in developing countries." *Transportation Research Record: Journal of the Transportation Research Board*(1989), 41-49.

Aslaksen, E. W., and Klauder, J. R. (1968). "Unitary representations of the affine group." *Journal of Mathematical Physics*, 9(2), 206-211.

ASTM E1926-08 (2015). "Standard Practice for Computing International Roughness Index of Roads from Longitudinal Profile Measurements." ASTM International, West Conshohocken, PA, 2015, www.astm.org.

Attoh-Okine, N. O. (2001). "Grouping Pavement Condition Variables for Performance Modeling Using Self-Organizing Maps." *Computer-Aided Civil and Infrastructure Engineering*, 16(2), 112-125.

Bandara, N., and Gunaratne, M. (2001). "Current and future pavement maintenance prioritization based on rapid visual condition evaluation." *Journal of Transportation Engineering*, 127(2), 116-123.

Barrett, L. "Automated machine guidance: An emerging technology whose time has come?" *Proc., Transportation Research Board Annual Meeting. Washington, DC. January*.

Baus, R. L., and Wang, W. (2004). "Development of profiler-based rideability specifications for asphalt pavements and asphalt overlays." FHWA.

Berthelot, C. F., Podborochynski, D., Stuber, E., Prang, C., and Marjerison, B. "Saskatchewan case studies of network and project level applications of a structural asset management system." *Proc., Seventh International Conference on Managing Pavement Assets*.

Bianchini, A. (2012). "Fuzzy representation of pavement condition for efficient pavement management." *Computer-Aided Civil and Infrastructure Engineering*, 27(8), 608-619.

Blateyron, F. (2013). "The Areal Field Parameters." *Characterisation of Areal Surface Texture*, R. K. Leach, ed., Springer, 15-43.

Boggess, A. (2009). *A First Course in Wavelets with Fourier Analysis*, Hoboken John Wiley & Sons, Hoboken, N.J.

Bogsjö, K., and Rychlik, I. (2009). "Vehicle fatigue damage caused by road irregularities." *Fatigue & Fracture of Engineering Materials & Structures*, 32(5), 391-402.

Bosché, F., and Biotteau, B. (2015). "Terrestrial laser scanning and continuous wavelet transform for controlling surface flatness in construction – A first investigation." *Advanced Engineering Informatics*.

Bosché, F., and Guenet, E. (2014). "Automating surface flatness control using terrestrial laser scanning and building information models." *Automation in Construction*, 44, 212-226.

Brokaw, M. (1967). "Development of the PCA road meter: a rapid method for measuring slope variance." *Highway Research Record*(189).

Brooks, C., Colling, T., Kueber, M. J., Roussi, C., and Endsley, A. (2011). "Characterization of unpaved road condition through the use of remote sensing." Michigan Tech Research Institute.

Broughton, S. A., and Bryan, K. M. (2011). *Discrete Fourier analysis and wavelets: applications to signal and image processing*, John Wiley & Sons.

Brown, M., Mercier, S., and Provencher, Y. (2003). "Road maintenance with Opti-Grade®: Maintaining road networks to achieve the best value." *Transportation Research Record: Journal of the Transportation Research Board*, 1819(1), 282-286.

Buchanan, J. A., Catudal, A. L., Greenshields, B. D., and Moyer, R. A. (1941). "Standardizable equipment for evaluating road surface roughness." *Highway Research Board Proceedings*, 20.

Bureau of Transportation Statistics (2015). "Table 1-4: Public Road and Street Mileage in the United States by Type of Surface (Thousands of miles)." <http://www.rita.dot.gov/bts/sites/rita.dot.gov.bts/files/publications/national_transportation_statistics/html/table_01_04.html>. (February 20, 2015).

Byrne, M., Albrecht, D., Sanjayan, J., and Kodikara, J. (2009). "Recognizing patterns in seasonal variation of pavement roughness using minimum message length inference." *Computer-Aided Civil and Infrastructure Engineering*, 24(2), 120-129.

Calderón, A. (1964). "Intermediate spaces and interpolation, the complex method." *Studia Mathematica*, 24(2), 113-190.

Capuruço, R. A., Hegazy, T., Tighe, S. L., and Zaghloul, S. (2005). "Full-car roughness index as summary roughness statistic." *Transportation Research Record: Journal of the Transportation Research Board*, 1905(1), 148-156.

Chang, J.-R., Chang, K.-T., and Chen, D.-H. (2006). "Application of 3D laser scanning on measuring pavement roughness." *ASTM Journal of Testing and Evaluation*, 34(2), 83-91.

Chang, J.-R., Su, Y.-S., Huang, T.-C., Kang, S.-C., and Hsieh, S.-H. "Measurement of the international roughness index (IRI) using an autonomous robot (P3-AT)." *Proc., 26th International Symposium on Automation and Robotics in Construction (ISARC). International Association for Automation and Robotics in Construction*.

Chau, K., Anson, M., and Zhang, J. (2004). "Four-dimensional visualization of construction scheduling and site utilization." *Journal of construction engineering and management*, 130(4), 598-606.

Cheng, H.-D., and Miyojim, M. (1998). "Automatic pavement distress detection system." *Information Sciences*, 108(1), 219-240.

Cheng, H., Chen, J., Glazier, C., and Hu, Y. (1999). "Novel approach to pavement cracking detection based on fuzzy set theory." *Journal of Computing in Civil Engineering*, 13(4), 270-280.

Chootinan, P., Chen, A., Horrocks, M. R., and Bolling, D. (2006). "A multi-year pavement maintenance program using a stochastic simulation-based genetic algorithm approach." *Transportation Research Part A: Policy and Practice*, 40(9), 725-743.

Choubane, B., McNamara, R. L., and Page, G. C. (2002). "Evaluation of high-speed profilers for measurement of asphalt pavement smoothness in Florida." *Transportation Research Record: Journal of the Transportation Research Board*, 1813(1), 62-67.

Daubechies, I. (1992). *Ten lectures on wavelets*, Philadelphia, PA : Society for Industrial and Applied Mathematics, Philadelphia, PA.

Dewan, S., and Smith, R. (2002). "Estimating International Roughness Index from Pavement Distresses to Calculate Vehicle Operating Costs for the San Francisco Bay Area." *Transportation Research Record*, 1816(1), 65-72.

E950M-09, A. E. "Standard Test Method for Measuring the Longitudinal Profile of Traveled Surfaces with an Accelerometer Established Inertial Profiling Reference."ASTM International, West Conshohocken, PA, 2008, www.astm.org.

Eaton, R. A., and Beaucham, R. E. (1992). "Unsurfaced road maintenance management." U.S. Army Cold Regions Research and Engineering Laboratory, 67 p.

Eaton, R. A., Gerard, S., and Dattilo, R. S. "A method for rating unsurfaced road." *Proc., Fourth International Conference*, p. 34-43.

El-Korchi, T., Bacon, J., Turo, M., and Ecmecian, M. (2002). "Ride quality assessment with pavement profiling devices." *Transportation Research Record: Journal of the Transportation Research Board*, 1806(-1), 140-148.

El-Korchi, T., and Collura, J. (1998). "Comparative study of ride quality measuring devices." *Transportation Research Record: Journal of the Transportation Research Board*, 1643(-1), 125-135.

Federal Highway Administration (2014). "LTPP InfoPave." Long Term Pavement Performance.

Fernando, E., Walker, R., and Mikhail, M. (2014). "Comparative testing of lasers for ride quality measurement on hot-mix asphalt pavements." *Transportation Research Record: Journal of the Transportation Research Board*, 2457, 19-29.

Fernando, E. G., and Walker, R. S. (2013). "Impact of changes in profile measurement technology on QA testing of pavement smoothness: Technical Report."Alexandria, VA: National Technical Information Service., 188p.

Fernando, E. G., Walker, R. S., and Mikhail, M. "Comparative Testing of Lasers for Ride Quality Measurement on HMA Pavements." *Proc., Transportation Research Board 93rd Annual Meeting*.

Flintsch, G., de León, E., McGhee, K., and Al-Qadi, I. (2003). "Pavement Surface Macrotexture Measurement and Applications." *Transportation Research Record: Journal of the Transportation Research Board*, 1860(1), 168-177.

Fu, P., Lea, J. D., Lee, J. N., and Harvey, J. T. (2013). "Comprehensive evaluation of automated pavement condition survey service providers' technical competence." *International Journal of Pavement Engineering*, 14(1), 36-49.

Gao, H., and Zhang, X. (2013). "A Markov-based road maintenance optimization model considering user costs." *Computer-Aided Civil and Infrastructure Engineering*, 28(6), 451-464.

Gavilán, M., Balcones, D., Marcos, O., Llorca, D. F., Sotelo, M. A., Parra, I., Ocaña, M., Aliseda, P., Yarza, P., and Amírola, A. (2011). "Adaptive road crack detection system by pavement classification." *Sensors*, 11(10), 9628-9657.

Georgopoulos, A., Loizos, A., and Flouda, A. (1995). "Digital image processing as a tool for pavement distress evaluation." *ISPRS Journal of Photogrammetry and Remote Sensing*, 50(1), 23-33.

Gillespie, T., Sayers, M., and Segel, L. (1980). "Calibration of response-type road roughness measuring systems." Washington, DC: Transportation Research Board, National Research Council, NCHRP Report 228, Available from: http://www.trb.org/Publications/Pages/262.aspx.

Gillespie, T. D. (1992). *Fundamentals of vehicle dynamics*, Warrendale, PA : Society of Automotive Engineers, Warrendale, PA.

Gillespie, T. D., Sayers, M. W., and Hagan, M. R. (1987). "Methodology for road roughness profiling and rut depth measurement." Federal Highway Administration, 47P.

Goodspeed, C. H., Schmeckpeper, E. R., and Lemieux, R. L. "Road surface management system." Transportation Research Board, p. 242-248.

Hannon, J. J. (2007). *Emerging technologies for construction delivery*, Transportation Research Board, Washington D.C.

Herabat, P., and Songchitruksa, P. (2003). "A decision support system for flexible pavement treatment selection." *Computer-Aided Civil and Infrastructure Engineering*, 18(2), 147-160.

Hesami, R., and McManus, K. J. "Signal processing approach to road roughness analysis and measurement." *Proc., TENCON 2009-2009 IEEE Region 10 Conference*, IEEE, 1-6.

Huntington, G., and Ksaibati, K. (2011). "Implementation guide for the management of unsealed gravel roads." *Transportation Research Record: Journal of the Transportation Research Board*, 2205(1), 189-197.

Janoff, M. S. (1988). "Pavement roughness and rideability field evaluation." Washington, DC: Transportation Research Board, National Research Council, NCHRP Report 308.

Jolliffe, I. (2005). *Principal component analysis*, Wiley Online Library. doi:10.1002/0470013192.bsa501.

Karamihas, S. M., Gillespie, T. D., Perera, R. W., and Kohn, S. D. (1999). "Guidelines for longitudinal pavement profile measurement: final report." Transportation Research Board, 81 p.

Kilpeläinen, P., Jaakkola, M., and Alanaatu, P. (2011). "Development of a control system for a multipurpose road repairing machine." *Automation in Construction*, 20(6), 662-668.

Kohn, S. D., Perera, R. W., Cable, J. K., Karamihas, S. M., and Swanlund, M. "Use of profile data to detect concrete paving problems." *Proc., 9th International Conference on Concrete Pavements*, pp 690-703.

Kuo, C. M., Fu, C. R., and Chen, K. Y. (2011). "Effects of Pavement Roughness on Rigid Pavement Stress." *Journal of Mechanics*, 27(1), 1-8.

Lamptey, G., Labi, S., and Li, Z. (2008). "Decision support for optimal scheduling of highway pavement preventive maintenance within resurfacing cycle." *Decision Support Systems*, 46(1), 376-387.

Laurent, J., Savard, Y., and Lefebvre, D. (2014). "3D laser road profiling for the automated survey of road surface conditions and geometry." *The 17th IRF World Meeting & Exhibition*, Proceedings of the Institute of Radio Engineers, 30. Riyadh, Saudi Arabia, November.

Lin, J.-D., Yau, J.-T., and Hsiao, L.-H. "Correlation analysis between international roughness index (IRI) and pavement distress by neural network." *Proc., 82nd annual meeting in January, 2003*.

Liu, C., and Herman, R. (1998). "Road profiles, vehicle dynamics, and human judgment of serviceability of roads: spectral frequency domain analysis." *Journal of transportation engineering*, 124(2), 106-111.

Liu, C., and Herman, R. (1999). "Road profile, vehicle dynamics, and ride quality rating." *Journal of Transportation Engineering*, 125(2), 123-128.

Loizos, A., and Plati, C. (2008). "An alternative approach to pavement roughness evaluation." *International Journal of Pavement Engineering*, 9(1), 69-78.

Mahgoub, H., Bennett, C., and Selim, A. (2011). "Analysis of Factors Causing Corrugation of Gravel Roads." *Transportation Research Record: Journal of the Transportation Research Board*, 2204(-1), 3-10.

Mahler, D. S., Kharoufa, Z. B., Wong, E. K., and Shaw, L. G. (1991). "Pavement distress analysis using image processing techniques." *Computer-Aided Civil and Infrastructure Engineering*, 6(1), 1-14.

Marcondes, J., Burgess, G. J., Harichandran, R., and Snyder, M. B. (1991). "Spectral analysis of highway pavement roughness." *Journal of transportation engineering*, 117(5), 540-549.

MathWorks. 2013. MATLAB and Wavelet Toolbox 2013bThe MathWorks, Inc., Natick, Massachusetts, United States.

McDonald, T., and Sperry, R. (2013). "Evaluation of mitigation for safety concerns on low-volume, unpaved rural roads." Institute for Transportation, Iowa State University, Ames, IA.

Morlet, J. (1983). "Sampling theory and wave propagation." *Issues in Acoustic Signal—Image Processing and Recognition*, Springer, 233-261.

Mosa, A. M., Rahmat, R. A. O. K., Ismail, A., and Taha, M. R. (2013). "Expert System to Control Construction Problems in Flexible Pavements." *Computer-Aided Civil and Infrastructure Engineering*, 28(4), 307-323.

Moyer, R., and Ahlborn, G. (1956). "New developments in the BPR roughness indicator and tests on California pavements." *HRB Bulletin*, 139.

Mucka, P., and Granlund, J. (2012). "Comparison of longitudinal unevenness of old and repaired highway lanes." *Journal of Transportation Engineering*, 138(3), pp 371-380.

Murray, R. M., Li, Z., Sastry, S. S., and Sastry, S. S. (1994). *A mathematical introduction to robotic manipulation*, CRC press.

Nakamura, V. F., and Michael, H. L. (1962). "Serviceability ratings of highway pavements : technical paper." FHWA/IN/JHRP-62/18. Joint Highway Research Project, Indiana Department of Transportation and Purdue University, West Lafayette, Indiana, 1962., 43p.

Namur, E., and de Solminihac, H. (2009). "Roughness of unpaved roads." *Transportation Research Record: Journal of the Transportation Research Board*, 2101, 10-16.

Navon, R., and Shpatnitsky, Y. (2005). "Field experiments in automated monitoring of road construction." *Journal of construction engineering and management*, 131(4), 487-493.

Nejad, F. M., and Zakeri, H. (2011). "An expert system based on wavelet transform and radon neural network for pavement distress classification." *Expert Systems with Applications*, 38(6), 7088-7101.

Nejad, F. M., and Zakeri, H. (2011). "An optimum feature extraction method based on Wavelet–Radon Transform and Dynamic Neural Network for pavement distress classification." *Expert Systems with Applications*, 38(8), 9442-9460.

Nick, J., and Janoff, M. (1983). "Evaluation of panel rating methods for assessing pavement ride quality." *Transportation Research Record: Journal of the Transportation Research Board*(946).

Nitsche, P., Stütz, R., Kammer, M., and Maurer, P. (2014). "Comparison of machine learning methods for evaluating pavement roughness based on vehicle response." *Journal of Computing in Civil Engineering*, 28(4), 04014015.

Oijer, F., and Edlund, S. (2004). "Identification of transient road obstacle distributions and their impact on vehicle durability and driver comfort." *Vehicle System Dynamics*, 41, 744-753.

Ouyang, W., and Xu, B. (2013). "Pavement cracking measurements using 3d laser-scan images." *Measurement Science and Technology*, 24(10), 105204.

Ouyang, Y., and Madanat, S. (2004). "Optimal scheduling of rehabilitation activities for multiple pavement facilities: exact and approximate solutions." *Transportation Research Part A: Policy and Practice*, 38(5), 347-365.

Papagiannakis, A. T., Zelelew, H. M., and Muhunthan, B. (2007). "Wavelet analysis of energy content in pavement roughness and truck dynamic axle loads." *Transportation Research Record: Journal of the Transportation Research Board*, 2005(1), 153-159.

Papagiannakis, A. T., Zelelew, H. M., and Muhunthan, B. (2007). "A wavelet interpretation of vehicle-pavement interaction." *International Journal of Pavement Engineering*, 8(3), 245-252.

Park, K., Thomas, N. E., and Wayne Lee, K. (2007). "Applicability of the international roughness index as a predictor of asphalt pavement condition." *Journal of Transportation Engineering*, 133(12), 706-709.

Perera, R., and Kohn, S. (2002). "Issues in pavement smoothness." *Transportation Research Board, Washington, DC*.

Pinsky, M. A. (2002). *Introduction to Fourier analysis and wavelets*, Brooks/Cole Pacific Grove.

Radopoulou, S. C., and Brilakis, I. (2015). "Patch detection for pavement assessment." *Automation in Construction*, 53(0), 95-104.

Rahim, A. M., Fiegel, G., Ghuzlan, K., and Khumann, D. (2009). "Evaluation of international roughness index for asphalt overlays placed over cracked and seated concrete pavements." *International Journal of Pavement Engineering*, 10(3), 201-207.

Rasmussen, R. O., Torres, H. N., Sohaney, R. C., Karamihas, S. M., and Fick, G. (2013). "Real-time smoothness measurements on Portland cement concrete pavements during construction." Transportation Research Board, SHRP 2 Report S2-R06E-RR-1, 143p.

Research, and analytics (2012). "Miles of public roads in Iowa by surface type." <http://www.iowadot.gov/research/analytics/publicroads.html>. (February 20, 2015).

Roberts, C. A., and Attoh-Okine, N. O. (1998). "A comparative analysis of two artificial neural networks using pavement performance prediction." *Computer-Aided Civil and Infrastructure Engineering*, 13(5), 339-348.

Sayers, M. W. (1989). "Two quarter-car models for defining road roughness: IRI and HRI." *Transportation Research Record*(1215), 165-172.

Sayers, M. W. (1990). "Profiles of roughness." *Transportation Research Record*(1260), p. 106-111.

Sayers, M. W., Gillespie, T. D., and Paterson, W. D. (1986). "Guidelines for conducting and calibrating road roughness measurements." *Technical Report UMTRI-84-13, Washington, DC: The World Bank.*

Sayers, M. W., Gillespie, T. D., and Queiroz, A. (1986). "The international road roughness experiment. Establishing correlation and a calibration standard for measurements." *Technical Report HS-039 586, Washington, DC: The World Bank.*

Sayers, M. W., and Karamihas, S. M. (1996). "Interpretation of road roughness profile data." University of Michigan Transportation Research Institute.

Sayers, M. W., and Karamihas, S. M. (1998). "The little book of profiling." *Ann Arbor: Transportation Research Institute, University of Michigan*.

Sen, R., Hassan, R. A., and Evans, R. P. (2012). "Wavelet-based detection of roughness progression in wavebands for highways in Victoria, Australia." *Transportation Research Record: Journal of the Transportation Research Board*, 2304(1), 17-27.

Shi, X., and Cai, C. (2009). "Simulation of dynamic effects of vehicles on pavement using a 3D interaction model." *Journal of Transportation Engineering*, 135(10), 736-744.

Shokouhi, P., Gucunski, N., Maher, A., and Zaghloul, S. M. (2005). "Wavelet-based multiresolution analysis of pavement profiles as a diagnostic tool." *Transportation Research Record: Journal of the Transportation Research Board*, 1940(1), 79-88.

Soria, M., and Fontenele, E. (2003). "Field evaluation of method for rating unsurfaced road conditions." *Transportation Research Record: Journal of the Transportation Research Board*, 1819(-1), 267-272.

Spangler, E., and Kelly, W. (1964). "GMR road profilometer—A method for measuring road profile." *General Motors Corporation*.

Stein, E. M., and Shakarchi, R. (2011). *Fourier analysis: an introduction*, Princeton University Press.

Steinwolf, A., Giacomin, J., and Staszewski, W. (2002). "On the need for bump event correction in vibration test profiles representing road excitations in automobiles." *Proceedings of the Institution of Mechanical Engineers, Part D: Journal of Automobile Engineering*, 216(4), 279-295.

Suermann, P. C. (2009). "Evaluating the impact of building information modeling (BIM) on construction." Doctoral dissertation: University of Florida.

Sun, L. (2003). "Simulation of pavement roughness and IRI based on power spectral density." *Mathematics and computers in simulation*, 61(2), 77-88.

Sun, L., and Deng, X. (1998). "Predicting vertical dynamic loads caused by vehicle-pavement interaction." *Journal of transportation engineering*, 124(5), 470-478.

Sun, L., Hudson, W., and Zhang, Z. (2003). "Empirical-mechanistic method based stochastic modeling of fatigue damage to predict flexible pavement cracking for transportation infrastructure management." *Journal of Transportation Engineering*, 129(2), 109-117.

Swan, M., and Karamihas, S. M. (2003). "Use of a ride quality index for construction quality control and acceptance specifications." *Transportation Research Record*(1861), p. 10-16.

Tomiyama, K., Kawamura, A., and Ohiro, T. "Lifting wavelet transform for distress identification using response type profilers." *Proc., Transportation Research Board 93rd Annual Meeting*.

Transportation, U. S. D. o. (2012). "Highway Statistics 2012." Federal Highway Administration, Washington, DC.

Tsai, Y., Jiang, C., and Huang, Y. (2012). "Multiscale crack fundamental element model for real-world pavement crack classification." *Journal of Computing in Civil Engineering*, 28(4), 04014012.

Tsai, Y. J., Wu, J., Wang, Z., and Hu, Z. (2010). "Horizontal roadway curvature computation algorithm using vision technology." *Computer-Aided Civil and Infrastructure Engineering*, 25(2), 78-88.

Tsunokawa, K., and Schofer, J. L. (1994). "Trend curve optimal control model for highway pavement maintenance: Case study and evaluation." *Transportation Research Part A: Policy and Practice*, 28(2), 151-166.

Ueckermann, A., and Steinauer, B. (2008). "The weighted longitudinal profile." *Road Materials and Pavement Design*, 9(2), 135-157.

Vidya, R., Santhakumar, S. M., and Mathew, S. (2013). "Estimation of IRI from PCI in construction work zones." *ACEE International Journal on Civil and Environmental Engineering*, 2(1).

Walker, D., Entine, L., and Kummer, S. (2002). "Gravel-Paser Manual: pavement surface evaluation and rating." Wisconsin Transportation Information Center.

Walker, R. S., and Hudson, W. R. (1973). "A correlation study of the Mays road meter with the surface dynamics profilometer." Center for Highway Research, University of Texas at Austin.

Wand, M. (1997). "Data-based choice of histogram bin width." *The American Statistician*, 51(1), 59-64.

Wei, L., Fwa, T., and Zhe, Z. (2005). "Wavelet analysis and interpretation of road roughness." *Journal of transportation engineering*, 131(2), 120-130.

White, D. J., Vennapusa, P., and Thompson, M. J. (2007). "Field validation of intelligent compaction monitoring technology for unbound materials." *Tech Transfer Summaries*(Paper 2).

White, D. J., and Vennapusa, P. K. R. "Report of the workshop on intelligent construction for earthworks." *Proc., Workshop on Intelligent Construction for Earthworks*, 156p.

Woll, J. H., Surdahl, R. W., Everett, R., and Andresen, R. (2008). "Road stabilizer product performance: Seedskadee national wildlife refuge." *FHWA-CFL/TD-08-005*.

Zalama, E., Gómez-García-Bermejo, J., Llamas, J., and Medina, R. (2011). "An effective texture mapping approach for 3D models obtained from laser scanner data to building documentation." *Computer-Aided Civil and Infrastructure Engineering*, 26(5), 381-392.

Zalama, E., Gómez-García-Bermejo, J., Medina, R., and Llamas, J. (2014). "Road crack detection using visual features extracted by Gabor filters." *Computer-Aided Civil and Infrastructure Engineering*, 29(5), 342-358.

Zhang, C. (2009). "Monitoring the condition of unpaved roads with remote sensing and other technology." Geographic Information Science Center of Excellence, South Dakota State University.

Zhang, C., and Elaksher, A. (2012). "An unmanned aerial vehicle-based imaging system for 3D measurement of unpaved road surface distresses." *Computer-Aided Civil and Infrastructure Engineering*, 27(2), 118-129.

Zhang, C., and Elaksher, A. (2012). "An Unmanned Aerial Vehicle-Based Imaging System for 3D Measurement of Unpaved Road Surface Distresses1." *Computer-Aided Civil and Infrastructure Engineering*, 27(2), 118-129.

Zimmerman, K., and Wolters, A. (2004). "Local road surfacing criteria." South Dakota Department of Transportation, Federal Highway Administration, Applied Pavement Technology, Inc.

APPENDIX PSEUDOCODES FOR ANALYSIS ALGORITHMS

Algorithm 1. Pseudocode for continuous roughness maps

Input: $P = [x, y, z]$ // spatial coordinates of N points in a point cloud
$P = P - \bar{P}$ // shift the origin to point clod center
$Var\left(P_{x-y}\right) = Var(x) + Var(y)$ // *x-y* plane variance is the sum of variances in *x* and *y*
$\theta = \arg\max_{\theta \in [0,\pi]} (x \cos\theta + y \sin\theta)^2$ // maximize the variance in the *x* direction
$P = R_\theta P$ // rotate data using R_θ to define *x* as longitudinal direction
quadratic surface fit ← *S* // construct inertial reference
P = P – S
$n = (x_{max} - x_{min})/\delta_x$, $m = (y_{max} - y_{min})/\delta_y$ // define a grid of size $n \times m$ and spacing δ_x and δ_y
    for $i \leftarrow 1$ **to** (n) **do**
        for $j \leftarrow 1$ **to** (m) **do**
            for $k \leftarrow 1$ **to** (N)
                If $(i - 1) \times \delta_x < x_k < i \times \delta_x$ & $(j - 1) \times \delta_y < y_k < j \times \delta_y$ **then**
                    c = c + 1
                    sum = sum + z_k
                    $z_{i,j} = z_k / c$, $x_{i,j} = (i - 0.5)\,\delta_x$, $y_{i,j} = (j - 0.5)\,\delta_y$
                end if
            end for
        end for
    end for
Return $G = [x_i, y_j, z_{i,j}]$ // define an elevation mesh grid
    for $j \leftarrow 1$ **to** (m) **do**
        $[IRI_j , RS_{i,j}] \leftarrow$ QCFD $(v, z_{i,j})$, **where** $i \in [1, n]$ // input the *m* profiles in a mesh along the *x* direction in the quarter-car finite difference simulation algorithm to get rectified slope at each point for different speeds *v*.
    end for
Return Roughness map = $[x_i, y_j, RS_{i,j}]$
Return IRI_j

Algorithm 2. Pseudocode for continuous QC-wavelet filtering

Input: (*P*, *wave)*, where *P* = [*x*, *z*] // spatial coordinates of *N* points in a profile P and wavelet name

$\omega_i = 2i\pi/N\delta x$ where, $i \in [1, N/2]$

$\omega = [0;\ \omega_i;\ -\omega_j]$ where, $i \in [1, N/2], j \in [N/2\ , 1]$ // define spatial frequency (wave number) vector

    for $k \leftarrow 1$ **to** ($n_{a,max}$) // run over defined scales

        $\hat{\psi}_a \leftarrow fft\ (\psi_a)$ // find the fast Fourier transform of wavelet function at a scale a

        $QC\psi_a \leftarrow ifft\ (R_0\hat{\psi}_a)$ // define the QC-wavelet filter as the Fourier inverse of wavelet basis multiplied by QC filter.

        Return $SR_a \leftarrow P^* QC\psi_a$ // convolve the profile with the QC-wavelet filter to produce a suspension response layer of detail

    end for

Return $SR_{QC\psi} = \sum_{n_a} SR_a$ // define the suspension response profile as the sum of all detail layers

$SR_{fft} \leftarrow ifft\ (R_0\hat{P})$ // calculate the suspension response using Fourier transform

Return $C_c \leftarrow (SR_{QC\psi}SR_{fft})/(\sigma_{SR,QC\psi}\sigma_{SR,fft})$ // calculate the cross correlation coefficient at lag 0